Dynamical Evolution and High-Energy Radiation of Mixed-Morphology Supernova Remnants

Takafumi Shimizu

Thesis submitted to
Tokyo Metropolitan University

Doctor of Philosophy
in Physics

Department of Physics
1-1 Minami-Osawa, Hachioji-shi, Tokyo, Japan 192-0397

February 20, 2014

Abstract

Evolution of a supernova remnant (SNR) without an active neutron star is basically described by probation of shock waves. The shock waves accelerate charged particles. The particles accelerated to GeV radiate synchrotron radio emission, which appears to be shell-like morphology. The shock waves heat matter up to keV, and heated-electrons ionize ions. Compared with a time-scale of shock-heating of electrons by the shock, a time-scale of ionization of ions by electron collisions in the shock down stream region is longer. Hence an ionization state of SNR plasma is thought to be under-ionized state in which the ionization temperature is lower than the electron temperature, or collisional ionization equilibrium state at late time. In fact, X-ray spectra of many SNRs are explained by such plasma state model. SNRs that exhibit shell-like morphology in thermal X-ray as well as radio are categorized into shell-like SNRs.

In contrast to shell-like SNRs, some SNRs exhibit shell-like radio but center-filled thermal X-ray morphology. Such SNRs are categorized into mixed-morphology SNRs (MM SNRs). Many MM SNRs interact with molecular clouds, suggested by OH maser and near infrared observations, and hence are thought to be remnants of core-collapse supernova of massive stars. Interestingly, recombination radiation X-rays, which are evidence that X-ray emitting plasmas are over-ionized states in which the ionization temperature is higher than the electron temperature, are detected from six MM SNRs. The center-filled X-rays with recombination radiation can not be explained by a picture of shock-wave propagation that explains the X-rays of shell-like SNRs.

As well as X-rays, MM SNRs are characteristic in γ-ray emission. Several MM SNRs and shell-like SNRs are detected in the GeV γ-ray band by *Fermi*. The $1-100$ GeV γ-ray luminosities of MM SNRs are $\sim 10^{34}-10^{36}$ erg s^{-1}, which are systematically higher than those of shell-like SNRs of $\sim 10^{33}-10^{35}$ erg s^{-1}. Such high luminosities may be caused by π^0-decay γ-rays enhanced by the interactions with molecular clouds. The γ-ray spectra of SNRs are fitted to broken power-laws with break energies of $1-100$ GeV above which the spectra become steep.

If the progenitors of MM SNRs are massive stars, their X-ray characters may caused by progenitors and/or their environment. One possibility of the origin of over-ionized state is rarefaction: when the blast wave breaks out of the dense circumstellar matter, consists of stellar wind matter blown out by the progenitor, into rarefied interstellar medium, electrons rapidly cool by adiabatic expansion, leaving a high ionization state (Itoh and Masai 1989). Such SNR evolution is investigated only by Itoh and Masai (1989), and whether the evolution results in other characters of MM SNRs is not clear.

The work of Itoh and Masai (1989) is spherically-symmetric calculation. We extent their work to three dimensional non-symmetric calculation. In realistic stellar wind, more matter is in the equatorial plane by rotation, like observed around B[e] stars. Assuming such distribution of stellar wind matter, we carry out numerical hydrodynamic calculation of adiabatic gas. As a result of the calculation, we find that shocked ejecta and stellar wind matter become over-ionized states due to rarefaction after the break-out when the anisotropies of stellar wind matter are considered. The shocked ejecta contribute X-ray emission dominantly, because the density of the shocked ejecta is higher that those of the shocked stellar

wind matter and ISM. The X-ray emission measure appears to be an irregular shape depending on viewing angle in early times after the break-out because of the anisotropies of stellar wind matter., e.g., bar-like structure with wings at either end in equatorial view. Since the shocked ejecta are located far inside the blast wave, the distribution of emission measure is inside the blast wave. Using the results of hydrodynamic calculations, we investigate synchrotron radio and bremsstrahlung, inverse-Compton scattering, and π^0-decay γ-ray emissions from blast-shocked ISM shell. Just after the break-out, the blast wave is accelerated to have a high velocity, which is favor for magnetic field amplification near the shock. We take such amplification into calculation. As a result, the radio flux at 1 GHz is tens of Jy, which is comparable to typical observed value of MM SNRs. From the above results of radio and X-rays, we find that the SNR after the break-out exhibit radio shell and center-filled recombination radiation X-ray morphology, as observed in MM SNRs. The γ-ray luminosity is dominated by inverse-Compton scattering because of low density. The total γ-ray luminosity, including bremsstrahlung and π^0-decay, is on the order of 10^{33} erg s^{-1}, which is lower than the typical value of MM SNRs of $10^{34} - 10^{36}$ erg s^{-1}. However, if e.g., 10% of accelerated protons interact with some matter of density of ~ 100 cm^{-3}, the π^0-decay γ-ray luminosity would be enhanced to be comparable with the typical value.

In order to verify the SNR model considered in the present thesis, we investigate observations of X-ray fluxes and γ-ray spectra, referring to radio, of MM SNRs comparing with shell-like SNRs. The 2.1-10 keV X-rays to 1 GHz radio flux ratios of MM SNRs are lower than those of shell-like SNRs at the same 1 GHz surface brightness. This can be explain by lower emissivity of plasma in the over-ionized state than other ionization states.

Contents

Chapter 1

Introduction

Massive stars with mass more than $\sim 8M_{\odot}$ or white dwarfs with companion stars explode at the end of their evolutions, observed as supernovae (SNe). In case of a massive star, a neutron star or black hole is formed after the explosion in the center at the explosion. After the explosion, ejected matter, called ejecta, interact circumstellar matter (CSM) or interstellar medium (ISM) to form a blast wave and reverse shock that propagate outward and inward, respectively, from a contact discontinuity between these matter. If the neutron star neither is active nor present, evolution of a remnant of the SN is basically described by propagation of the shock waves. The shock waves accelerate charged particles. The particles accelerated up to ∼GeV energy radiate synchrotron radio emission. The shock waves heat the matter. The matter heated up to 10^7 K radiate thermal X-rays. The remnant that exhibits shell-like morphology in both radio and X-ray band is called shell-like supernova remnant (SNR). Figure 1.1 (a) shows radio and X-ray surface brightness of a shell-like SNR Tycho. Compared with a time-scale of shock-heating of electrons, a time-scale of ionization of ions by electron collisions in the shock down stream region is longer. Hence an ionization state of X-ray emitting plasma is thought to be under-ionized state in which the ionization temperature is lower than the electron temperature, $T_{\rm z} < T_{\rm e}$, or ionization equilibrium state, $T_{\rm z} = T_{\rm e}$. In fact, this picture explains X-ray spectra of many shell-like SNRs.

If an active neutron star presents, it affects evolution of a SNR. The neutron star accelerated charged particles to radiate non-thermal radio and X-rays. When such radiation is dominated in a SNR, the SNR exhibits center-filled radio and X-ray morphology and is called plerion. Besides, there are SNRs that exhibit both center-filled non-thermal radio/X-ray and shell-like non-thermal radio/thermal X-ray morphologies. The SNRs of this type are called composite. Figures 1.1 (c) and (d) show a plerion 3C58 and composite G11.2-0.3, respectively.

In addition to three types of SNRs, there is another type of SNRs that exhibit shell-like radio and center-filled thermal X-ray morphology without active neutron star. Such SNRs are called mixed-morphology SNRs (e.g., Rho and Petre 1998 [153]), hereafter we call MM SNRs. A formation mechanism of the center-filled X-rays are not clear. Figures 1.1 (b) shows radio and X-ray surface brightness of a MM SNR MSH 11-61A. On the contrary to the shock-heating and ionizing picture mentioned above, Kawasaki et al. (2002) [104] found that

plasma of MM SNR IC 443 is an over-ionized state in which $T_z > T_e$ by *ASCA* observation. Kawasaki et al. (2005) [105] further investigated five other MM SNRs (W49B, W28, W44, 3C391, and Kes 27), and found that W49B shows an over-ionized plasma state. The over-ionized states of these two MM SNRs are proved by radiative recombination continua in X-ray spectra detected by *Suzaku* (Yamaguchi et al. 2009 [202] for W49B; Ozawa et al. 2009 [136] for IC443). Radiative recombination X-rays are detected also from other MM SNRs, G359.1-0.5 (Ohnishi et al. 2011 [134]), W44 (Uchida et al. 2012 [184]), W28 (Sawada and Koyama 2012 [163]), and G346.6-0.2 (Yamauchi et al. 2013a [204]), and SNR CTB 37A[1] (Yamauchi et al. 2013b [205]). Although samples are still limited, the over-ionized plasmas are found from SNRs interacting with molecular clouds, suggested by observations of 1720 MHz hydroxyl (OH) maser (Frail et al. 1994 [64]; Yusef-Zadeh et al. 1995 [207]; Frail et al. 1996 [65]; Claussen et al. 1997 [49]; Koralesky et al. 1998 [110]) and near infrared (Keohane et al. 2007 [106]). The presence of the molecular clouds suggests that progenitors are massive stars. Hence, the over-ionized plasma are possibly related to massive stars and/or their environment.

MM SNRs are also characterized by γ-rays as compared to shell-like SNRs. *Fermi* detects GeV γ-rays from several MM SNRs (Castro and Slane 2010 [43]; Abdo et al. 2010a [2]; Abdo et al. 2010b [3]; Ajello et al. 2012 [16], Ackermann et al. 2013 [9]; Pivato et al. 2013 [143]). Many of γ-ray spectra of MM SNRs are fitted to broken power-laws with broken energies of $\sim 1 - 100$ GeV above with the spectra become steep. The $1 - 100$ GeV γ-ray luminosity of MM SNRs are in the range of $10^{34} - 10^{36}$ erg s^{-1}, which are typically higher than those of shell-like SNRs of $10^{33} - 10^{35}$ erg s^{-1} (Castro and Slane 2010 [43]; Abdo et al. 2011 [4]; Tanaka et al. 2011 [178]; Katagiri et al. 2011 [99]; Giordano et al. 2012 [76]; Katsuta et al. 2012 [103]; Hewitt et al. 2012 [87]; Yuan et al. 2013 [206]). Such high luminosities may be due to enhancement of π^0-decay γ-rays by interactions with dense molecular clouds and/or H I gas. In fact, spectral signature of π^0-decay are detected in γ-ray spectra of two MM SNRs IC443 and W44 (Giuliani et al. 2011 [77]; Ackermann et al. 2013 [9]). The spectral signature may be detected also in Cas A (Yuan et al. 2013 [206]), which has relatively high γ-ray luminosity of 4×10^{34} erg s^{-1} in shell-like SNRs.

Several models of MM SNRs are proposed; cloud evaporation by White and long (1991) [194], radiative phase by Cox et al. (1999) [50], projection by Hnatyk and Petruk (1999) [90] and Petruk (2001) [141]. Another possibility is rarefaction in the adiabatic evolution phase of the SNR, which can be explain the over-ionized state; when the blast wave breaks out of the dense CSM, like stellar wind of a massive progenitor, into ISM, the shock-heated electrons would rapidly cool due to adiabatic expansion, leaving highly ionized state (Itoh and Masai 1989 [95]). However, it is not clear that this picture can explain other characters of MM SNR, especially center-filled X-ray morphology.

In the present thesis, we investigate dynamical evolution and high energy radiation of SNR expanding into dense CMS and ISM outside, as a model of MM SNR. We extend

[1]CTB 37A is proposed as a MM SNR because of center-filled thermal X-ray morphology (Sezer et al. 2011 [168]) and detection of radiative recombination X-rays (Yamauchi et al. 2013 [205]). However, we do not include this remnant in MM and shell-like SNRs because the remnant has a candidate of pulsar wind nebula in the radio shell.

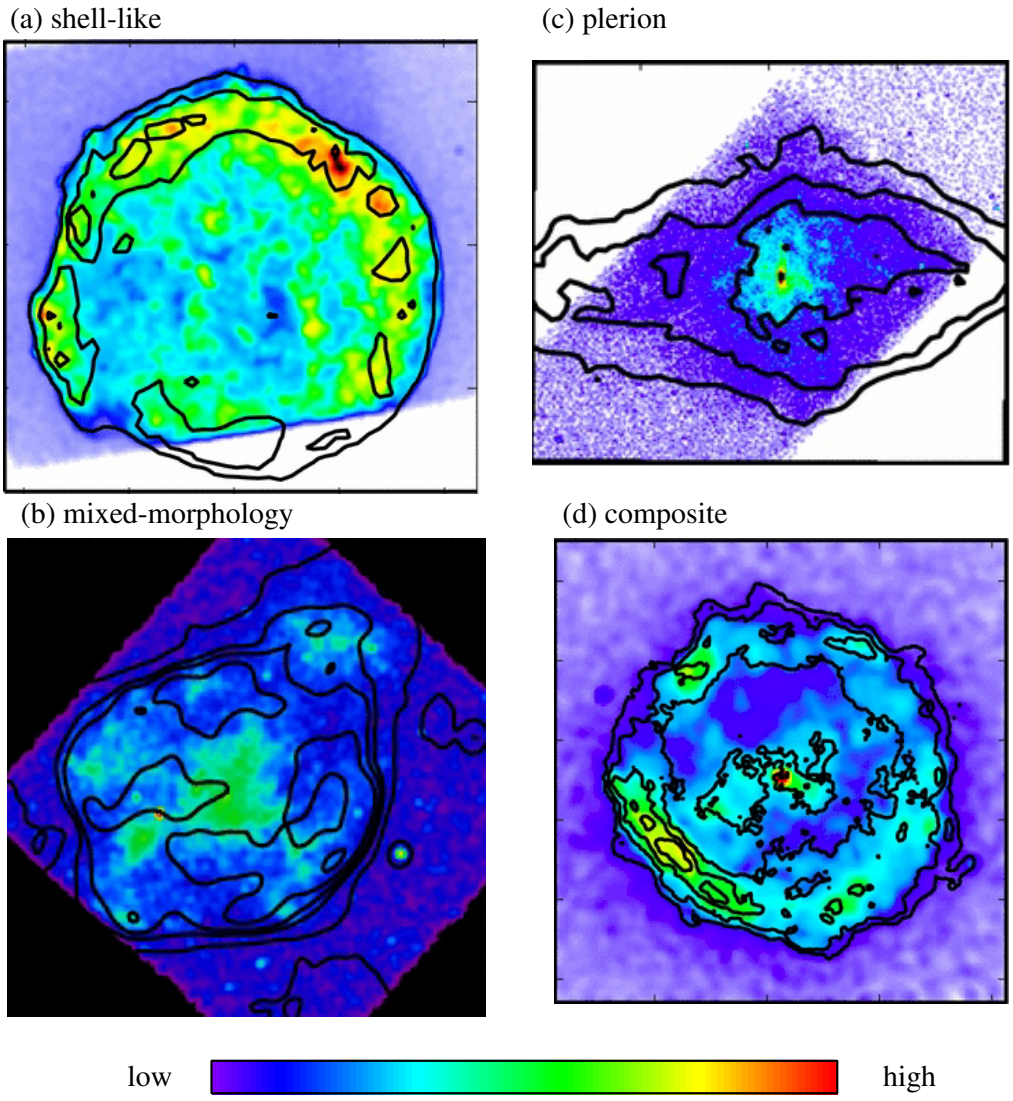

Figure 1.1: Radio (black contour) and X-ray (color image) surface brightnesses of (a) shell-like SNR Tycho, (b) mixed-morphology SNR MSH 11-61A, (c) plerion 3C58 , and (d) composite G11.2-0.3. These figures are taken from Chandra supernova remnant catalog (available at http://chandra.harvard.edu/photo/category/snr.html).

the spherical symmetric calculation of the work of Itoh and Masai (1989) [95] to three dimensional hydrodynamical calculation, considering realistic distribution of CSM. Unlike their work, we do not take ionization or radiation processes into account; we assume the relevant SNR evolution is fully adiabatic. In chapter 2, we describe an overview of SN and standard scenario of evolution of SNR. In chapter 3, we compare the standard model with shell-like SNRs and MM SNRs. In chapter 4, we describe the model of MM SNRs and present calculations and results. In chapter 5, we discusses the results and the implications. In chapter 6, we give a summary.

Chapter 2

Supernova and Supernova Remnant

At an explosion of supernova (SN), part or all of a progenitor are ejected with an initial speed of $V_{\rm ej} \sim 10^4 (E_{\rm ej}/10^{51}\ {\rm erg})^{1/2} (M_{\rm ej}/M_\odot)^{1/2}$ km s^{-1}, where $E_{\rm ej}$ and $M_{\rm ej}$ are the explosion energy and the mass of ejected matter, respectively. Such ejected matter are called ejecta. The ejecta interact with ambient medium to propagate a blast wave and reverse shock propagate outward and inward, respectively from a contact discontinuity of these matter. Although the ambient medium is mainly though to be interstellar medium (ISM), it may be a dense circumstellar matter (CSM) composed of stellar wind matter blown out in pre-supernova phase when the progenitor is a massive star. In fact, radio and X-ray emissions from shocked CSM are detected in some supernovae (SNe). As the blast wave expands, the SN transforms into the SNR. SNRs are categorized by radio and X-ray surface brightnesses, as described in chapter 1. These brightnesses reflect dynamical evolution of SNRs. The radio and X-ray spectra reflect non-thermal and thermal evolution of SNRs, respectively. The evolutions of SNRs without active neutron stars are basically described by the shock waves. In the following, we describe observational properties of SNe in section 2.1. The dynamical, thermal and non-thermal evolutions are described in section 2.2, 2.3, and 2.4, respectively

2.1 Supernovae

Supernovae are energetic events caused by explosions of stars at the end of their lives, observed commonly in the optical wavelength with sudden brightening followed by decaying. According to the optical spectra near maximum light and the light curves, SNe are classified into subclasses (e.g., Filippenko 1997 [63]). Supernovae that show no hydrogen absorption line are called type I, while those that show such line are called type II (Minkowski 1941 [126]). The type I SNe are divided into three subclasses called Ia, Ib and Ic, by early-time spectra. The type Ia SNe show singly ionized silicon (Si II) absorption line, while type Ib/c does not show the line (e.g., Bertola 1964 [30]). The type Ib SNe are distinguished from type Ic by the presence of neutral helium (He I) absorption line. The type II SNe are divided into four subclasses called IIP, IIL, IIn, and IIb. The type IIP SNe show a plateau in the light curve after the magnitude becomes a peak value, while the type IIL SNe show linear decrease

with time from the peak (e.g., Barbon et al. 1979 [24]). The type IIn SNe shows relatively narrow emission line, especially of hydrogen (e.g., Schhegel 1990 [165]). The type IIb SNe is a class intermediate between type II and Ib; the hydrogen absorption line is initially present in their spectra, but the line disappears and then He I absorption line appears (e.g., Filippenko 1988 [62]). Such transition suggests a connection between type II and Ib SNe. As mentioned above, SNe show observational variety. This variety are thought to reflect progenitor type and/or environment of the progenitor.

The progenitors of SNe are thought to be two types. One is the thermonuclear explosion of white dwarf (e.g., Hillebrandt and Niemeyer [89]), and the other is core-collapse of massive star ($\gtrsim 8M_\odot$) (e.g, Woosley et al. 2002 [196]). Each type of explosion releases kinetic energies of $\sim 10^{51}$ erg.

White dwarf is a degenerate star that a low mass star ($\lesssim 3M_\odot$) becomes after a nuclear fusion is over. The nuclear fusion in the low mass star progress up to the stage of helium burning, which produce carbon and oxygen. After the helium burning is over, the star cools and shrink to a size of $\sim 10^4$ km at which the self-gravity balances with the degenerate pressure of electrons. Such compact object is called white dwarf. When the white dwarf have a companion star, the mass of white dwarf increases with time by mass transfer from the star. When the mass of white dwarf becomes Chandrasekhar mass of $1.4M_\odot$, which is the limit mass that can be supported by the degenerate pressure, the white dwarf explodes by thermonuclear reaction. This type of explosion of SN is though to be observed as type Ia, because white dwarf have no hydrogen envelope while silicon is produce at the explosion.

On contrast to the low mass star, the nuclear fusion of massive star ($\lesssim 8M_\odot$) progresses to the stage of silicon burning, which produce iron. Because iron is most stable element, nuclear burning of iron do not occur and iron core is formed in the center of the star. As iron is produced by silicon burning, the iron core becomes dense and hot by shrink due to self-gravity. When the iron core density and temperature become $\sim 10^{10}$ K and $\sim 10^9$ g cm^{-3}, respectively, iron is decomposed into helium and neutron by photodissociation. After that, the iron core collapses to form denser core, and the envelope also collapses to fall into the center. Part of envelope are bounced by the core and ejected into outside the star, leaving neutron star or black hole in the central region. This is called core-collapse SN explosion. The core-collapse SNe are thought to be observed as type Ib/c or II. The spectroscopic difference among these type SNe are thought to reflect hydrogen and helium envelope of progenitors. The progenitors of type II SNe have hydrogen envelope despite blowing stellar wind, while those of type Ib/c SNe are stripped of hydrogen envelope by the stellar wind or mass exchange with the companion. The spectral transition of type IIb is caused by thin hydrogen envelope outside helium envelope. The progenitor of type Ic SNe are stripped of helium in addition to hydrogen envelope. The candidate for the stripped progenitor is Wolf-Rayet stars (e.g., Woosley et al. 1995 [197]). On the other hand, the progenitors for type II SNe are red supergiants, blue supergiants, and luminous blue variables. We show a classification scheme of SNe in figure 2.1.

The stellar wind blown out by massive stars before the explosion forms CSM. After the explosion occur, ejected matter, called ejecta, interact with the CSM first. Such interaction is suggested by radio (e.g., Weiler et al. 2002 [192]) and X-ray (e.g., Schlegel 1995 [166])

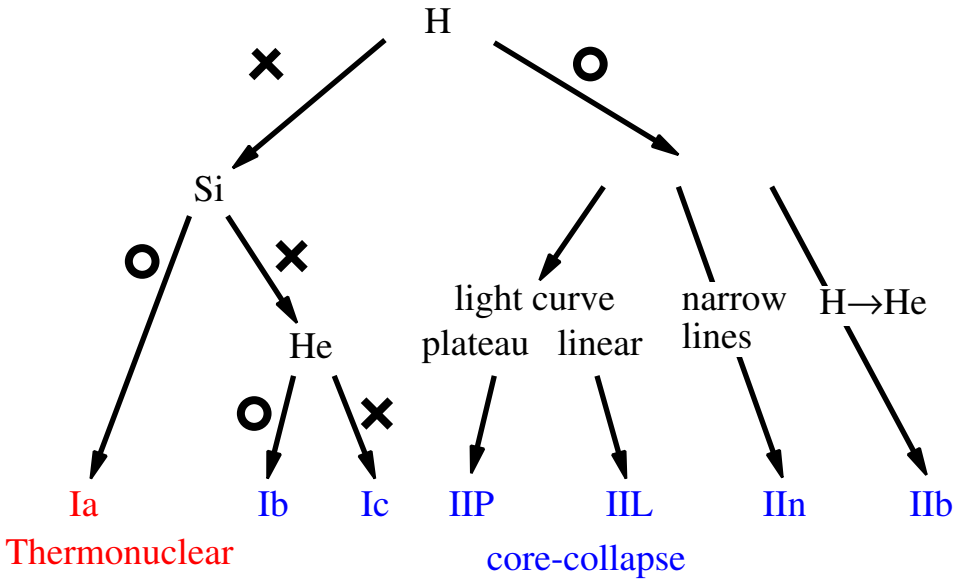

Figure 2.1: Classification of SNe by optical observations. The characters "H", "Si", and "He" mean absorption lines of hydrogen, silicon, and helium, respectively. The symbols "○" and "×" represent that these lines are and are not observed, respectively. Type II SNe are divided into four types. The SNe that show narrow emission lines, especially of hydrogen, are called type IIn. The other SNe that show plateau phase or linear decline in the early-time light curves are called type IIP or IIL, respectively. Type Ia SNe are thought to be originated from thermonuclear explosion of white dwarfs, while type Ib/c and II SNe are thought to be originated from core-collapse of massive stars.

emissions, which are observed only in core-collapse SNe so far (e.g., for radio, Panagia et al. 2006 [137]; for X-ray, Russell and Immler 2012 [157]). In addition, the narrow emission lines of type IIn are caused by the interaction. Those are emitted from pre-shocked CSM ionized by radiation of shocked CSM and ejecta. Mass loss rates of progenitor of type IIn SNe calculated from results of multi-wavelength observations are about $10^{-4} - 1 M_{\odot}$ yr^{-1} (Kiewe et al. 2012 [107]). Such high rates are possible for luminous blue variable. In fact, progenitors of two type IIn SNe 2005gl and 2009ip are luminous blue variables (Gal-Yam and Leonard 2009 [70]; Mauerhan et al. 2013 [119]). Because of dense mass-loss, several type IIn SNe are members of most luminous SNe powered by the interaction of ejecta with the CSM (Gal-Yam 2012 [69]). High luminosities powered by the interaction are observed also from type IIL SNe. The lack of narrow emission lines of the luminous IIL SNe despite the interactions may be due to location of shock break-out (Chevalier and Irwin 2011 [48]) or non-steady wind (Moriya and Tominaga 2012 [130]).

2.2 Dynamical Evolution of Supernova Remnant

An initial phase of SNR evolution, a blast wave is driven by a ram pressure of ejecta. This phase is called free expansion phase (e.g., Chevalier 1982 [47]). A blast-shocked matter receives the energy from the ejecta, and becomes dominant in the energy of SNR on a time-

scale that the blast-shocked mass is comparable to the ejecta mass. Then, the blast wave is driven by thermal pressure of the shocked matter. Such phase is called Sedov-Taylor phase (Taylor 1950 [180]; Sedov 1959 [167]). The free expansion and Sedov-Taylor phases also called adiabatic phase because radiative loss negligible for dynamical evolution in these phases. As the blast wave expands, a temperature and hence radiative cooling time of-scale of shocked matter decrease. After the cooling time-scale becomes smaller than dynamical time-scale, the cooling affects the dynamical evolution. Such phase is called radiative phase.

We consider the dynamical evolution in two manners; one is a thin shell approximation, and the other is self-similar analysis. In the former, the evolution is modeled by expansion of a shell of shocked matter. Solving equation of motion of the shell assumed to be infinitesimal thin, we get a relation of a radius of the blast wave to time but does not give a structure in the shell. The latter is based on Euler equations that are transformed into dimensionless form by use of self-similar variable given by dimensional analysis. The dimensional analysis give the relation of a radius of the blast wave to time, and the solution of these equations give the structure in the shell. The structures at different epochs are the same under a scale transformation, i.e., self-similar. The self-similar analysis is applied to describing the dynamical evolution of SNR in free expansion phase by Chevalier (1982) [47] and in Sedov-Taylor phase by Taylor (1950) [180] and Sedov (1959) [167].

In the following sections, we first describe a relation between physical quantities in shock down and up stream region. Then the dynamical evolution in the three phases are described.

2.2.1 Shock Jump Condition

A shock wave is a transition layer propagating into medium. The shock compresses the medium and transfers the kinetic energy of the incoming medium to degree of freedom of the downstream medium. In space plasma, shocks are likely to be collisionless, i.e., thickness of shock transition layer is thinner than a length of mean free path of Coulomb collisions. In-situ observations of Earth's bow shock prove that the shock is collisonless (Sonett and Abrams 1963 [171]; Ness et al. 1964 [133]). Although such observation for shocks of SNRs can not be carried out, the shocks are expected to be collisionless. In the following, we assume that the thickness is infinitesimally small for simplicity.

Regions where the shock wave does not pass yet and passes are called a shock up and down stream, respectively, because a direction of fluid flow is from the up to down stream in the rest frame of the shock. A relation between the physical quantities in the shock up and down stream at the shock front is calculated from conservation laws of mass, momentum, and energy, i.e., the Euler equations:

$$\frac{\partial \rho}{\partial t} + \nabla \cdot (\rho \boldsymbol{u}) = 0, \tag{2.1}$$

$$\frac{\partial \boldsymbol{u}}{\partial t} + (\boldsymbol{u} \cdot \nabla)\boldsymbol{u} = -\frac{1}{\rho}\nabla P, \tag{2.2}$$

$$\frac{\partial}{\partial t}\left[\rho\left(\frac{1}{2}v^2 + \epsilon\right)\right] + \nabla \cdot \left[\rho \boldsymbol{u}\left(\frac{1}{2}u^2 + \epsilon + \frac{P}{\rho}\right)\right] = 0, \tag{2.3}$$

where ρ is the mass density, $\boldsymbol{u}$ is the fluid velocity, P is the pressure, ϵ is the internal energy per unit mass, and t is the time. Assume that the shock is plane parallel and static, and the fluid velocity is normal to the shock front. Using equations (2.1) and (2.2), conservations of mass and momentum fluxes at the shock front are represented by

$$\rho_1 u_1 = \rho_2 u_2, \tag{2.4}$$

$$\rho_1 u_1^2 + P_1 = \rho_2 u_2^2 + P_2, \tag{2.5}$$

respectively, where characters "1" and "2" represent quantities in the shock up and down-stream region, respectively. In the rest frame of the shock, $-u_1$ is the shock velocity, V_s. The energy flux is also conserved at the shock front when the shock is adiabatic, i.e. radiative cooling in a shock transition region is negligible. This conservation law is represented by

$$\rho_1 u_1 \left(\frac{1}{2}u_1^2 + \epsilon_1 + \frac{P_1}{\rho_1}\right) = \rho_2 u_2 \left(\frac{1}{2}u_2^2 + \epsilon_2 + \frac{P_2}{\rho_2}\right). \tag{2.6}$$

When the fluid element is ideal gas, the equation of state (EOS) is given by $P = (\gamma_\mathrm{ad} - 1)\rho\epsilon$ with the adiabatic index of γ_ad, which is 5/3 for monoatomic gas, and $\epsilon + P/\rho = \gamma_\mathrm{ad} P/[(\gamma_\mathrm{ad} - 1)\rho]$. Transforming equations (2.4), (2.5), and (2.6) using the EOS, we get

$$r = \frac{\rho_2}{\rho_1} = \frac{u_1}{u_2} = \frac{(\gamma_\mathrm{ad}+1)\mathcal{M}_1^2}{(\gamma_\mathrm{ad}-1)\mathcal{M}_1^2 + 2}, \tag{2.7}$$

$$\frac{p_2}{p_1} = \frac{2\gamma_\mathrm{ad}\mathcal{M}_1^2 - (\gamma_\mathrm{ad}-1)}{\gamma_\mathrm{ad}+1}, \tag{2.8}$$

where r is the compression ratio and $\mathcal{M}_1 = u_1/c_{\mathrm{s},1}$ is the acoustic Mach number in the rest frame of shock up stream and $c_{\mathrm{s},1} = (\gamma_\mathrm{ad} P_1/\rho_1)^{1/2}$ is the sound speed. Equations (2.7) and (2.8) are called Rankine-Hugoniot relation.

In case of the blast wave of SNRs, since u_1 is initially about 10^4 km s^{-1} and $c_{\mathrm{s},1}$ is typically 10 km s^{-1}, $\mathcal{M}_1 \sim 10^3$. The Rankine-Hugoniot relation of r at such high Mach number shock reduces to $r = (\gamma_\mathrm{ad}+1)/(\gamma_\mathrm{ad}-1)$, which is 4 for $\gamma_\mathrm{ad} = 5/3$. The temperature T_2 in the down stream of high Mach number shock can be obtained by using above relations as,

$$\begin{aligned} \frac{T_2}{T_1} &= \frac{p_2\rho_1}{p_1\rho_2} = \frac{[2\gamma_\mathrm{ad}\mathcal{M}_1^2 - (\gamma_\mathrm{ad}-1)][(\gamma_\mathrm{ad}-1)\mathcal{M}_1^2 + 2]}{(\gamma_\mathrm{ad}+1)^2\mathcal{M}_1^2} \\ &\sim \frac{2\gamma_\mathrm{ad}(\gamma_\mathrm{ad}-1)\mathcal{M}_1^2}{(\gamma_\mathrm{ad}+1)^2} = \frac{2(\gamma_\mathrm{ad}-1)}{(\gamma_\mathrm{ad}+1)^2}\frac{m_i u_1^2}{kT_1}, \end{aligned} \tag{2.9}$$

where k is the Boltzmann constant, m_i is the mass of the component of gas, and we consider $\mathcal{M}_1 \gg 1$ for the second expression. When the gas contains some components, the average temperature, T_s, just behind the shock front is give by

$$T_\mathrm{s} = \frac{T_{2,i}}{\sum_i n_i} \sim \frac{2(\gamma_\mathrm{ad}-1)}{(\gamma_\mathrm{ad}+1)^2}\frac{\mu_\mathrm{a} m_\mathrm{p} u_1^2}{kT_1}, \tag{2.10}$$

where $\mu_{\rm a}$ is the mean atomic weight and $m_{\rm p}$ is the proton mass. For fully-ionized gas with the cosmic-abundances (Allen 1973 [18]), $\mu_{\rm a} \sim 0.6$.

In the above, we neglect a magnetic field. Considering magnetic field in a framework of ideal magneto-hydrodynamics, the compression ratio is $(\gamma_{\rm ad}+1)/(\gamma_{\rm ad}-1)$ for high Mach number shock. A relation of magnetic field strength between the shock up and down stream for high Mach number shock is given by

$$\begin{aligned} \frac{B_{2,\perp}}{B_{1,\perp}} &= \frac{(\gamma_{\rm ad}+1)}{(\gamma_{\rm ad}-1)} \\ \frac{B_{2,\parallel}}{B_{1,\parallel}} &= 1, \end{aligned}$$

where $B_\perp$ and $B_\parallel$ is the magnetic field component normal and parallel to the perpendicular direction to the shock front. In ideal magneto-hydrodynamics, the magnet field lines are frozen in the plasma. Hence, $B_\perp$ increases linearly with the compression ratio.

2.2.2 Free Expansion Phase

In the free expansion phase, a thin shell of blasts-shocked CSM and reverse-shocked ejecta are formed. The shell is driven by ram pressure of the ejecta to propagate outward. Assuming spherical symmetric evolution for simplicity, the equation of motion of the shell is given by

$$\begin{aligned} \frac{d}{dt}\left(M_{\rm sh}\frac{dR}{dt}\right) &= 4\pi(R_{\rm r}^2 P_{\rm r} - R^2 P_{\rm b}) \\ &\simeq 4\pi R^2 (P_{\rm r} - P_{\rm b}), \end{aligned} \tag{2.11}$$

where t is the elapsed time after the explosion, $M_{\rm sh}$ is the shell mass, $R_{\rm r}$ is the reverse-shock radius, R is the blast-wave radius, and $P_{\rm r}$ and $P_{\rm b}$ are the pressure on the shell through a surface of the reverse shock and blast wave, respectively. In the second expression, we assume $R_{\rm r} \simeq R$. The shell mass is divided into the shocked CSM mass, $M_{\rm b}$, and the shocked-ejecta mass, $M_{\rm r}$. Assuming that the density distribution of CMS is

$$\rho_{\rm CSM} = A r^{-s},\ s < 3 \tag{2.12}$$

where r is the radial coordinate, we get

$$M_{\rm b} = \frac{4\pi A}{3-s} R^{3-s}. \tag{2.13}$$

If the progenitor is a massive star, the CSM is expected to be composed of stellar wind matter blown in pre-SN phase. In case of the spherically symmetric wind blows at a constant velocity of $v_{\rm w}$ and a constant mass-loss rate of $\dot{M}$, $A = \dot{M}/4\pi v_{\rm w}$ and $s = 2$. On the other hand, $M_{\rm b}$ is calculated from density distribution of ejecta. The radial distribution of ejecta is nearly flat at relatively inner part, called core, and can be approximate as a power-law of radius at outer part, called envelope. If the ejecta expand uniformly, i.e.,

$$u = \frac{r}{t}, \tag{2.14}$$

the density distribution of envelope is given by

$$\rho_{\rm env} = \left(\frac{r}{U_{\rm c}t}\right)^{-n} t^{-3},\ n > 5, \tag{2.15}$$

where $U_{\rm c}$ is of the order of 10^9 in cgs unit. Using this distribution, we get

$$M_{\rm r} \simeq \frac{4\pi U_{\rm c}^n}{3-n} t^{-3+n} R^{3-n}. \tag{2.16}$$

The pressure of $P_{\rm b}$ and $P_{\rm r}$ are the ram pressure of CSM entering into a blast wave,

$$P_{\rm b} = \rho_{\rm CSM}(R)\frac{dR^2}{dt}, \tag{2.17}$$

and of ejecta,

$$P_{\rm r} = \rho_{\rm env}(R)\left(\frac{R}{t} - \frac{dR}{dt}\right)^2, \tag{2.18}$$

respectively, where $dR/dt - R/t$ is the relative velocity between the reverse shock and unshocked ejecta just ahead of the shock. Using equations (2.13), (2.16), (2.17), and (2.17), we can solve equation 2.11. A solution of equation (2.11) is given by

$$R = \left[\frac{U_{\rm c}^n(3-s)(4-s)}{A(n-3)(n-4)}\right]^{1/(n-s)} t^m,\ m = \frac{(n-3)}{(n-s)}. \tag{2.19}$$

Since $U_{\rm c}^n \propto M_{\rm ej}^{(5-n)/2} E_{\rm ej}^{(n-3)/2}$, R is proportional to $M_{\rm eje}^{(5-n)/2(n-s)}\ E_{\rm ej}^{(n-3)/2(n-s)}\ A^{-1/(n-s)}$ and varies little with these quantities.

The dependence of R on t can be calculated from the dimensional analysis. Characteristic quantities of SNR in the free expansion phase are $\rho_{\rm env}$ and $\rho_{\rm CSM}$. A non-dimensional variable that made from these two quantities is $\eta = \rho_{\rm CSM}/\rho_{\rm env}$. Solving η with respect to r and substituting R for r, we get that $R = (\eta U_{\rm c}^n/A)^{1/(n-s)} t^{(n-3)/(n-s)}$, which is the same time dependence of R as equation (2.19).

In the above, we neglect an inner structure of a shell between the blast wave and reverse shock. The inner structure can be obtained by solving equations (2.1), (2.2), and (2.3) (Euler equations) with self-similar analysis using η (Chevalier 1982 [47]). We show the self-similar solution calculated for $\gamma_{\rm ad} = 5/3$, $n = 6$, and $s = 0$, 2 in figure 2.2a. When $s > 2$, the density diverges at contact discontinuity between the ejecta and CSM, as shown in left panel of figure 2.2a, because the density distribution of CSM diverges at $r = 0$. Such divergence does not present when $s = 0$, as shown in right panel of figure 2.2a. A thickness of the shell increases with the value of s, as suggested by figure 2.2a. We show a ratio of the thickness to R in figure 2.2b. The thickness increases with a decrease in the value of n, and reaches 30% of R.

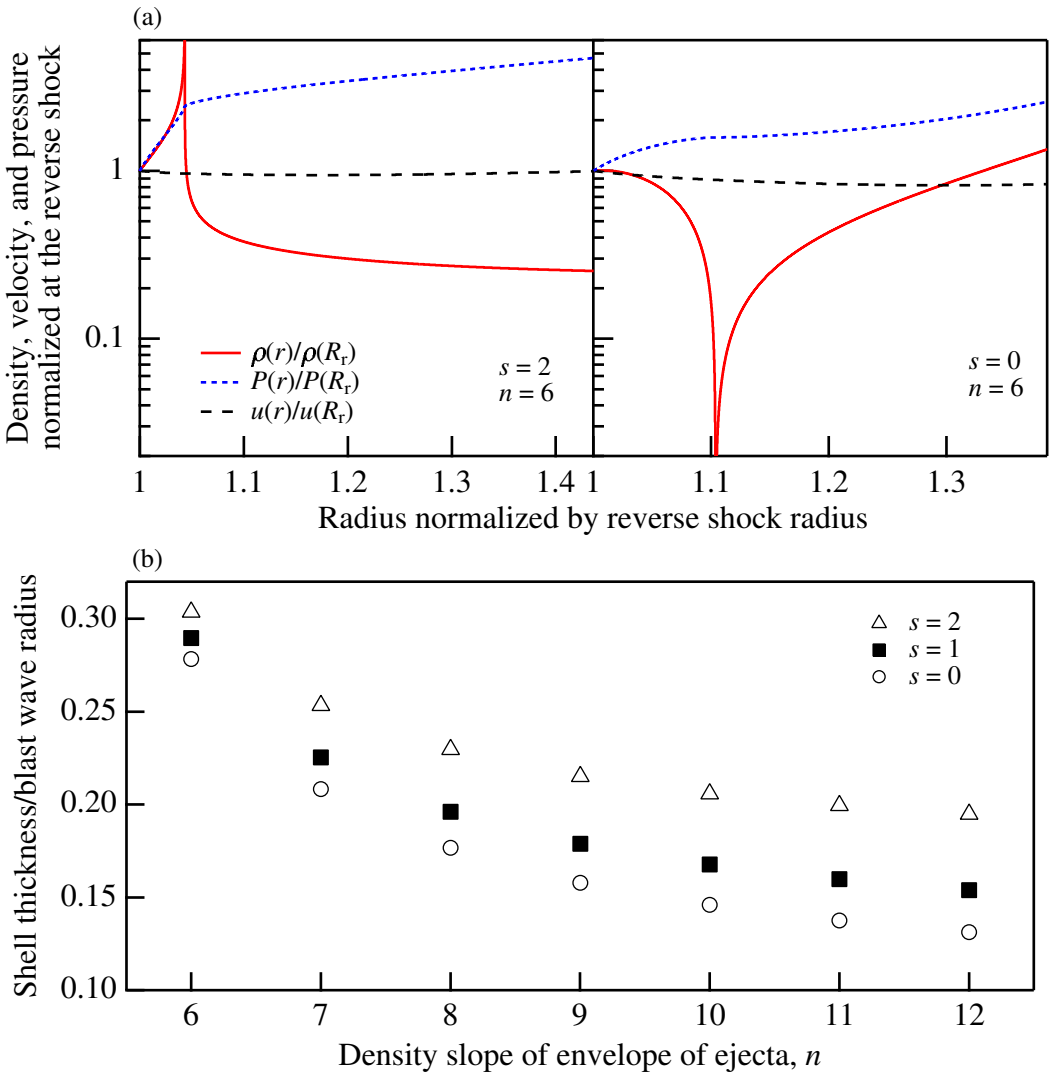

Figure 2.2: (a) Radial distribution of density (red solid line), pressure (blue dotted line), and fluid velocity (black broken line) in the shell between the blast wave and reverse shock, calculated for $\gamma_{\rm ad} = 5/3$, $n = 6$, $s = 0$, 2. These physical quantity is normalized by values at the reverse shock, $R_{\rm r}$. The contact discontinuity is located at which the normalized radius is 1.04 for $s = 2$ and 1.1 for $s = 0$. (b) Thickness of the shell between the blast wave and reverse shock, normalized by the blast wave radius vs. density slope of envelope of ejecta, calculated for $s = 0, 1, 2$.

2.2.3 Sedov-Taylor Phase

The ejecta continue to give the kinetic and thermal energies to the blast-shocked matter increasing in mass with an expansion of SNR by pushing them. Owing to a reaction of the pushing, the reverse shock propagates inside the core of ejecta at around a time when the mass of blast-shocked matter is comparable with that of ejecta, and then reaches the center of SNR. After that, the blast-shocked matter determine dynamical evolution of the SNR. The shocked matter have relatively high density near the blast wave because of shock-compression, but low density and hence high temperature in the central part of SNR because of expansion. Such high density shell is driven by the thermal pressure of the hot matter in the central part. Assuming spherical evolution and uniform ISM with density of $\rho_{\rm ISM}$, we solve the equation of motion of the shell by use of equation (2.11). The mass of the shell is given by

$$M_{\rm sh} = \frac{4\pi R^3 \rho_{\rm ISM}}{3}. \tag{2.20}$$

The thermal pressure, $P_{\rm th}$, can be written by $P_{\rm th} = (\gamma - 1)E_{\rm th}/V$, where $E_{\rm th}$ is the thermal energy and V is the volume of SNR. Assuming that $E_{\rm th} = E_{\rm ej}$ for simplicity, the thermal pressure is given by

$$P_{\rm th} = \frac{E_{\rm ej}}{2\pi R^3}. \tag{2.21}$$

Substituting equation (2.20) into equation (2.11), replacing $P_{\rm r}$ in equation (2.11) by equation (2.21), and neglecting $P_{\rm b}$ because of lower blast-wave velocity than in free expansion phase, we get a solution of equation of motion:

$$R = \left(\frac{25}{4\pi}\right)^{1/5} \left(\frac{E_{\rm ej}}{\rho_{\rm ISM}}\right)^{1/5} t^{2/5}. \tag{2.22}$$

This dependent of R on $E_{\rm ej}$, $\rho_{\rm ISM}$, and t is also derived by self-similar analysis considered below.

The self-similar analysis gives the dependence of R and also an inner distribution of physical quanteties of SNR. In the Sedov-Taylor phase, physical quantities influence the evolution of SNR is only $E_{\rm ej}$ and $\rho_{\rm ISM}$. A non-dimensional variable, ξ made by combination of these two quantities, R, and t is only $\xi = Rt^{-2/5}E_{\rm ej}^{-1/5}\rho_{\rm ISM}^{2/5}$. Solving this equation for R, we get

$$\begin{aligned} R &= \xi \left(\frac{E_{\rm ej}}{\rho_{\rm ISM}}\right)^{1/5} t^{2/5} \\ &= 8.4 \left(\frac{E_{\rm ej}}{10^{51}\ {\rm erg}}\right)^{1/5} \left(\frac{\rho_{\rm ISM}}{0.1 m_{\rm p}\ {\rm cm}^{-3}}\right)^{1/5} \left(\frac{t}{10^3\ {\rm yr}}\right)^{2/5}\ {\rm pc}, \end{aligned} \tag{2.23}$$

where ξ is a constant that determined from energy conservation and is ~ 1.15. The velocity,

$V_{\rm s}$, of blast wave is given by the time derivative of R:

$$\begin{aligned} V_{\rm s} = \frac{dR}{dt} &= \frac{2}{5}\xi \left(\frac{E_{\rm ej}}{\rho_{\rm ISM}}\right)^{1/5} t^{-3/5} \\ &= 3300 \left(\frac{E_{\rm ej}}{10^{51}\ {\rm erg}}\right)^{1/5} \left(\frac{\rho_{\rm ISM}}{0.1 m_{\rm p}\ {\rm cm}^{-3}}\right)^{1/5} \left(\frac{t}{10^3\ {\rm yr}}\right)^{-3/5}\ {\rm km\ s}^{-1}. \end{aligned} \tag{2.24}$$

Using equation (2.23), we estimate a time-scale of transition between free expansion to Sedov-Taylor phase. Such transition occurs at around a radius, $R_{\rm dyn}$, that determined by $(4\pi R_{\rm din}^3 \rho_{\rm ISM}/3) \sim M_{\rm ej}$. The solution of this equation for $R_{\rm dyn}$ is

$$R_{\rm dyn} = \left(\frac{3M_{\rm ej}}{4\pi\rho_{\rm ISM}}\right)^{1/3} = 4.6 \left(\frac{M_{\rm ej}}{1M_\odot}\right)^{1/3} \left(\frac{\rho_{\rm ISM}}{0.1 m_{\rm p}\ {\rm cm}^{-3}}\right)^{-1/3}\ {\rm pc}. \tag{2.25}$$

Substituting this equation to the equation (2.23), we get the transition time-scale by

$$\begin{aligned} t_{\rm dyn} &= \left(\frac{1}{\xi}\right)^{5/2} \left(\frac{3}{4\pi}\right)^{5/6} E_{\rm ej}^{-1/2} M_{\rm ej}^{5/6} \rho_{\rm ISM}^{-1/3}, \\ &= 220 \left(\frac{E_{\rm ej}}{10^{51}\ {\rm erg}}\right)^{-1/2} \left(\frac{M_{\rm ej}}{1M_\odot}\right)^{5/6} \left(\frac{\rho_{\rm ISM}}{0.1 m_{\rm p}\ {\rm cm}^{-3}}\right)^{-1/3}\ {\rm yr}. \end{aligned} \tag{2.26}$$

The distribution of density, pressure, and fluid velocity can be calculated by self-similar analysis using equation (2.11) and Euler equations (equations (2.1), (2.2), and (2.3)). We define a self-similar variable, λ, by

$$\lambda = \frac{r}{R} = \frac{\rho_{\rm ISM}^{1/5}}{\xi E_{\rm ej}^{1/5}} \frac{r}{t^{2/5}}, \tag{2.27}$$

and dimensionless functions V, Ω, and Π by

$$u(r,t) = \frac{r}{t} U(\lambda), \quad \rho(r,t) = \rho_{\rm ISM}\Omega(\lambda), \quad P(r,t) = \rho_{\rm ISM}\frac{r^2}{t^2}\Pi(\lambda). \tag{2.28}$$

Using equations (2.27) and (2.28), Euler equations are transformed into dimensionless form:

$$\begin{aligned} 3U + \frac{dU}{d\ln\lambda} + \left(U - \frac{2}{5}\right)\frac{d\ln\Omega}{d\ln\lambda} &= 0, \\ U(U-1) + 2\frac{\Pi}{\Omega} + \left(U - \frac{2}{5}\right)\frac{dU}{d\ln\lambda} + \frac{1}{\Omega}\frac{d\Pi}{d\ln\lambda} &= 0, \\ 2(U-1) + \left(U - \frac{2}{5}\right)\frac{d\ln\Pi}{d\ln\lambda} - \gamma\left(U - \frac{2}{5}\right)\frac{d\ln\Omega}{d\ln\lambda} &= 0. \end{aligned} \tag{2.29}$$

Assuming Rankine-Hugoniot relation of compression ratio of 4 as a boundary condition to these equations, we numerically solve the equations. Upper panel of figure 2.3 shows the

distribution of $\rho(r)/\rho(R)$, $P(r)/P(R)$, and $u(r)/u(R)$. The density is concentrated near the shock front as mentioned above. Using this density distribution, we calculate X-ray emission measure, which is defined by the integration of ρ^2 along the line of sight, and show the result in lower panel of figure 2.3. The emission measure is proportional to X-ray surface brightness, explained in section 2.3. The emission measure have a peak at $r = 0.96R_{\rm b}$ and decreases by a factor of one third at central region.

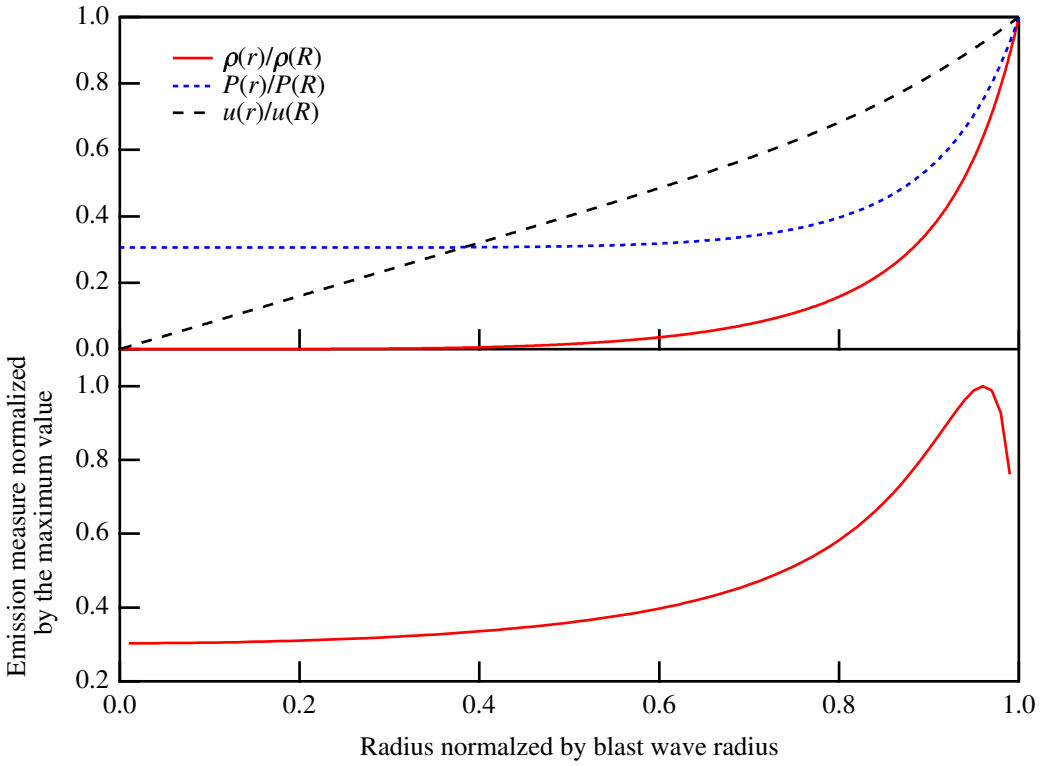

Figure 2.3: Upper: Radial distribution of density (red solid line), pressure (blue dotted line), and fluid velocity (black broken line). These physical quantity is normalized by values at the blast wave. Lower: Radial distribution of emission measure calculated from the density distribution in upper panel. The emission measure is normalized by its maximum value.

2.2.4 Radiative Phase

In the Sedov-Taylor phase, the shock temperature decreases with time as $t^{-6/5}$. As the temperature decreases, a time-scale, $t_{\rm cool}$, of radiative cooling of shocked matter decreases because $t_{\rm cool}$ is given by $(3nkT/2)/8n^2\Lambda(T) \propto T/\Lambda(T)n \propto T^{1-\alpha}$, where $\Lambda(T)$ is the radiative cooling function and α is smaller than 0.5 for cosmic abundance gases. After $t_{\rm cool}$ becomes smaller than the age of SNR, the cooling affects the dynamical evolution SNR. The dynamical evolution of SNR may be modeled by expansion of a cold dense shell formed by the cooling involving collapse of the matter behind the blast wave. On the other hand, gas at the inner part of the SNR is hotter than the shell because the radiative cooling of the gas is less efficient

due to low density. The hot gas pushes the cold shell by the thermal pressure, so that the blast wave continues to expand. Assuming that spherical symmetric evolution and uniform ISM, a mass of the dense shell is proportional to R^3 (equation (2.20)). A thermal pressure of the hot inner gas is proportional to $V^{-\gamma_{\rm ad}} \propto R^{-5}$ for adiabatic gas of index of 5/3. Using these proportional relation, we can solve equation of motion, and get that $R \propto t^{2/7}$ (McKee and Ostriker 1977 [124]).

The dynamical evolution of SNR in radiative phase is numerically investigated by several authors (e.g., Chevalier 1974 [46]; Blondin et al. 1998 [35]). An one dimensional calculation for $\gamma_{\rm ad} = 5/3$ of Blondin et al. (1998) [35] showed that R is nearly proportional to $t^{0.33}$ in the radiative phase. They discussed that large value of 0.33 than 2/7 is due to heating of the hot inner gas by reverse shock propagate inward after the dense colds shell are formed.

A time-scale, $t_{\rm tr}$, of transition from adiabatic to radiative phase is estimated by equating $t_{\rm cool}$ with the age, $t_{\rm age}$, of the SNR. Blondin et al. (1998) [35] calculated $t_{\rm tr}$ by approximating $\Lambda(T)$ as $\sim 10^{-16} T^{-1}$ erg cm^3 s^{-1} for fully-ionized solar-abundance gas and taking the shock temperature $kT_{\rm s} = 3\mu_{\rm a} m_{\rm p} V_{\rm s}^2/16$ as a temperature of shocked matter:

$$t_{\rm tr} = 2.9 \times 10^4 \left(\frac{E_{\rm ej}}{10^{51}\ {\rm erg}}\right)^{4/17} \left(\frac{n_{\rm ISM}}{1\ {\rm cm}^{-3}}\right)^{-9/17}\ {\rm yr}. \tag{2.30}$$

At $t_{\rm tr}$, the radius of the blast wave and the shock temperature are

$$R(t = t_{\rm tr}) = 19 \left(\frac{E_{\rm ej}}{10^{51}\ {\rm erg}}\right)^{5/17} \left(\frac{n_0}{1\ {\rm cm}^{-3}}\right)^{-7/17}\ {\rm pc}, \tag{2.31}$$

and

$$T_{\rm s}(t = t_{\rm tr}) = 8.9 \times 10^5 \left(\frac{\mu_{\rm a}}{0.6}\right) \left(\frac{E_{\rm ej}}{10^{51}\ {\rm erg}}\right)^{2/17} \left(\frac{n_0}{1\ {\rm cm}^{-3}}\right)^{4/17}\ {\rm K} \tag{2.32}$$

respectively.

The gases near the shock front at which the radiative cooling is efficient can not be treated as an ideal gas with $\gamma_{\rm ad} = 5/3$. Such gases can approximately treated as a gas of adiabatic index smaller than 5/3. The smaller index means a compression ratio higher than 4 (see section 2.2.1). The change of spectral index affect a spectrum of accelerated particles, explain in section 2.4.

2.3 Thermal Evolution of Supernova Remnant

X-ray emission from a SNR reflect thermal evolution in a shock down stream region. As shown in section 2.2.1, components of plasma are heated to temperature proportional their masses at the shock front. If collisionless heating mechanisms that bring the components into thermal equlibrium at the front (e.g., McKee 1974 [123]) do not work, the plasma in the shock down stream is in thermal non-equilibrium state. The slowest relaxation process toward the equlibrium is Coulomb collisions. Equation of thermal transport from protons

to electrons is given by (e.g., Spitzer 1962 [172])

$$\frac{dT_{\rm e}}{dt} = \frac{8Z_{\rm i}^2 e^4 (2\pi m_{\rm e})^{1/2} n_{\rm i} \ln\Lambda}{3k_{\rm b}^{3/2} m_{\rm i}} \frac{(T_{\rm i} - T_{\rm e})}{[T_{\rm e} + (m_{\rm e}/m_{\rm i})T_{\rm i}]^{3/2}}, \tag{2.33}$$

where $\ln\Lambda$ is the Coulomb logarithm,

$$\ln\Lambda = 30.7 + \ln\left[\left(\frac{n_{\rm e}}{1\ {\rm cm}^{-3}}\right)^{-1/2}\left(\frac{kT_{\rm e}}{10^7\ {\rm K}}\right)\right]. \tag{2.34}$$

This equation can be solved analytically but a solution is complicated. When $(m_{\rm e}/m_{\rm i})T_{\rm i} \ll T_{\rm e} \ll T_{\rm i}$, the equation (2.33) is approximated as $dT_{\rm e}/dt \propto n_{\rm i}T_{\rm i}T_{\rm e}^{-3/2}$ and a solution is simple. If this is the case, the solution is approximated by $T_{\rm e} \sim 0.8 n_{\rm e}^{2/5} t^{2/5} T_{\rm s}^{2/5}$ K (Masai 1994 [121]). Solving this solution for t and substituting 10^7 K for $T_{\rm e}$, we get a time-scale, $t_{\rm heat}$, of electron heating up to the temperature at which the plasma emit X-rays:

$$t_{\rm heat} \sim 10^9 \left(\frac{n}{1\ {\rm cm}^{-3}}\right)^{-1}\left(\frac{T_{\rm e}}{10^7\ {\rm K}}\right)^{5/2}\left(\frac{T_{\rm s}}{10^9\ {\rm K}}\right)\ {\rm s}. \tag{2.35}$$

In interstellar space, elements heavier than proton present. Such elements may reduce $t_{\rm heat}$ because their temperature just behind the shock is high. Most abundant heavy element is helium (e.g., Allen 1973 [18]). In order to an effect of present of helium on thermal evolution, we compare the temperature evolution through Coulomb collisions of plasma that comprises electron and proton with electron, proton, and fully-ionized helium with cosmic abundance (Allen 1973 [18]). Figure 2.4 shows the temperature evolutions of these two plasmas with $n_{\rm p} = 1\ {\rm cm}^{-3}$. Initial temperatures of the electrons, protons, and helium are $(3m_{\rm e}V_{\rm s}^2/16k)$, $(3m_{\rm p}V_{\rm s}^2/16k)$, and $(3m_{\rm He}V_{\rm s}^2/16k)$ with $V_{\rm s} = 3 \times 10^3$ km s^{-1}, respectively, where $m_{\rm He}$ is the helium mass. The electron temperature increases with time as $t^{2/5}$, as mentioned in above, when the time is in the range from $\sim 10^{-1}$ yr to $\sim 10^4$ yr for each plasma. The effect of presence of helium on the evolution of electron temperature is small, as shown in figure 2.4.

The electron temperature evolves with time as $T_{\rm e} \propto t^{2(2-s)(n-3)/5(n-s)-2/5}$ in the free expansion phase and $T_{\rm e} \propto t^{-2/25}$ in the Sedov-Taylor phase (Masai 1994 [121]). In figure 2.5, we compare the temperature of electron heated by Coulomb collisions in the post-shock region (solid lines) and that of electron equilibrate with ion at the shock front (broken lines) with the observed electron temperature (circles). One can see that the transfer by Coulomb collisions from ions to electrons is a reasonable assumption to account for the observed data.

The heated electrons in the shock down stream ionize ion by collisions. A time-scale, $t_{\rm ion}$, of ionization by electron collision is given by (Masai 1984 [120]),

$$t_{\rm ion} \sim 10^{12}\left(\frac{n}{1\ {\rm cm}^{-3}}\right)^{-1}\ {\rm s}. \tag{2.36}$$

This time-scale is longer than $t_{\rm heat}$. Hence X-ray emitting plasma is an under-ionizing/ionizing state, or nearly collisional ionization equilibrium state at late time. Using the ionization temperature, $T_{\rm z}$, which is the plasma temperature in collisional ionization equilibrium having the relevant ionization state, the under-ionized state is represented by $T_{\rm z} < T_{\rm e}$.

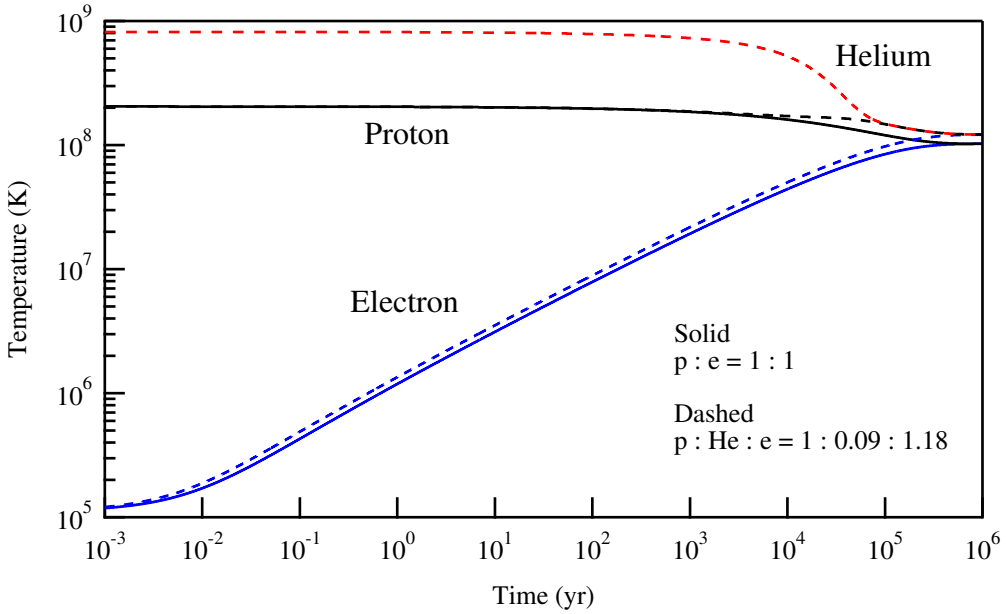

Figure 2.4: Time evolution of plasma temperature through Coulomb collision, calculated for the number density of protons of 1 cm^{-3} and the initial temperatures of each component given by Rankine-Hugoniot relation for the shock velocity of 3×10^3 km s^{-1}. Solid and dashed lines represent temperature evolution of electron-proton plasma with the number ratio of 1 to 1 and that of fully-ionized electron-proton-helium plasma of which number ratio is given by the cosmic abundances (Allen 1973 [18]).

2.3.1 Thermal Emission

In the adiabatic phase, thermal emissions from SNR are observed in X-ray band because the temperature is more than 10^6 K. The X-ray emitting plasma of SNR is optically thin because of low density. Thermal emission from such plasma is due to three types of transtions: free-free (bremsstrahlung), free-bound (recombination radiation), and bound-bound (line emission).

Charged particles interact with another charged particles through Coulomb force emit bremsstrahlung. Since the bremsstrahlung by collisions between like particles is zero in the dipole approximation, which is valid when the particle energies are non-relativistic, we consider collisions between the different kind of particles, i.e., electrons and ions. When the electrons have the Maxwell velocity distribution and the ions are at rest, the spectrum of bremsstrahlung photons is given by (e.g., Rybicki and Lightman 1979 [158])

$$\begin{aligned} \frac{dW}{dV\,dt\,d\nu} &= \frac{2^{11/2}\pi^{3/2}e^6}{3^{3/2}k^{1/2}m_{\rm e}^{3/2}c^3}\bar{g}_{\rm ff}Z_{\rm i}^2 n_{\rm i}n_{\rm e}T_{\rm e}^{-1/2}\exp\left(-\frac{h\nu}{kT_{\rm e}}\right) \\ &= 6.8\times10^{-38}\bar{g}_{\rm ff}Z_{\rm i}^2 n_{\rm i}n_{\rm e}T_{\rm e}^{-1/2}\exp\left(-\frac{h\nu}{kT_{\rm e}}\right) \end{aligned} \tag{2.37}$$

where $Z_{\rm i}$ is the charge of ion and $\bar{g}_{\rm ff}$ is a velocity average Gaunt factor. The Gaunt factor is of the order of unity at $h\nu/kT \sim 1$ and is in the range of $1-5$ for $10^{-3} < h\nu/kT < 1$

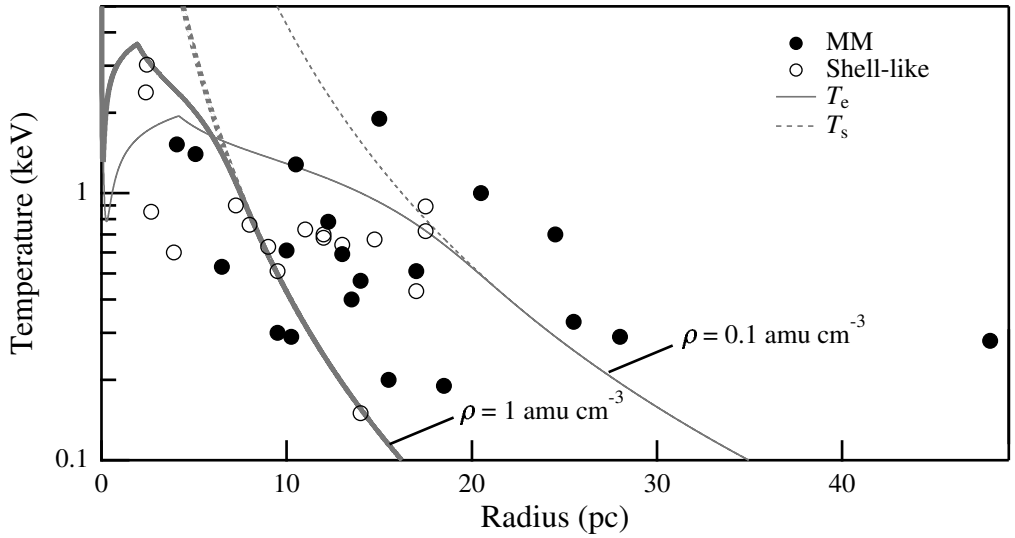

Figure 2.5: Electron temperature vs. radius of SNRs that have no active central sources. Open and filled circles represent shell-like and mixed-morphology SNRs, respectively. The thin and thick solid/broken lines represent the calculations for the density $\rho = 0.1$ amu cm^{-3} and $\rho = 1$ amu cm^{-3}, respectively, of the ambient matter.
References – Kepler: Kinugasa and Tsunemi 1999 [108], G15.9+0.2: Reynolds et al. 2006 [150], G27.4+0.0: Gotthelf and Vasisht 1997 [78], Cygnus Loop: Miyata et al. 2007 [127], G78.2+2.1: Uchiyama et al. 2002 [187], Landecker, Roger, and Higgs 1980 [115] G109.1+1.0: Sasaki et al. 2004 [162], Cassiopeia A: Kawasaki et al. 2005 [105], Tycho: Hwang and Gotthelf 1997 [92], Puppis A: Tamura 1995 [177], G272.2-3.2: Harrus et al. 2001 [85], G296.1+0.5: Castro et al. 2011 [44], G299.2-2.9: Park et al. 2007 [140], RCW 86: Rho et al. 2002 [154], SN 1006: Yamaguchi et al. 2008 [201], Lupus Loop: Park et al. 2009 [139], CTB 37 B: Nakamura et al. 2009 [131], G349.7+0.2: Lazendic et al. 2005 [116], W 28: Sawada and Koyama [164], W 44: Uchida et al. 2012 [184], 3C400.2: Saken et al. 1995 [161], Kes 27: Enoguchi et al. 2002 [58], MSH 11-61 A: Rho and Petre 1998 [153], 3C 391: Kawasaki et al. 2005 [105], CTB 1: Rho and Petre 1998 [153], W 51 C: Hanabata et al. 2013 [84], W 63: Rho and Petre 1998 [153], HB 21: Rho and Petre 1998 [153], IC 443: Yamaguchi et al. 2009 [202], Kes 79: Rho and Petre 1998 [153], HB 3: Rho and Petre 1998 [153], G156.2+5.7: Katsuda et al. 2009 [101], W 49 B: Ozawa et al. 2009 [136], 3C 397: Rho and Petre 1998 [153], G344.7-0.1: Yamaguchi et al. 2012 [203], G346.6-0.2: Yamauchi et al. 2013a [204], G352.7-0.1: Giacani et al. 2009 [73], G359.1-0.5: Ohnishi et al. 2011 [134].

(Karzas and Latter 1961 [97]). Integrating this bremsstrahlung spectrum, we get

$$P = \int \frac{dW}{dVdtd\nu} d\nu = 1.4 \times 10^{-27} \bar{g}_{\rm ff} n_{\rm e} n_{\rm i} T_{\rm e}^{1/2}. \tag{2.38}$$

Integrating this equation along the line of sight, we get a surface brightness of bremsstrahlung. When the temperature varies little through the line of sight, the surface brightness is proportional $\int n_{\rm e} n_{\rm i} dl$, i.e., the emission measure. The line emission and recombination radiation are proportional to the square of density as well as bremsstrahlung. Hence the emission measure is proportional to the X-ray surface brightness.

2.4 Particle Acceleration and Non-Thermal Radiation

Observations of non-thermal radio (e.g., Green 2009 [82]), X-rays (e.g., Koyama et al. 1995 [112]), and γ-rays (e.g., Giuliani et al. 2011 [77]; Ackermann et al. 2013 [9]) of SNRs show that electrons and protons are accelerated by shocks. The plausible acceleration mechanism is diffusive shock acceleration (DSA); particles gain momentum through shock crossing due to scattering by magnetic inhomogeneities (e.g., Blandford and Ostriker 1987 [33]; Bell 1978a, b [25], [26]). We describe DSA and radiation process of non-thermal particles in the following sections.

2.4.1 Particle Acceleration

Fermi (1949) [59] proposed that charged particles are accelerated by collisions with randomly-moving magnetic clouds. The particles gain and lose energy by head-on and overtaking collisions, respectively. If the speed of the cloud is $V_{\rm c}$, energy gain and loss per collision are both $\sim V_{\rm c}/c$ percent. The probability of head-on collisions is higher than the overtaking collisions by $\sim V_{\rm c}/c$ when the particles are relativistic, and hence the particle energy increases by $\sim (V_{\rm c}/c)^2$ percent per collision on average. Such stochastic acceleration mechanism is called the second-order Fermi acceleration. This acceleration may play a role in acceleration in SNR shocks when Alfvén velocity in the upstream is non-negligible in comparison with the shock velocity, i.e., Alfvén Mach number is low (Ostrowski 1999 [135]). However, in general, more efficient stochastic acceleration mechanism, called the first-order Fermi acceleration or DSA, plays a dominate role in particle acceleration near shocks. Particles with sufficiently-high energy can cross the shock owing to scattering by magnetic inhomogeneity in the shock down and up stream. The scattering is elastic in the rest frame of the down an up stream, but the particles momentum increases in the rest frame of the shock. Hence the particle momentum increases with the shock crossing. Figure 2.6 shows schematic picture of DSA.

There is two manners explaing DSA; one is the probabilistic argument by Bell (1978a, b) [25] [26] and the other is the argument using diffusion convection equation by Blandford & Ostriker (1987) [33]. We describe the former in the below.

We consider DSA of particles with initial number of N_0 and energy of E_0 using the probabilistic manner. Assume that the particles are relativistic for simplicity. DSA comprises energy gain by shock crossing and escape from ongoing acceleration region by advection from the shock front to down stream. We first calculated the energy gain rate. The energy gain of the particles per cycle of crossing and re-crossing is given by

$$\Delta E = \frac{u_1 - u_2}{c}(\cos\theta_2 - \cos\theta_1)E \tag{2.39}$$

where E is the energy of particle, θ_1 and θ_2 is scattering angle between the particle and the shock normal direction in the up and down stream, respectively. These angle satisfy a condition that $\pi/2 < \theta_1 \leq \pi$ and $0 \leq \theta_2 < \pi/2$ to cross the shock for the particles. Because the particle distribution can be approximated as an isotropic in the up and down stream, probabilities of the particle that cross the shock per unit time is proportional to $\cos\theta_1$ and

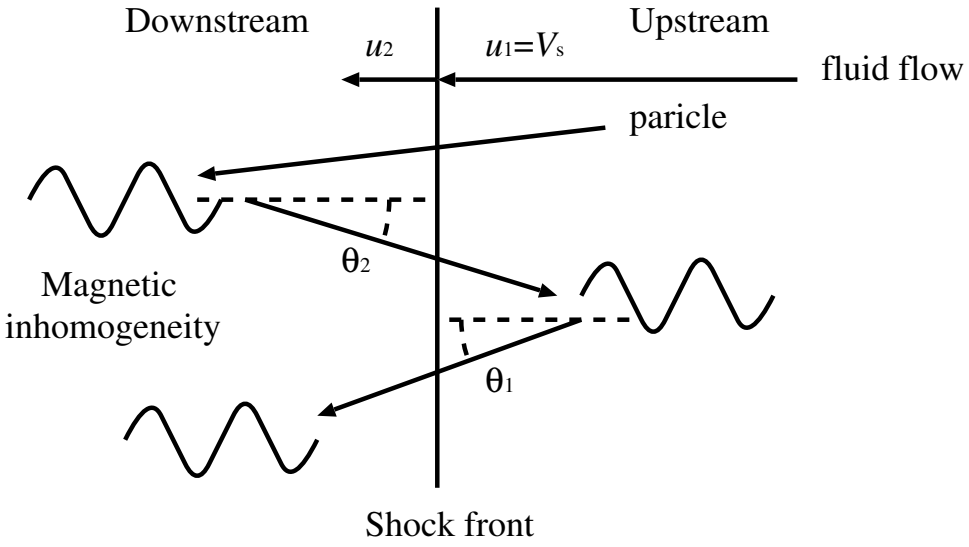

Figure 2.6: Schematic of diffusive shock acceleration.

$\cos\theta_2$, respectively. Hence average of $\cos\theta_1$ and $\cos\theta_2$ over solid angle are given by

$$\langle\cos\theta_1\rangle = \frac{\int\cos^2\theta_1 d\Omega_1}{\int\cos\theta_1 d\Omega_1} = -\frac{2}{3},\ \langle\cos\theta_2\rangle = \frac{2}{3},$$

respectively, and average of energy gain is given by

$$\langle\Delta E\rangle = \frac{4(u_1-u_2)}{3c}E. \tag{2.40}$$

After l cycles of cross and re-crossing, the energy of particles becomes

$$E_l = E_0\left(1+\frac{4(u_1-u_2)}{3c}\right)^l. \tag{2.41}$$

Second we calculate a fraction of particles, N_l, that remain in accelerated after l cycles. Such probability can be determined by a ratio of number flux of particles cross the shock from down stream to up stream. Average speed normal to the shock of particles cross from the shock up stream is $c/2$. Because a fraction of such particles is $1/2$, the number flux of the particles is $n_s c/4$ where n_s is the number density at the shock. In the downstream, particles are advected away from the shock front at the speed of u_2 when the scattering center is fixed in the fluid, and a number flux of the advected particles is $n_s u_2$. Hence a number flux of particles that cross from downstream is a difference between these fluxes, $n_s c/4 - n_s u_2$, and the fraction is given by

$$N_l = N_0\left(1-\frac{4u_2}{c}\right)^l. \tag{2.42}$$

Using equations (2.41) and (2.42), we get

$$\frac{\ln(N_l/N_0)}{\ln(E_l/E_0)} = \frac{\ln(1-4u_2/c)}{\ln(1+4(u_1-u_2)/3c)} \sim -\frac{3u_2}{u_1-u_2} \tag{2.43}$$

Hence an integrated energy spectrum of particles is

$$N_l = N_0(E_l/E_0)^{-3u_2/(u_1-u_2)} = \int_{E_l}^{\infty} \frac{dN}{dE} dE \tag{2.44}$$

and a differential energy spectrum is

$$\frac{dN}{dE} = \frac{N_0}{E_0}(\mu - 1)\left(\frac{E}{E_0}\right)^{-\mu}, \tag{2.45}$$

$$\mu = \frac{r+2}{r-1} = \frac{(3\gamma_{\rm ad}-1)\mathcal{M}^2+4}{2(\mathcal{M}^2-1)}, \tag{2.46}$$

where $r = u_1/u_2$ is the shock compression ratio (see section 2.2.1). Therefore, the accelerated particle have power-law energy distribution.

For high Mach number shocks, $\mu = 2$ for $\gamma_{\rm ad} = 5/3$. When the shock is radiative, r can be larger than 4 because shocked matter collapses by cooling. In this case, the accelerated particles have a spectral index smaller than 2.

In the above, we restrict relativistic particles. However, the particle spectra including non-relativistic energy range can be derived using the similar probabilistic manner (Bell 1978b [26]):

$$\frac{dN}{dE} = N_0(\mu-1)(E_{\rm inj}+2mc^2E_{\rm inj})^{(\mu-1)/2}(E+mc^2)(E^2+2mc^2E)^{-(\mu+1)/2}, \tag{2.47}$$

where $E = (\gamma-1)mc^2$ is the kinetic energy and $E_{\rm inj}$ is the injection kinetic energy. This equation is valid when the particle speed is much higher than shock speed.

We estimate a maximum attainable energy, $E_{\rm max}$, of accelerated particles using the energy gain rate of equation (2.40). For the estimate, a time-scale, $t_{\rm cyc}$, of shock cross and re-cross of particles is needed. This time-scale is given by the sum of time of particles spend in the shock up and downstream (Krymsky et al. 1979 [113]):

$$t_{\rm cyc} = \frac{4}{c}\left(\frac{D_1}{u_1}+\frac{D_2}{u_2}\right), \tag{2.48}$$

where D is the diffusion coefficient. Using $t_{\rm cyc}$, the time-scale of acceleration of particles is given by

$$t_{\rm acc}^{-1} \sim \frac{\langle \Delta E\rangle}{E}\frac{1}{t_{\rm cyc}} = \frac{u_1-u_2}{3}\frac{1}{D_1/u_1+D_2/u_2}. \tag{2.49}$$

Although a sample is limited, X-ray observation suggests that particle diffusion is near Bohm limit, $D = r_{\rm g}v/3$, where $r_{\rm g}$ is the gyration radius, in shocks of SNRs (Stage et al. 2006 [173]). Assuming Bohm limit, $u_2 = u_2/4$, and $B_2 = 4B_1$, we get

$$t_{\rm acc} = \frac{8D_1}{u_1^2} = \frac{8Ec}{3eB_1u_1^2}, \tag{2.50}$$

where $E \simeq pc$ is considered in the last expression. Equating the acceleration time-scale with the age of SNR, we get

$$E_{\rm max} = 30 \left(\frac{u_1}{3 \times 10^3 \text{ km s}^{-1}} \right)^2 \left(\frac{B_1}{3\ \mu\text{G}} \right) \left(\frac{t}{10^3 \text{ yr}} \right) \text{ TeV}, \tag{2.51}$$

where 3 μG is the typical strength of interstellar magnetic field. For a fixed magnetic field strength, $E_{\rm max}$ increases with time in the free expansion phase in a case of $n + s > 6$ while decreases time as $t^{1/5}$ in the Sedov-Taylor phase. In between these two phases, $E_{\rm max}$ reaches a peak value during SNR evolution. Such value can be estimated using the time-scale of transition from the free to Sedov-Taylor phase (equation 2.26):

$$E_{\rm max}^{\rm peak} = 50 \left(\frac{E_{\rm ej}}{10^{51} \text{ erg}} \right)^{1/2} \left(\frac{M_{\rm ej}}{M_\odot} \right)^{-1/6} \left(\frac{\rho_{\rm ISM}}{0.1 m_{\rm p} \text{ cm}^{-3}} \right)^{-1/3} \left(\frac{B_1}{3\ \mu\text{G}} \right) \text{ TeV} \tag{2.52}$$

In the above, we adopt the typical interstellar value of magnetic field as the field strength in the shock up stream. However, a magnetic field amplification mechanism are proposed by Bell and Lucek (2001) [28] and Bell (2004) [27]. In the mechanism, the magnetic field in the shock up stream is amplified up to 10^3 μG by the streaming instability of cosmic-ray when the shock velocity is high. Although whether the mechanism works in SNR shocks is not clear, strong magnetic field, which is of the order of $10^2 - 10^3$ μG, is suggested by observations: X-ray filament-like structure of young shell-like SNRs (e.g, Berezhko et al. 2003 [29]; Parizot et al. 2006 [138]), time-variability of X-rays in a young shell-like SNR RX J1713.7-3946 (Uchiyama et al. 2007 [186]), and radio flux based on equipartition aurgument (e.g, Arbutina et al. 2012 [20], 2013 [21]). If the magnetic field is still $\sim 10^2$ μG at the transition phase between the free expansion and Sedov-Taylor phases, $E_{\rm max}^{\rm peak}$ reaches 10^3 TeV.

2.4.2 Synchrotron Radiation

Relativistic electron moving in a magnetic field emits synchrotron radiation. The power, $P_{\rm syn}$, of synchrotron radiation is given by

$$P_{\rm syn} = \frac{4}{3} \sigma_{\rm T} c \beta^2 \gamma^2 U_{\rm B}, \tag{2.53}$$

where $\sigma_{\rm T}$ is the Thomson scattering cross section and $U_{\rm B} = B^2/8\pi$ is the energy density of magnetic field. Because the power is proportional to the square of the energy of electrons, higher energy electrons cool faster than lower energy electrons. A time-scale, $t_{\rm syn}$, of cooling by synchrotron radiation is

$$t_{\rm syn} = \frac{\gamma m_{\rm e} c^2}{P_{\rm syn}} = \frac{3 m_{\rm e} c}{4 \sigma_{\rm T} \beta^2 \gamma U_{\rm B}} \sim 4 \times 10^8 \left(\frac{E}{100 \text{ TeV}} \right)^{-1} \left(\frac{B}{100\ \mu\text{G}} \right)^{-2} \text{ yr}. \tag{2.54}$$

A typical frequency, ν, of synchrotron photon emitted by an electron of energy of E can be estimated from a synchrotron spectrum. The power per unit volume per unit frequency

of synchrotron radiation emitted by the electron is given by (Ginzburg and Syrovatskii 1965 [75])

$$P(\nu) = \frac{\sqrt{3}e^3 B \sin\alpha}{m_{\rm e}c^2} F\left(\frac{\nu}{\nu_{\rm c}}\right), \tag{2.55}$$

where α is the pitch angle between a velocity of the electron and the magnetic field line, $F(x) = x\int_x^\infty K_{5/3}(t)dt$ is the synchrotron function defined by modified Bessel function of second kind, K_j, and $\nu_c = (3\gamma^2 eB\sin\alpha/4\pi m_{\rm e}c)$. This function $P(\nu)$ has a peak at $\nu = 0.29\nu_c$. In other word, the typical frequency of emitted synchrotron photons is given by

$$\nu \sim 1.5 \text{ GHz } \left(\frac{E}{2 \text{ GeV}}\right)^2 \left(\frac{B}{100\ \mu\text{G}}\right). \tag{2.56}$$

This means that gigahertz radio emissions that are commonly observed in SNRs are correspond to GeV electrons. Synchrotron X-ray emission that are observed in several SNRs (e.g., Koyama et al. 1995 [112]; Nakamura et al. 2012 [132]) are correspond to ~ 100 TeV electrons, because $h\nu \sim 15$ keV $(E/100 \text{ TeV})^2(B/100\ \mu\text{G})$. When the cooling by synchrotron radiation balance the momentum gain by DSA, the maximum energy, $E_{\rm max,cool}$, of electrons is

$$E_{\rm max,cool} \sim \frac{3\pi^{1/2}e^{1/2}m_{\rm e}cV_{\rm s}}{4\sigma_{\rm T}^{1/2}B^{1/2}} \sim 18 \text{ TeV } \left(\frac{V_{\rm s}}{3\times10^3 \text{ km s}^{-1}}\right)\left(\frac{B}{100\ \mu\text{G}}\right)^{-1/2}. \tag{2.57}$$

In this case, a frequency, $\nu_{\rm max,cool}$, of synchrotron radiation correspond to $E_{\rm max,cool}$ is

$$h\nu_{\rm max,cool} \sim 0.5 \text{ keV } \left(\frac{V_{\rm s}}{3\times10^3 \text{ km s}^{-1}}\right)^2, \tag{2.58}$$

which is independent of B.

When relativistic electrons have a power-law energy distribution, $N_{\rm e} = KE^{-\mu}$, a spectrum of synchrotron radiation emitted from the electrons is given by

$$\int P(\nu)N_{\rm e}(E)dE \propto KB^{(\mu+1)/2}\nu^{-\Gamma}, \Gamma = \frac{\mu-1}{2}. \tag{2.59}$$

The spectral index, Γ, is 0.5 when μ is 2, which is a value predicted by DSA for the compression ratio of 4.

2.4.3 Inverse-Compton Scattering

When a electron scatters a photon of which wavelength in the rest frame of the electron is shorter than the Compton wavelength of $(h/m_{\rm e}c)$, an energy transfer between these particles is not negligible. Such scattering is called Compton scattering. In particular, scattering by which the photon gain energy is called inverse-Compton scattering. The energy of photon after scattering by the electron with Lorentz factor of γ is about γ^2 times larger than that before the scattering.

The power, $P_{\rm IC}$, of inverse-Compton scattering photons is given by

$$P_{\rm IC} = \frac{4}{3}\sigma_{\rm T} c\beta^2\gamma^2 U_{\rm CMB}. \tag{2.60}$$

The power of inverse-Compton scattering is $U_{\rm CMB}/U_{\rm B}$ times as large as that of synchrotron emission. Because $U_{\rm CMB}/U_{\rm B}$ is about 10^{-3} for a typical magnetic field strength of 100 μG in SNRs, cooling of electrons by inverse-Compton scattering is negligible.

A spectrum of inverse-Compton photons emitted from a relativistic electron is given by (Blumenthal and Gould 1970 [36])

$$\frac{dN_\gamma}{dtdh\nu} = \frac{3c\sigma_{\rm T}}{4\gamma^2}\int \frac{h\nu}{h\nu_0} n_{\rm ph}(h\nu_0)[2x\ln x + x + 1 - 2x^2]dh\nu_0, \tag{2.61}$$

where $x = (h\nu/4\gamma^2 h\nu_0)$. When the electron distribution is $N_{\rm e} = K_{\rm e}E^{-\mu}$.

$$\int \frac{dN_\gamma}{dtdh\nu} N_{\rm e} dE \propto (h\nu)^{-(\mu-1)/2} \tag{2.62}$$

Spectral indices of inverse-Compton and synchrotron photons emitted from the same electrons are the same.

At higher energies, inverse-Compton scattering is suppressed by Klein-Nishina effect. Such effect is not important in case that an initial energy of photon, $h\nu_{\rm i}$, is much less than the the rest mass energy in the rest frame of electron, i.e., $(4\gamma h\nu_{\rm i}/m_{\rm e}c^2) \ll 1$. For CMB photons, this condition is roughly $\gamma m_{\rm e}c^2 \ll 100$ TeV. If this is not the case, inverse-Compton scattering is described by Klein-Kishina cross section instead of Thomson cross section.

2.4.4 Bremsstrahlung

When the initial and final energy of the electron is much higher than the electron rest mass energy, an energy spectrum of bremsstrahlung photons radiated through electron-proton collisions is given by (Blumenthal and Gould 1970 [36])

$$h\nu\frac{dN_\gamma}{dtdh\nu} = \frac{4Z_{\rm i}^2\alpha r_0^2 c n_{\rm T}}{E^2}\left(\frac{4}{3}E^2 - \frac{4}{3}Eh\nu + (h\nu)^2\right)\left[\ln\left(\frac{2E(E-h\nu)}{h\nu m_{\rm e}c^2}\right) - \frac{1}{2}\right], \tag{2.63}$$

where α is the fine structure constant, r_0 is the classical electron radius, and $n_{\rm T}$ is the number density of target ion. Considering bremsstrahlung through the electron-electron collisions, which have the same cross section as that through electron-proton collisions in relativistic energies of $E, E-h\nu, h\nu \gg m_{\rm e}c^2$ (Gould 1969 [79]), the energy spectrum of bremsstrahlung becomes double that given by equation (2.63) for electron-proton plasma. Integrating equation (2.63) over photon energy, we get the total power of bremsstrahlung;

$$\begin{aligned} P_{\rm bremss} &\simeq \int_0^{h\nu_{\rm max}} h\nu\frac{dN_\gamma}{dtdh\nu}dh\nu \\ &= 4Z_{\rm i}^2\alpha r_0^2 c n_{\rm T} E\left[\ln(1+2e_{\rm N}^{-1/2}\tilde{E}) + \frac{2}{3}\frac{e_{\rm N}^{-1/2}\tilde{E}(1+e_{\rm N}^{-1/2}\tilde{E})}{(1+2e_{\rm N}^{-1/2}\tilde{E})^2}\right] \\ &\simeq 4Z_{\rm i}^2\alpha r_0^2 c n_{\rm T} E\left[\ln(2\tilde{E}) - \frac{1}{3}\right], \end{aligned} \tag{2.64}$$

where $h\nu_{\rm max}$ is determined by

$$\ln\left(\frac{2E(E-h\nu_{\rm max})}{h\nu_{\rm max}m_{\rm e}c^2}\right)-\frac{1}{2}=0, \tag{2.65}$$

which is a condition that the expression in the second parenthesis in equation (2.63) is equal to zero, $\tilde{E}=E/m_{\rm e}c^2$ is the electron energy in unit of the rest mass energy, $e_{\rm N}$ is Napier's number, and $\tilde{E}\gg 1$ is considered in the last expression. Since the total power, i.e., the energy loss rate of electron, is almost proportional to the electron energy, a cooling time-scale of electron due to bremsstrahlung emission is almost independent of the energy. The time-scale is given by

$$\begin{aligned} t_{\rm brems} &\simeq \frac{1}{4Z_{\rm i}^2\alpha r_0^2 c n_{\rm T}}\left[\ln(2\tilde{E})-\frac{1}{3}\right]^{-1} \\ &\sim 6\times10^7{\rm yr}\left(\frac{Z_{\rm i}}{1}\right)^{-2}\left(\frac{n_{\rm T}}{1\ {\rm cm}^{-3}}\right)^{-1}[\ln(E/1\ {\rm GeV})]^{-1}. \end{aligned} \tag{2.66}$$

When electrons whose energy distribution is $N_{\rm e}=K_{\rm e}E^{-\mu}$ emit bremsstrahlung, the power per frequency per unit volume is given by integration of equation (2.63) over the electron energy;

$$\begin{aligned} h\nu\frac{dN_\gamma}{dtdh\nu dV} &= \int h\nu\frac{dN_\gamma}{dtdh\nu}N_{\rm e}dE \\ &\simeq 4Z_{\rm i}^2\alpha r_0^2 cK_e n_{\rm T}\left(\frac{4}{3(\mu-1)}-\frac{4}{3\mu}+\frac{1}{\mu+1}\right)\left(\frac{h\nu}{m_{\rm e}c^2}\right)^{-\mu+1}\left(\ln\left(\frac{4h\nu}{m_{\rm e}c^2}\right)-\frac{1}{2}\right). \end{aligned} \tag{2.67}$$

Hence the number spectrum of bremsstrahlung photons traces that of the parent electrons. Power per unit volume is given by

$$\begin{aligned} \frac{dE_\gamma}{dtdV} &= \int_{h\nu_{\rm min}}^{h\nu_{\rm max}} h\nu\frac{dN_\gamma}{dtdh\nu dV}dh\nu \\ &= 4\alpha r_0^2 cK_e n_{\rm T}\left(\frac{4}{3(\mu-1)}-\frac{4}{3\mu}+\frac{1}{\mu+1}\right)\times \\ &\quad\begin{cases} \left[\ln\left(\frac{h\nu}{m_{\rm e}c^2}\right)\left\{\frac{1}{2}\ln\left(\frac{h\nu}{m_{\rm e}c^2}\right)+\ln 4-\frac{1}{2}\right\}\right]\Big|_{h\nu_{\rm min}}^{h\nu_{\rm max}}, & \text{for } \mu=2 \\ \left[\frac{1}{2-\mu}\left(\frac{h\nu}{m_{\rm e}c^2}\right)^{-\mu+2}\left\{\ln\left(\frac{4h\nu}{m_{\rm e}c^2}\right)-\frac{1}{2}\right\}+\frac{1}{\mu-1}\left(\frac{h\nu}{m_{\rm e}c^2}\right)^{-\mu+1}\right]\Big|_{h\nu_{\rm min}}^{h\nu_{\rm max}}, & \text{for } \mu\neq 2. \end{cases} \end{aligned} \tag{2.68}$$

2.4.5 π^0-decay

Cosmic-ray protons produce neutral pions (π^0) through inelastic collisions with interstellar protons. In the rest frame of the interstellar protons, a threshold total energy of cosmic-ray protons to produce π^0 is given by $m_{\rm p}c^2(1+2m_\pi/m_{\rm p}+m_\pi^2/2m_{\rm p}^2)\sim 1.2$ GeV, which is

determined by conservation of four-momentum, where $m_\pi = 135$ MeV is the mass of π^0. Above the threshold energy, the cross section of the inelastic proton-proton collision, $\sigma_{\rm inel}$, is about 10^{-26} cm^{-2}, varing little with the energy of protons (Dermer 1986 [52]). Ninety-nine percent of π^0 decay into two photons. Almost of the other one percent of π^0 decay into a set of electron, positron and photon, but we neglect these products.

In order to treat π^0-decay photons analytically, we adopt δ-function approximation of Aharonian and Atoyan (2000) [11]. The cross section $\sigma_{\rm inel}$ is approximated by

$$\sigma_{\rm inel}(E_{\rm p}) \simeq 3\left[0.95 + 0.06\ln\left(\frac{E_{\rm p} - m_{\rm p}c^2}{1\ {\rm GeV}}\right)\right] \times 10^{-26}\ {\rm cm}^2, \tag{2.69}$$

where $E_{\rm p} = \gamma m_{\rm p} c^2$ is the total energy of cosmic-ray protons. A mean fraction, f_π, of the kinetic energy of a proton transferred to a π^0 per collision is 0.17. Hence a time-scale of cooling of cosmic-ray protons by π^0 production is given by

$$t_\pi \sim \frac{1}{f_\pi \sigma_{\rm inel} n_{\rm T} c} \sim 10^7 \left(\frac{n_{\rm T}}{1\ {\rm cm}^{-3}}\right)^{-1}\ {\rm yr}, \tag{2.70}$$

which is longer than time-scale of middle-aged SNRs of 10^4 yr unless $n_{\rm T} \geq 10^3$ cm^{-3}. Assuming that a fraction of kinetic energy of protons transferred to π^0 is always f_π, a spectrum of π^0 emitted from protons whose energy distribution function is $N_{\rm p}$ is given by,

$$\begin{aligned}\frac{dN_\pi}{dtdE_\pi dV} &= \int c n_{\rm T} \sigma_{\rm inel}(E_{\rm p}) N_{\rm p}(E_{\rm p}) \delta(E_\pi - f_\pi(E_{\rm p} - m_{\rm p}c^2)) dE_{\rm p} \\ &= \frac{c n_{\rm T}}{f_\pi} \sigma_{\rm inel}\left(m_{\rm p}c^2 + \frac{E_\pi}{f_\pi}\right) N_{\rm p}\left(m_{\rm p}c^2 + \frac{E_\pi}{f_\pi}\right),\end{aligned} \tag{2.71}$$

where $E_\pi = \gamma_\pi m_\pi c^2$. Because a time-scale of decay of π^0 is much small as 8.5×10^{-17} s, we can assume that π^0 decay at the same time as they are produced. In the rest frame of π^0, emitted photons have an energy of $m_\pi c^2/2$ and an isotropic distribution. The Lorentz transform of the isotropic distribution gives that the number distribution of photons produced by decay of π^0 with the number of N_π and a given momentum of p_π in the observer frame is

$$\frac{dN_\gamma}{dh\nu} = \begin{cases} \dfrac{2N_\pi}{p_\pi c}, & \dfrac{(E_\pi - p_\pi c)}{2} < h\nu < \dfrac{(E_\pi + p_\pi c)}{2} \\ 0, & \text{otherwise.} \end{cases} \tag{2.72}$$

Using equations (2.71) and (2.72), the photon number spectrum is given by

$$\begin{aligned}\frac{dN_\gamma}{dtdh\nu dV} &= 2\int_{E_{\rm min}}^\infty \frac{1}{p_\pi}\frac{dN_\pi}{dtdE_\pi dV} dE_\pi \\ &= \frac{2cn_{\rm T}}{f_\pi}\int_{E_{\rm min}}^\infty \frac{1}{p_\pi}\sigma_{\rm inel}\left(m_{\rm p}c^2 + \frac{E_\pi}{f_\pi}\right) N_{\rm p}\left(m_{\rm p}c^2 + \frac{E_\pi}{f_\pi}\right) dE_\pi\end{aligned} \tag{2.73}$$

where $E_{\rm min} = h\nu + m_\pi^2 c^4/(4h\nu)$ is the minimum pion energy to produce a photon of energy of $h\nu$. Figure 2.7 shows that π^0 and photon number spectrum when the proton spectrum is

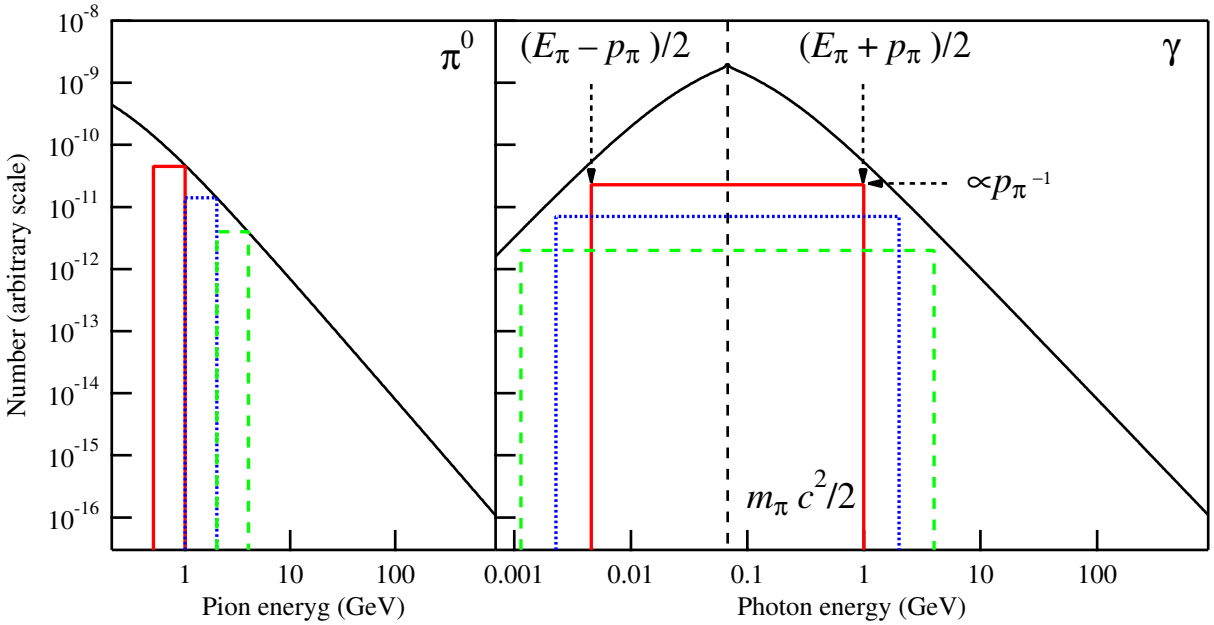

Figure 2.7: Number spectra of π^0 (left) and γ-ray produced by decay thereof (right). Red, blue, and green solid lines in right panel represent the spectra of photons emitted by decay of π^0 whose distributions are represented by the same color solid lines in left panel.

proportional to E^{-2}. The photon number spectrum peaks at $m_\pi c^2/2$ and have a symmetric structure in log-log representation on either side.

When $N_{\rm p} \propto E_{\rm p}^{-\mu}$, number spectrum of emitted photons is roughly proportional to $(h\nu)^{-\mu}$ above an energy of $m_\pi c^2/2$. Below the energy, the photon spectrum rises. This bump-like structure in photon spectrum, as shown in figure 2.7, does not appear in bremsstrahlung or inverse-Compton photon spectra, and can be used to distinguish π^0-decay spectrum from others. In fact, such structure have been observed in two MM SNRs W44 and IC 443 (Giuliani et al. 2011 [77]; Ackermann et al. 2013 [9]), and a shell-like SNR Cas A (Yuan et al. 2013 [206]).

Figure 2.8 shows time-scales of energy loss due to non-thermal radiation and energy gain due to acceleration, calculated for $n_{\rm T} = 1$ cm^{-3}, $B = 100\mu$G, and $V_{\rm s} = 3000$ km s^{-1}. The energy loss of protons due to π^0 production is negligible compared to the energy gain due to acceleration, unless $n_{\rm T} \gtrsim 10^5$ cm^{-3} $(E/10^6$ GeV$)^{-1}(B/100$ μG$)(V_{\rm s}/3000$ km s$^{-1})^2$. The energy loss of electron is dominated by synchrotron radiation. The synchrotron loss rate becomes higher than the energy gain rate due to acceleration above an energy of $E \sim$ 37 TeV $(B/100$ μG$)^{-1/2}(V_{\rm s}/3000$ km s$^{-1})$.

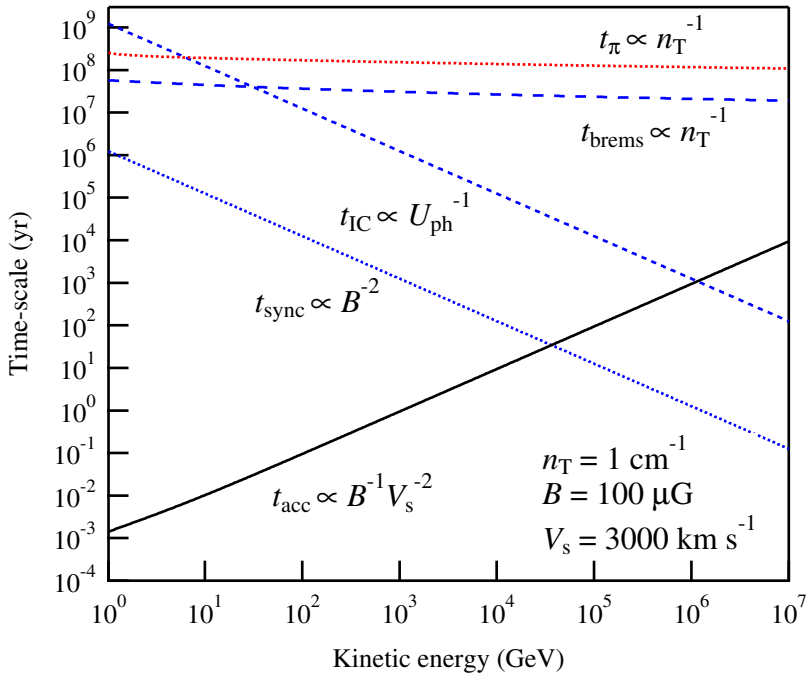

Figure 2.8: Time-scales of energy loss of electrons due to synchrotron radiation (blue dotted line), inverse-Compton scattering off the cosmic microwave background photons (blue dashed line), and bremsstrahlung (blue broken line), and of protons due to π^0-decay (red dotted line). The time-scale of energy gain due to acceleration is also shown by black solid line.

Chapter 3

Observed Propertied of Shell-Like and Mixed-Morphology Supernova Remnants

Shell-like SNRs and MM SNRs are classified by morphology in radio and X-ray bands. The morphology and also spectra in these bands of shell-like SNRs are explained by a picture described in chapter 2.

The radio of shell-like SNRs are explained by synchrotron radiation emitted from electrons accelerated by the blast wave through DSA. The diffusive shock acceleration predicts accelerated electrons of which energy spectrum is a power-law with a spectral index of 2 for a compression ratio of 4. Such electrons emit synchrotron radiation of which energy spectra is a power-law with spectral index of 0.5. This value of spectral index is comparable to a typical observational value of shell-like SNRs (see figure 1 of Reynolds et al. 2012 [149]). The synchrotron intensity is proportional to three-halves power of the magnetic field strength. Since a shell, where the magnetic field is strong because of compression, between the blast wave and reverse shock have a thickness that is at most 30% of a radius of the blast wave in free expansion phase (see figure 2.2b), the synchrotron radio appears to be shell-like morphology. In the Sedov-Taylor phase, since the magnetic field is strong near the blast wave but is weak far away from the blast wave front because of expansion, the radio appears to be shell-like morphology.

The X-ray morphology and spectra of shell-like SNRs are explained by shock compression and thermal evolution of shocked matter, respectively. In the free expansion phase, the thickness of the shell of shocked matter, which emit X-rays, is at most 30% of the radius of blast wave. As a result, the X-rays appear to be shell-like morphology. In the Sedov-Taylor phase, the X-ray emission measure of shocked matter are high near the blast wave (see figure 2.3) and hence the X-ray morphology is shell-like. The X-ray spectra of shocked matter reflect Coulomb heating of electrons and ionizing of ions by electron collisions behind the shocks. Since the times-scale of ionizing is longer than that of the heating up to temperatures at which the X-rays are emitted, the shocked matter is under-ionized/ionizing states. In fact, observed X-ray spectra of shell-like SNRs are explained by such non-equilibrium plasma

model.

As well as shell-like SNRs, the radio morphology of MM SNRs is commonly shell-like. We show a list of Galactic MM SNRs, which can be spatially resolved in the radio and X-ray bands, with their angular diameters, θ, radio spectral indices, 1 GHz radio fluxes, $F_{1\ \mathrm{GHz}}$, distances, d, and diameters, D in table 3.1. Our definition of MM SNRs basically follows Vink (2012) [191] (table 4 in his paper). The radio spectral index of MM SNRs is 0.50, which can be explained by DSA, in average.

On contrast to shell-like SNRs, the X-ray morphology of MM SNRs is not shell-like but irregular shape in the radio shell. Such morphology can not be explained by the free expansion or Sedov-Taylor model. In addition to the X-ray morphology, ionization states of X-ray emitting matter of MM SNRs are different from those of shell-like SNRs. Kawasaki et al. (2002) [104] found an over-ionized/recombining plasma ($T_{\mathrm{z}} > T_{\mathrm{e}}$) in *ASCA* observation from a MM SNR IC 443. Such plasma state does not caused by the shock heating and ionizing that explain the X-rays of shell-like SNRs. Moreover, Kawasaki et al. (2005) [105] investigated five other MM SNRs (W49B, W28, W44, 3C391, and Kes 27), and found that W49B shows over-ionized states as well. They proposed that thermal conduction from the hot interior of the remnant to the cold exterior can explain the over-ionized plasma and center-filled X-rays. The over-ionized states of IC 443 and W49B are shown by observations of radiative recombination continua in X-ray spectra by *Suzaku* (Yamaguchi et al. 2009 [202], Ozawa et al. 2009 [136]). Yamaguchi et al. 2009 [202] discussed that thermal conduction is unfavorable for the origin of over-ionized state of IC 443 using the plasma density and electron temperature updated by *Suzaku* observation. The recombination radiation X-rays are detected also from other four MM SNRs, G359.1-0.5 (Ohnishi et al. 2011 [134]), W44 (Uchida et al. 2012 [184]), W28 (Sawada and Koyama 2012 [163]), G346.6-0.2 (Yamauchi et al. 2013a [204]), and a SNR G348.5+0.1 (Yamauchi et al. 2013b [205]), which is possibly a MM SNR. In the above papers about the detection of recombination radiation X-rays, the origin of over-ionized states are discussed, but are still not clear.

Many of MM SNRs that emit the radiative recombination X-rays are associated with star forming complex including molecular clouds and H II regions. In fact, interactions with molecular clouds are suggested by OH maser and near infrared observations. Since the associations suggest that progenitors of the MM SNRs are core-collapse SNe of massive stars, the over-ionized state may related to the progenitors and/or their environments. In addition, many of the MM SNRs are observed in γ-ray band. The observations of γ-rays may be due to enhancement of π^0-decay by the interactions with molecular clouds. We show the list of detections of radiative recombination X-rays, observations of γ-rays, and sign of interactions with molecular clouds in table 3.2.

There are two possibilities of over-ionized states. One is photo-ionization by X-ray photons, and the other is rarefaction caused when a blast wave breaks out of dense CSM into ISM (Itoh and Masai 1989 [95]).

The low energy X-ray photons can ionize ion but do not heat electrons. Hence, an external X-ray source near a SNR can increase an ionization temperature of X-ray emitting plasma of the SNR higher than an electron temperature. However, such sources are not observed. Other possibility is ionizations by photons emitted at the supernova shock break-out, but

Table 3.1: List of Galactic MM SNRs

Name	Other Name	θ	$F_{1\ \mathrm{GHz}}$	Index	Refs.	d	Refs.	D
		arcmin	Jy			kpc		pc
G0.0+0.0	Sgr A East	3.5×2.5	100?	0.76	[57]	8	[160]	8.2×5.8
G6.4-0.1	W28	48	310	0.35	[54]	1.9	[190]	27
G8.7-0.1[a]	W30	45	80	0.53	[98]	4.5	[61]	59
G31.9+0.0	3C391	7×5	24	0.49	[38]	7.2	[65]	15×11
G33.6+0.1	Kes 79	10	22	0.58	[73]	7.1	[40]	21
G34.7-0.4	W44	35×27	230	0.37	[41]	3.1	[195]	32×24
G41.1-0.3	3C397	4.5×2.5	22	0.48	[82]	10	[159]	13×7.3
G43.3+0.2	W49B	4×3	38	0.48	[80]	8	[128]	9.3×7
G49.2-0.7	W51C	30	160?	0.26	[129]	5.6	[109]	49
G53.6-2.2	3C400.2	33×28	8	0.50	[175]	2.3	[72]	22×19
G65.3+5.7	G65.2+5.7	310×240	52?	0.58	[199]	0.8	[37]	72×56
G82.2+5.3	W63	95×65	120?	0.44	[71]	1.6[e]	[155]	44×30
G89.0+4.7	HB21	120×90	220	0.38	[143]	0.8	[179]	28×21
G93.7-0.2	CTB 104A	80	65	0.52	[71]	1.5	[188]	35
G116.9+0.2	CTB1	34	8	0.57	[175]	3.1	[83]	31
G132.7+1.3	HB3	80	45	0.66	[111]	2.2	[156]	51
G156.2+5.7		110	5	0.48	[200]	3	[142]	96
G160.9+2.6	HB9	140×120	110	0.59	[71]	0.8	[117]	32×28
G166.0+4.3	VRO 42.05.01	55×35	7	0.33	[71]	4.5	[114]	72×46
G189.1+3.0	IC443	45	160	0.39	[42]	1.5	[193]	20
G272.2-3.2		15?	0.4	0.55	[56]	2	[85]	8.7
G290.1-0.8	MSH 11-61A	19×14	42	0.43	[125]	7	[152]	39×29
G327.4+0.4	Kes 27	21	30?	0.6	[125]	4.3	[122]	26
G344.7-0.1[b]		10	2.5	0.6	[53]	14	[203]	41
G346.6-0.2[c]		8	8?	0.5	[53]	8	[204]	19
G352.7-0.1[d]		8×6	4	0.6	[53]	7.5	[73]	17×13
G359.1-0.5		24	14	0.37	[147]	8[f]	[148]	56

Note. This list basically follows table 4 of Vink (2012) [191]. We exclude G357.1-0.1 (Tornado), which is listed in the table 4 of Vink (2012), from a member of MM SNRs because X-ray observation (Sawada et al. 2011 [164]) suggests that this object is a bipolar jet from an accreting binary active in the past. The radio angular diameter, θ, and the radio flux at 1 GHz, $F_{1\ \mathrm{GHz}}$, are taken from Green (2009) [82].

[a] Following the suggestion of Hewitt and Yusef-Zadeh (2009) [88].

[b] Proposed as a MM SNR by Giacani et al. (2011) [74].

[c] This SNR exhibits thermal X-ray center-filled morphology (Yamauchi et al. 2013a [204]). We categorized this SNR into MM SNRs.

[d] Proposed as a MM SNR by Giacani et al. (2009) [73].

[e] Adopted the mean of a minimum value of 1.3 kpc and maximum value of 1.9 kpc in the reference.

[f] Observations of radio (Uchida et al. 1992 [185]) and X-ray (Bamba et al. 2002 [23]) suggest that this SNR is likely located near the Galactic center. We adopt a distance of 8 kpc to the Galactic center (Reid 1993 [148]).

Table 3.2: Detection of recombination radiation X-rays, GeV/TeV γ-rays, and signs of interactions with molecular clouds of MM SNRs

Name	RR	GeV	TeV	OH[a]	CO[a]	IR[a]
G0.0+0.0 (Sgr A East)				Y		
G6.4-0.1 (W28)	Y[163]	Y[2]	Y[14]	Y	Y	Y
G8.7-0.1 (W30)		Y[16]		Y		
G31.9+0.0 (3C391)		Y[43]		Y		Y
G33.6+0.1 (Kes 79)					Y	
G34.7-0.4 (W44)	Y[184]	Y[9]		Y	Y	Y
G41.1-0.3 (3C397)					Y	
G43.3+0.2 (W49B)	Y[136]	Y[3]	Y[39]			Y
G49.2-0.7 (W51C)		Y[1]	Y[17]	Y	Y	
G53.6-2.2 (3C400.2)						
G65.3+5.7 (G65.2+5.7)						
G82.2+5.3 (W63)						
G89.0+4.7 (HB21)		Y[143]		Y	Y	Y
G93.7-0.2 (CTB 104A)						
G116.9+0.2 (CTB1)						
G132.7+1.3 (HB3)					Y	
G156.2+5.7						
G160.9+2.6 (HB9)					Y	
G166.0+4.3 (VRO 42.05.01)		Y?[19]			Y	
G189.1+3.0 (IC443)	Y[202]	Y[9]	Y[5]	Y	Y	Y
G272.2-3.2						
G290.1-0.8 (MSH 11-61A)					Y	
G327.4+0.4 (Kes 27)						
G344.7-0.1						Y
G346.6-0.2	Y[204]			Y		Y
G352.7-0.1						
G359.1-0.5	Y[134]	Y?[91]	Y?[15]	Y	Y	Y

The character "RR" represents radiative recombination X-rays. The characters "OH", "CO", and "IR" represent 1720 MHz OH maser, CO line emission, and infrared emission, respectively. The character "Y" means that the radiations or the sign of interaction are detected. The character "Y?" means that γ-rays whose origin may be a SNR are detected.

[a] Follow Jiang et al. 2010 [96].

such photons can not ionize irons up to highly ionized states as observed in W49B. Therefore, the photo-ionization is unlikely to be the common origin of over-ionized states of MM SNRs.

The other possibility is the rarefaction (Itoh and Masai 1989 [95]). If a progenitor of a SNR is a massive star, it is surrounded by dense CSM composed of stellar wind matter blown out in the pre-supernova phase. After the explosion, ejecta initially interact with the CSM. The ejecta and CSM are heated by the reverse shock and blast wave, respectively. These heated matter are nearly ionization equilibrium state ($T_{\rm z} \sim T_{\rm e}$) because of high density. After the blast wave breaks out of the CSM into ISM, rarefaction of the shock matter occurs. Because of the rarefaction, the shocked matter rapidly cool by adiabatic expansion to be over-ionized states. The rarefaction also extends a time-scale of recombination because of the decrease in the density of shocked matter. Hence, the over-ionized state continues for long periods. Since observations suggest that the progenitors of MM SNRs are massive stars, as mentioned above, this scenario is likely for the origin of over-ionized states of MM SNRs.

In addition to the ionization states of X-ray emitting matter, the X-ray flux of MM SNRs is different from that of shell-like SNRs. We show the flux ratio of 2.1–10 keV thermal X-rays to 1 GHz radio against the 1 GHz surface brightness, $\Sigma_{1\ \rm GHz}$, for Galactic MM and shell-like SNRs in figure 3.1. Our definition of shell-like SNRs follows "type S" in Green (2009) [82] except those defined as MM SNRs above. We take the flux ratio in order to eliminate the distance dependence of the flux. Since the radio properties of MM and shell-like SNRs are not very different from each other, the ratio is expected to reflect the difference in X-ray properties. We use $\Sigma_{1\ \rm GHz}$ to compare SNRs at the same evolutional stage because $\Sigma_{1\ \rm GHz}$ correlates with the diameter (e.g., Case and Bhattacharya 1998 [40]) and thought to reflect their stages. The flux in the 2.1–10 keV band and that the 1 GHz are taken from Chandra supernova remnant catalog[1] and Green (2009) [82], respectively. As for MM SNRs, W28 and W44, Chandra observes only their central regions. However, because X-rays of MM SNRs come substantially from their central regions, we use the data of Chandra. We calculate $\Sigma_{1\ \rm GHz}$ using the 1 GHz flux and $\theta_{\rm radio}$. For a value of $\Sigma_{1\ \rm GHz}$, the flux ratios of MM SNRs are systematically lower than those of shell-like SNRs. An exception, a black diamond in the most left-top in figure 3.1 (a), is MM SNR G272.2–3.2. In order to make clear the difference between MM and shell-like SNRs, we introduce the product, P, of the X-ray/radio flux ratio by $\Sigma_{1\ \rm GHz}$, and show a distribution of P in figure 3.1 (b). Such product is though to be proportional to the X-ray surface brightness, because $P \propto (F_{\rm X}/F_{\rm radio}) \times (F_{\rm radio}/\theta^2_{\rm radio}) = F_{\rm X}/\theta^2_{\rm radio}$, where $F_{\rm X}$ and $F_{\rm radio}$ are the X-ray and radio flux, respectively. One can see that the products of MM SNRs are lower than those of shell-like SNRs by an order of magnitude. The lower X-ray flux as shown in figure 3.1 can be explained by the rarefaction scenario, because X-ray emissivity of plasma with recombining state that predicted in the scenario after the break out is lower than that of under-ionized plasma.

The over-ionized states and low X-ray flux of MM SNRs support the rarefaction scenario. The rarefaction scenario may accounts for other observed properties of MM SNRs in addition to these two properties. Therefore we investigate evolution of remnants of supernova exploded in the CSM in the next chapter.

[1]The data is available at http://heawww.harvard.edu/ChandraSNR/snrcat_gal.html

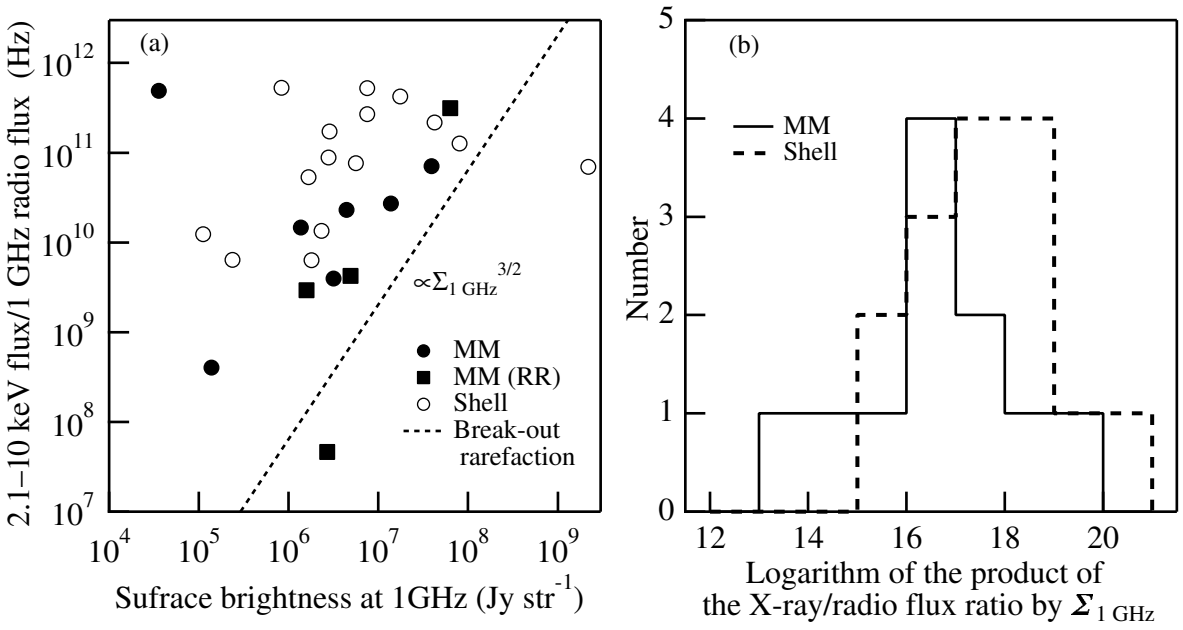

Figure 3.1: (a) Flux ratio of 2.1–10 keV X-rays to 1 GHz radio vs. the 1 GHz surface brightness for shell-like (open diamonds) and MM SNRs (filled diamonds and squares). The character "RR" represents that radiative recombination X-rays are detected. The dotted line represents the dependence of the X-ray/radio flux ratio on $\Sigma_{1\ \mathrm{GHz}}$ in the rarefaction scenario (see chapter 5). (b) Histogram of the product of the X-ray/radio flux ratio by $\Sigma_{1\ \mathrm{GHz}}$ of shell-like (broken line) and MM SNRs (solid line).

Chapter 4

Evolution of Supernova Remnants Expanding into Dense Cirucmstellar Matter and Interstellar Medium Outside

We investigate evolution of SNRs expanding into the CSM and the ISM outside to cause the rarefaction that results in over-ionized states as a possible formation process of MM SNRs. A previous research on such evolution was done only by Itoh and Masai (1989) [95]. They carried out spherically-symetrical numerical hydrodynamical calculation with ionization and radiation and treat the electron and ion temperatures separately. However, one of the observation properties of MM SNRs is irregular, i.e., non-symmetrical, X-ray morphology. Hence, we extend the research to three-dimensional numerical hydrodynamical calculations, considering an realistic anisotropy of the CSM. On the other hand, we do not solve ionization and radiation with the hydrodynamical calculations and treat only the mean temperature in the calculations in order to cut computational costs. An effect of neglecting ionization and radiation on dynamical evolution is about 5% in a time-scale, as mentioned in section 4.2.1. The ionization state and electron temperature calculate using results of the hydrodynamical calculations and assuming Coulomb interactions (see section 2.3). Although ages of MM SNRs are of the order of $10^3 - 10^4$ yr, Itoh and Masai (1989) [95] calculated evolution of the SNR up to 10^3 yr. We calculate evolution up to 10^4 yr.

In the following, we describe initial conditions of the numerical hydrodynamical calculations in section 4.1 and results in section 4.2. Using the results of calculations, we investigate non-thermal particles and radio and γ-rays, which are observed from many of MM SNRs emitting recombination radiation X-rays (see chapter 4), emitted from blast-shocked shell after the break-out, and describe in section 4.3.

4.1 Dynamical Evolution: Model

4.1.1 Circumstellar Matter

In a core-collapse SN, the massive progenitor (red or blue supergiant or Wolf-Rayet star or luminous blue variable) is expected to blow a strong stellar wind in its pre-SN phase, and to form dense CSM around the progenitor. If the stellar wind is spherically symmetric with a constant mass-loss rate, $\dot{M}$, and wind velocity, v_w , the CSM density, ρ, at a distance r from the progenitor is given by

$$\rho = \frac{\dot{M}}{4\pi r^2 v_{\rm w}}. \tag{4.1}$$

For a while before the SN explosion, the stellar wind ceases. Then, the stellar wind forms a thick shell. The inner and outer radii of the shell are given by $R_{\rm in} = v_{\rm w} t_{\rm e}$ and $R_{\rm out} = v_{\rm w}(t_{\rm w} + t_{\rm e})$, respectively, where time $t_{\rm w}$ and $t_{\rm e}$ are the duration of the wind activity and the elapsed time after the wind ceases, respectively.

In realistic stellar winds, more matter around the equatorial plane than the polar direction may be accumulated, because of rotation of the progenitor. For instance, such anisotropy are observed around B[e] stars, which are extreme cases because their rotational velocities are near break-up velocities (e.g., Maeder & Meynet 2000 [118]). The anisotropy are also suggested by observations of type IIn SN of X-rays originated from interactions between the ejecta and CSM: a disk-like strucutre of CSM are suggested (Katsuda et al. 2013 [100]). We thus modify the above equation as follows:

$$\rho = \frac{\dot{M}}{4\pi v_{\rm w}} \frac{a}{x^2 + y^2 + a^2 z^2} \quad \text{for } R_{\rm in} \le (x^2 + y^2 + a^2 z^2)^{1/2} \le R_{\rm out}, \tag{4.2}$$

with an anisotropy parameter, a, which is the ratio of the major to minor axis of an equi-density surface of the wind matter. Hereafter, $R_{\rm in}$ and $R_{\rm out}$ are referred to the radii on the equatorial plane. This distribution gives an a^2 times higher density on the equatorial plane than in the polar direction at the same distance. For the progenitor of SN 1987A, Blondin and Lundqvist (1993) [34] suggested that the ratio of the equatorial to polar mass-loss rate was at least 20 during its red supergiant stage. This value corresponds to $a \simeq 4.5$. In our calculations we adopted values of from 1 to 3. Outside the CSM, we assume ISM.

We calculated the evolution for the following five models:

A1 Isotropic CSM same as Itoh and Masai (1989) for a reference.

A2 Anisotropic CSM concentrated around the equatorial plane.

A3 Same as A2, but more mass around the equatorial plane.

B1 Same as A2, but with a lower density ISM.

B2 Same as B1, but with a higher wind velocity.

The numerical values for each model are given in table 1, where the values of $R_{\rm in}$, $R_{\rm out}$, $\rho_{\rm in}$, and $\rho_{\rm out}$ are those on the equatorial plane. The mass-loss rate is assumed to be $5 \times 10^{-5} M_\odot$ yr^{-1}, the same as that of Itoh and Masai (1989), for all the models.

Table 4.1: Parameters of circumstellar matter and interstellar medium.*

Model	CSM						ISM
	a	$R_{\rm in}$ (10^{16} cm)	$R_{\rm out}$ (10^{16} cm)	$\rho_{\rm in}$ (amu cm^{-3})	$\rho_{\rm out}$ (amu cm^{-3})	$v_{\rm w}$ (cm s^{-1})	$\rho_{\rm ISM}$ (amu cm^{-3})
A1	1	2.0	92.6	3.4×10^{5}	1.6×10^{2}	10^{6}	1.6×10^{-1}
A2	2	2.0	92.6	6.9×10^{5}	3.2×10^{2}	10^{6}	1.6×10^{-1}
A3	3	2.0	92.6	1.0×10^{6}	4.8×10^{2}	10^{6}	1.6×10^{-1}
B1	2	2.0	92.6	6.9×10^{5}	3.2×10^{2}	10^{6}	1.6×10^{-2}
B2	2	20	926	6.9×10^{2}	3.2×10^{-1}	10^{7}	1.6×10^{-2}

Mass loss rate $\dot{M}$ is $5\times10^{-5}M_{\odot}$ yr^{-1} in all the models, and $\rho_{\rm in}=\rho(r=R_{\rm in})$, $\rho_{\rm out}=\rho(r=R_{\rm out})$.

4.1.2 Supernova Ejecta

We focus on the effect of the CSM, particularly for an anisotropic CSM, on the early phase evolution of SNRs. For the SN ejecta, we simply assume a spherical distribution with a core of radius of $R_{\rm c}$ and an extended envelope of radius $R_{\rm ej}$, as (Truelove and McKee 1999 [183])

$$\rho=\frac{3M_{\rm ej}}{4\pi(v_{\rm ej}t)^3}\frac{1-n/3}{1-(n/3)w_{\rm c}^{3-n}}\times\begin{cases} w_{\rm c}^{-n} & \text{for } r<R_{\rm c} \\ [r/(v_{\rm ej}t)]^{-n} & \text{for } R_{\rm c}\le r\le R_{\rm ej}, \end{cases} \tag{4.3}$$

where

$$v_{\rm ej}=\left(\frac{2E_{\rm ej}}{M_{\rm ej}}\right)^{1/2}\left(\frac{5-n}{3-n}\right)^{1/2}\left(\frac{w_{\rm c}^{-(3-n)}-n/3}{w_{\rm c}^{-(5-n)}-n/5}\right)^{1/2}\frac{1}{w_{\rm c}} \tag{4.4}$$

is the expansion velocity at $R_{\rm ej}$. $M_{\rm ej}$ and $E_{\rm ej}$ are the ejecta mass and the explosion energy (kinetic energy), respectively. These are assumed to be $E_{\rm ej}=2\times10^{51}$ erg and $M_{\rm ej}=10M_{\odot}$. The other parameters, n and $w_{\rm c}=R_{\rm c}/R_{\rm ej}$, are taken to be 6 and 0.49, respectively. All of these values are the same as those of Itoh and Masai (1989), and hence $v_{\rm ej}\simeq8.5\times10^{8}$ cm s^{-1}. We show initial distribution of model A1 in figure 4.1 for instance.

4.2 Dynamical Evolution: Calculations and Resutls

We numerically solve the Euler equations (equations 2.1, 2.2, and 2.3) utilizing the athena3d code (Stone et al. 2008 [174]). The ideal EOS of $P=(\gamma-1)\rho\epsilon$ with $\gamma=5/3$ is considered. The mean molecular weight is taken to be 0.5.

In the hydrodynamical evolution, we obtained mean temperature T of ions (protons) and electrons weighted by their number density. If no plasma mode works directly on elections at the shock front, the ion temperature $T_{\rm i}$ rises faster and then the energy of ions is transferred to electron. We calculate $T_{\rm i}$ and $T_{\rm e}$ from T, assuming the transport by Coulomb collisions (see section 2.3).

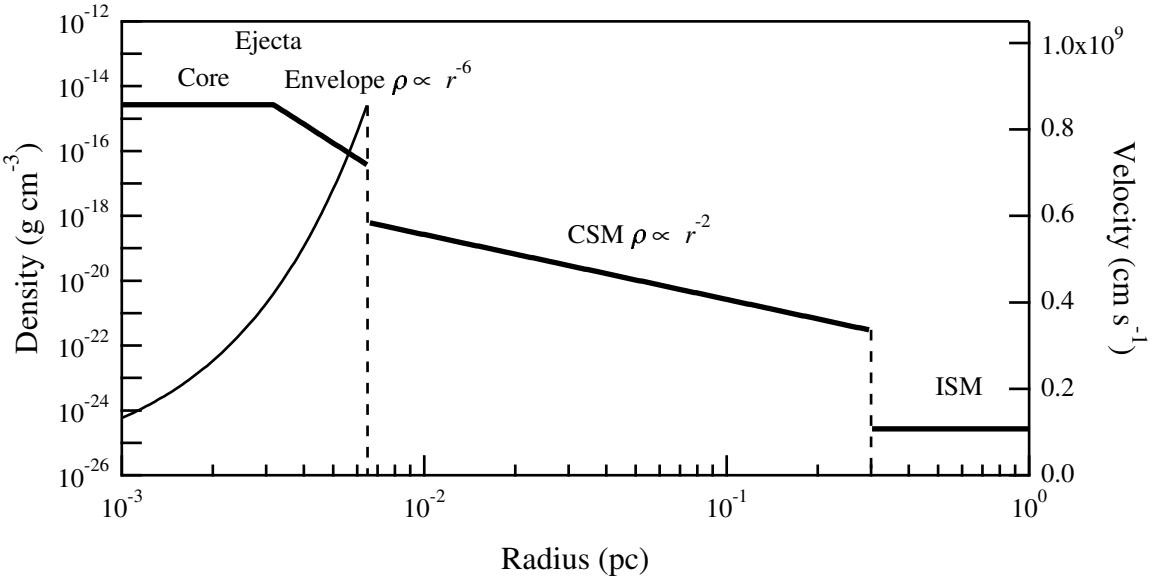

Figure 4.1: Initial distribution of density (thick line) and velocity (thin line) of model A1.

4.2.1 Model A1

Although we include neither ionization nor radiation and simply assume the adiabatic evolution, the evolution of model A1 is in fairly good agreement with Itoh and Masai (1989) [95]. The blast shock and reverse shock heat the CSM to $T \gtrsim 10^8$ K, and the ejecta to $T \gtrsim 10^7$ K, respectively. The blast wave expands as $r_{\rm b} \propto t^{0.88}$, while $r_{\rm b} \propto t^{0.87}$ in Itoh and Masai (1989) [95], where $r_{\rm b}$ is the blast-wave radius.

The blast wave breaks out at 41 yr, 2 years earlier than in Itoh and Masai (1989) [95] who take radiation loss into calculation. After the break-out, the blast wave rapidly expands adiabatically, and hence the temperature and density of the shocked matter decrease approximately as $T \propto t^{-2}$ and $\rho \propto t^{-3}$ for $\gamma = 5/3$.

When the pressure of the shocked CSM becomes below that of the shocked ISM, the second reverse shock occurs to propagate inward and reheats the CSM and ejecta. The second reverse shock reaches the ejecta at 830 yr, 120 years earlier than in Itoh and Masai (1989) [95].

4.2.2 Models A2 and A3

The evolution is basically the same as model A1, but is dependent on direction: more matter on the equatorial plane than in the polar direction. With increasing the value of a, the break-out occurs earlier in the polar and later in the equatorial direction than in model A1. The former is due to a shorter distance to the CSM, and the latter is higher density of the CSM than those in model A1. In addition, the second reverse shock reaches the ejecta earlier in the polar direction and later in the equatorial direction than in model A1. In model A2, the break-out occurs at 17 yr in the polar direction, and at 46 yr in the equatorial direction as

shown in Figure 4.2. The mean temperature T of the shocked ejecta turns to rise at 340 yr and 1100 yr, in the polar and equatorial directions, respectively.

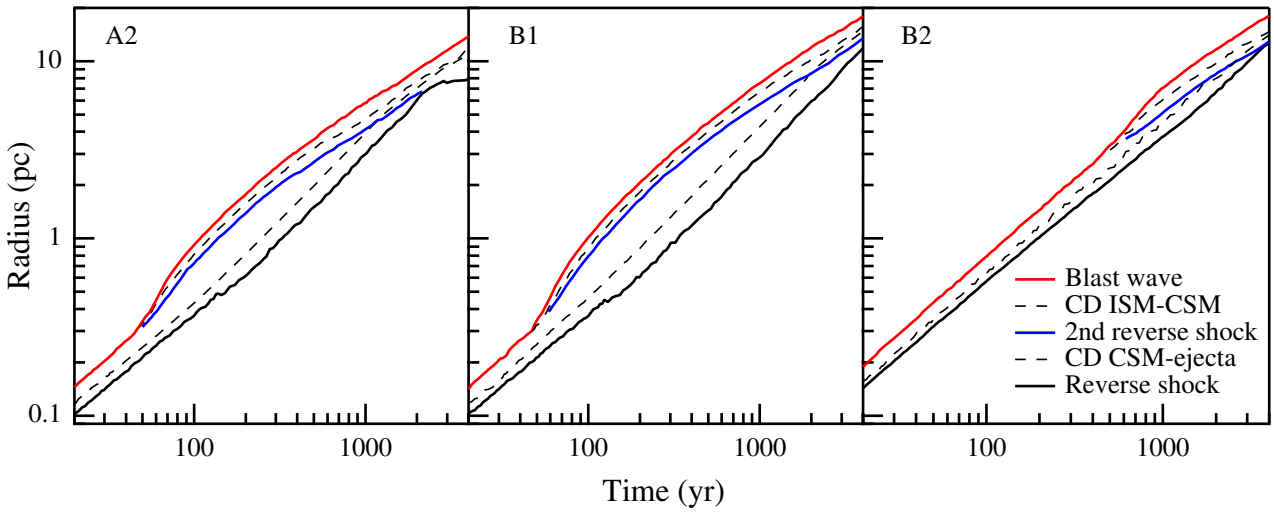

Figure 4.2: Shocks in the equatorial direction of model A2 (left), B1 (middle), and B2 (right) before and after the blast-wave break-out, as functions of the elapsed time after explosion. The upper, middle and lower solid lines represent the radii of the blast wave, second reverse shock and reverse shock, respectively. The upper and lower broken lines represent the contact discontinuities (CD) between ISM and CSM, and CSM and ejecta, respectively.

4.2.3 Model B1

The break-out occurs at the same time as model A2 since the CSM distribution is the same as model A2. The difference of model B1 from model A2 is the lower density of the ISM by an order of magnitude. The velocity of the blast wave after the break-out is slightly higher than that in model A2 by a factor of ~ 1.4 in the equatorial direction. As a result, the pressure of the shocked ISM is about one-fifth of that in model A2, and the second reverse shock occurs later. The temperature T of the shocked ejecta drops at 23 yr and 68 yr by the break-out, but turns to rise at 810 yr and 1800 yr in the polar and equatorial directions, respectively.

4.2.4 Model B2

The difference from model B1 is the lower density of the CSM by three orders of magnitude due to higher wind velocity by an order of magnitude. Even at such low densities, the break-out occurs at 170 yr and 450 yr in the polar and equatorial directions, respectively. Similarly to the other models, the temperature T of the shocked ejecta drops at 280 yr and 770 yr, but turns to rise by the second reverse shock at 920 yr and 2400 yr in the polar and equatorial directions, respectively.

4.3 Non-Thermal Particles and Radiation From Blast-Shocked Shell

In the present section, we consider model B2 for a model of MM SNR because this model explains the over-ionized states for the longest time of all the models concerned in the present thesis as described in chapter 5. Using the results of numerical hydrodynamic calculation of the model, we calculate synchrotron radio and inverse-Compton scattering, bremsstrahlung, and π^0-decay γ-ray emission from a blast-shocked ISM shell, assuming accelerated particles with a broken power-law spectra and magnetic field amplification by the particles.

4.3.1 Non-Thermal Particle Distribution

The diffusive shock acceleration results in a single power-law energy spectrum. On the other hand, γ-ray observations of SNRs by *Fermi* suggest that the energy spectrum of γ-ray emitting particles is not simply a single power-law, but a broken power-laws with an break energy, at which the spectrum becomes steep, in $\sim$GeV band. In order to take a realistic energy spectrum of particles into calculation, we assume a broken power-law spectrum:

$$N(E) = \begin{cases} KE^{-\mu}, & \text{for } E < E_{\rm b}, \\ KE_{\rm b}^{-\mu+\mu_2}E^{-\mu_2}, & \text{for } E_{\rm b} \leq E \leq E_{\rm max}, \end{cases} \tag{4.5}$$

where

$$K = \xi\langle n\rangle(\mu-1)(E_{\rm inj}^2 + 2mc^2E_{\rm inj})^{(\mu-1)}, \tag{4.6}$$

$E = (\gamma-1)mc^2$ is the kinetic energy, $E_{\rm b}$ is the break kinetic energy of 10 GeV, taken so as to make a GeV break in the γ-ray spectrum, $E_{\rm inj}$ the injection kinetic energy, ξ is the ratio of the number of non-thermal to thermal particles, and $\langle n\rangle$ is the average density of the blast-shocked shell. The spectral indecies are assumed to be $\mu = 2$ and $\mu_2 = 2.3$ which is medium value of the spectral index of cosmic-ray sources (e.g., Putze et al. 2011 [144]).

For $E_{\rm inj}$ and ξ, we consider that particles in the high energy tail of the thermal distribution are injected into acceleration process, as

$$E_{\rm inj-p,e} = \lambda_{\rm p,e}kT_{\rm p,e}. \tag{4.7}$$

with a constant λ, where the characters "p" and "e" mean proton and electron, respectively. Then a relation between ξ and λ is given by

$$\begin{aligned} \xi_{\rm p,e} &\equiv \frac{\int_{E_{\rm inj-p,e}}^{\infty} f_{\rm p,e}(E)dE}{\int_0^{\infty} f_{\rm p,e}(E)dE} \\ &= 1 - {\rm erf}({\lambda_{\rm p,e}}^{1/2}) + \frac{2}{\pi^{1/2}}{\lambda_{\rm p,e}}^{1/2}e^{-\lambda_{\rm p,e}}, \end{aligned} \tag{4.8}$$

where $f(E)$ is the Maxwellian distribution function, and erf is the error function.

We determine $\xi_{\rm p}$ for the pressure of accelerated protons to be equal to 10% of the ram pressure of ISM enters in the blast wave. The pressure of accelerated particles is given by

$$P_{\rm CR} = \frac{1}{3}\int_{p_{\rm inj}}^{p_{\rm max}} N'(p) p v dp \simeq \frac{1}{3}\xi\langle n\rangle c p_{\rm inj}\left[\ln\left(\frac{2p_{\rm b}}{mc}\right) + \frac{1}{\mu_2 - 2}\left(\frac{p_{\rm b}c}{E_{\rm b}}\right)^{-\mu_2+2}\right] \tag{4.9}$$

where we use $\mu = 2$ in the last expression. Here, v is the particle velocity, p is the momentum of a particle, $p_{\rm inj} = (2mE_{\rm inj})^{1/2}$ is the injection momentum, $p_{\rm max} = E_{\rm max}/c$ is the maximum momentum, $p_{\rm b}$ is the break momentum, and $N'(p)dp = N(E)dE$. In the last expression in equation (4.9), $p_{\rm inj} \ll mc$ and $p_{\rm max} \gg p_{\rm b} > mc$ are considered. The injection efficiency of protons is roughly proportional to the blast-wave velocity $V_{\rm s}$ because $\xi_{\rm p} \propto V_{\rm s}^2/p_{\rm inj-p} \propto V_{\rm s}^2/T_{\rm p}^{1/2} \propto V_{\rm s}$. The injection efficiency of protons reaches the maximum $\sim 2\times10^{-4}$ at ~ 530 yr, and then decreases to 5×10^{-5} at ~ 10000 yr. We determine $\xi_{\rm e}$ for the pressure $P_{\rm CR-e}$ of accelerated electrons not to exceed the pressure $P_{\rm CR-p}$ of accelerated protons. The ratio of the pressure of accelerated electrons to protons is

$$\frac{P_{\rm CR-e}}{P_{\rm CR-p}} \simeq 0.05\frac{\xi_{\rm e}}{\xi_{\rm p}}\left(\frac{E_{\rm inj-e}}{E_{\rm inj-p}}\right)^{1/2}. \tag{4.10}$$

If the injection energy of electrons is the same as protons, $\xi_{\rm e} \lesssim 20\,\xi_{\rm p}$ follows. In the following, we express $\xi_{\rm e}$ in unit of $\xi_{\rm p}$.

The maximum energy $E_{\rm max}$ is determined by the time-scales of energy gain and loss. Adiabatic loss due to SNR expansion is negligible through the age concerned here. The dominant loss process is synchrotron radiation and inverse-Compton scattering for electrons. Assuming that 1) mean free path of a particle is its gyration radius (Bohm limit), 2) shock compression ratio is 4, and 3) accelerated particles are relativistic ($\gamma \gg 1$), we estimate the time-scales of acceleration and radiation loss as

$$t_{\rm acc} \simeq \frac{32\gamma mc^3}{3eBV_{\rm s}^2} \tag{4.11}$$

and

$$t_{\rm loss(electron)} \simeq \frac{6\pi m_{\rm e}c}{\gamma\sigma_{\rm T}(B^2 + 8\pi U_{\rm CMB})}, \tag{4.12}$$

respectively, where $\sigma_{\rm T}$ is the Thomson scattering cross section, e is the elementary electric charge, B is the strength of the magnetic field in the shock downstream, assumed to be 4 times the strength in the upstream, and $U_{\rm CMB}$ is the energy density of cosmic microwave background. In SNRs, the magnetic field strength can be stronger than the average interstellar value by magnetic amplification mechanisms, as suggested by X-ray variability of RX J1713.7-3946 ([186]). Using the equation (14) of Bell and Lucek (2001) [28], we calculate the field strength in the SNR evolution. The magnetic amplification may cause the non-linear feedback from accelerated particles to the shock structure. However, such feedback is small when the injection efficiency is lower than $\sim 10^{-4}$ (e.g., Ferrand et al. 2010 [60]), which is marginally attained after the blast-wave break-out concerned here.

In figure 4.3 we show the time evolution of $E_{\rm max}$ and B in the blast-shocked shell. For protons, $E_{\rm max}$ is determined by $t_{\rm acc} \sim t_{\rm age}$, and reaches $\sim$ 1300 TeV at $\sim$ 700 yr, while $\sim$ 800 TeV at $\sim$ 430 yr in the case without CSM. For electrons, $E_{\rm max}$ is determined by $t_{\rm acc} \sim t_{\rm loss(electron)}$, and its maximum is about 10 TeV at the moment of the break out. At $\sim$ 700 yr, just after the break-out, $E_{\rm max}$ takes its maximum/minimum for protons/electrons because of rapid increase of the shock velocity and the magnetic field. For the explosion energy of 2×10^{51} erg assumed, the total energy of accelerated protons is 1×10^{49} erg at $\sim$ 700 yr and 2×10^{50} erg at $\sim$ 10000 yr.

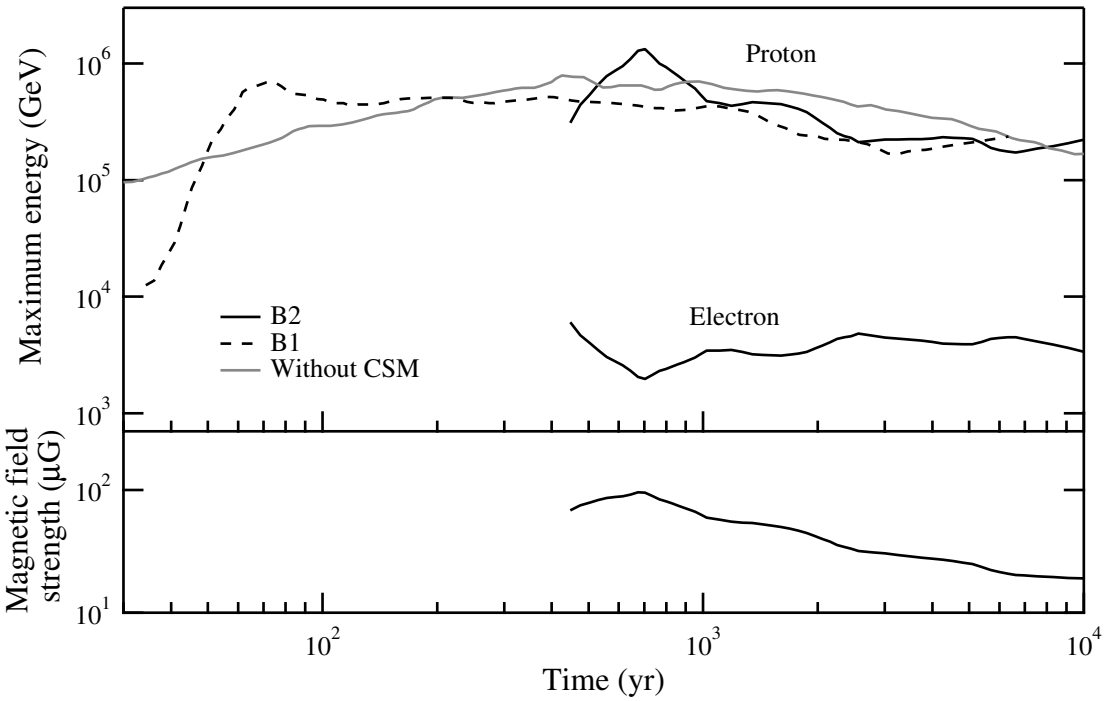

Figure 4.3: Maximum energy that the accelerated protons and electrons can reaches at a given time (upper) and the magnetic fields strength in the shock down stream (lower), as functions of elapsed time after the explosion. Gray line represents the maximum energy of the protons in the SNR evolution without CSM.

High energy particles can escape from the blast-shocked ISM shell by diffusion, because they have large mean free path. Taking an effect of the escape into consideration, we determine a spatial distribution of non-thermal particles in the shell with a condition that the particles are confined for shorter time of $t_{\rm age}$ or $t_{\rm esc} \sim R_{\rm b}^2/D$. Here, D is the diffusion coefficient, and is taken to be in the form of $D_{10}(E/10\ {\rm GeV})(B/10\ \mu{\rm G})^{-1}\ {\rm cm}^{-2}\ {\rm s}^{-1}$ with a numerical coefficient, D_{10}. Observations of cosmic-rays suggest that $D \sim 10^{28}\ {\rm cm}^2\ {\rm s}^{-1}$ at 10 GeV (Berezinskii et al. 1990 [31]). On the other hand, near SNRs, GeV and TeV observations suggest $D \sim 10^{26}\ {\rm cm}^2\ {\rm s}^{-1}$ at 10 GeV (e.g., Torres et al. 2008 [181]). We adopt $D_{10} = 3 \times 10^{27}$ so that $D \sim 10^{28}\ {\rm cm}^2\ {\rm s}^{-1}$ for $B = 3\ \mu$G, a typical field in interstellar space, and $D \sim 10^{26}\ {\rm cm}^2\ {\rm s}^{-1}$ for $B \sim 100\ \mu$G, which could be attained for SNRs.

4.3.2 Radio

The synchrotron radio flux at 1 GHz is given by integrating the power per unit volume per unit frequency of synchrotron emission from a single electron (equation (2.55)) over electron distribution of $N_{\rm e}$ and over the volume of shocked ISM shell and dividing by $4\pi d^2$;

$$F_{\rm syn}(\nu) = \frac{1}{4\pi d^2} \int \frac{\sqrt{3} e^3 B^{(\mu+1)/2} K_{\rm e}}{2 m_{\rm e} c} \left(\frac{16 m_{\rm e} c^5 \nu}{3e} \right)^{-(\mu-1)/2} \times \left[\int_{x_{\rm b}}^{x_{\rm inj}} F(x) x^{(\mu-3)/2} dx + E_{\rm b}^{-\mu+\mu_2} \left(\frac{16 m_{\rm e}^3 c^5 \nu}{3eB} \right)^{(\mu-\mu_2)/2} \int_{x_{\rm max}}^{x_{\rm b}} F(x) x^{(\mu_2-3)/2} dx \right] 4\pi r^2 dr, \quad (4.13)$$

where

$$x = \frac{16 m_{\rm e}^3 c^5 \nu}{3eBE^2}. \quad (4.14)$$

The integration interval of r is give by the shocked ISM shell, defined in section 3.3.1. The characters "inj", "b", and "max" correspond to injection, break, and maximum energy, respectively. Figure 4.4 shows the time evolution of the 1 GHz flux for the magnetic field in figure 4.3. Since the blast wave is little decelerated, the radio flux continues to increase through ~ 10000 yr (see discussion).

4.3.3 Gamma-Rays

We calculate GeV γ-ray emission to bremsstrahlung, inverse-Compton scattering off the cosmic microwave background, and π^0-decay. The γ-ray intensity is given by The bremsstrahlung γ-ray luminosity is is given by integrating the power per unit volume per unit frequency of these γ-ray emission from a single particle over particle distribution. The bremsstrahlung γ-ray luminosity is

$$\frac{dN_\gamma}{dtdh\nu dV} = \frac{4\alpha r_0^2 c n_{\rm T}}{h\nu} \left[\ln\left(\frac{4h\nu}{m_{\rm e}c^2} \right) - \frac{1}{2} \right] \int_{h\nu}^{E_{\rm max}} N_{\rm e} E^{-2} \left[\frac{4}{3}E^2 - \frac{4}{3}Eh\nu + (h\nu)^2 \right] dE$$

$$\simeq 4\alpha r_0^2 c K_{\rm e} n_{\rm T} \left[\ln\left(\frac{4h\nu}{m_{\rm e}c^2} \right) - \frac{1}{2} \right] \begin{cases} \dfrac{(3\mu^2+\mu+4)(h\nu)^{-\mu}}{3\mu(\mu-1)(\mu+1)} - \dfrac{4(\mu_2-\mu)E_{\rm b}^{-\mu+1}(h\nu)^{-1}}{3(\mu-1)(\mu_2-1)} \\ \quad + \dfrac{4(\mu_2-\mu)E_{\rm b}^{-\mu}}{\mu\mu_2} - \dfrac{(\mu_2-\mu)E_{\rm b}^{-\mu-1}h\nu}{(\mu+1)(\mu_2+1)}, \ h\nu \le \dfrac{E_{\rm b}}{2} \\ \dfrac{(3\mu_2^2+\mu_2+4)(h\nu)^{-\mu_2}}{3\mu_2(\mu_2-1)(\mu_2+1)}, \ h\nu > \dfrac{E_{\rm b}}{2}. \end{cases} \quad (4.15)$$

The inverse-Compton γ-ray luminosity is

$$\begin{aligned} \frac{dN_\gamma}{dtdh\nu dV} &= \frac{8\pi^2 r_0^2 K_{\rm e} E_{\rm b}^{-\mu+\mu_2}}{h^3 c^2 (m_{\rm e}c^2)^{\mu_2-1}} (kT_{\rm CMB})^{(\mu_2+5)/2} \\ &\quad \times \left[\frac{2^{\mu_2+3}(\mu_2^2+4\mu_2+11)}{(\mu_2+3)^2(\mu_2+5)(\mu_2+1)} \Gamma\left(\frac{\mu_2+5}{2} \right) \zeta\left(\frac{\mu_2+5}{2} \right) (h\nu)^{-(\mu_2+1)/2} \right. \\ &\quad \left. - \frac{2^{\mu_2+2}\pi^2}{3(\mu_2+1)} \left(\frac{m_{\rm e}^2 c^4}{4 E_{\rm max,e} k T_{\rm CMB}} \right)^{(\mu_2+1)/2} h\nu \right], \end{aligned} \quad (4.16)$$

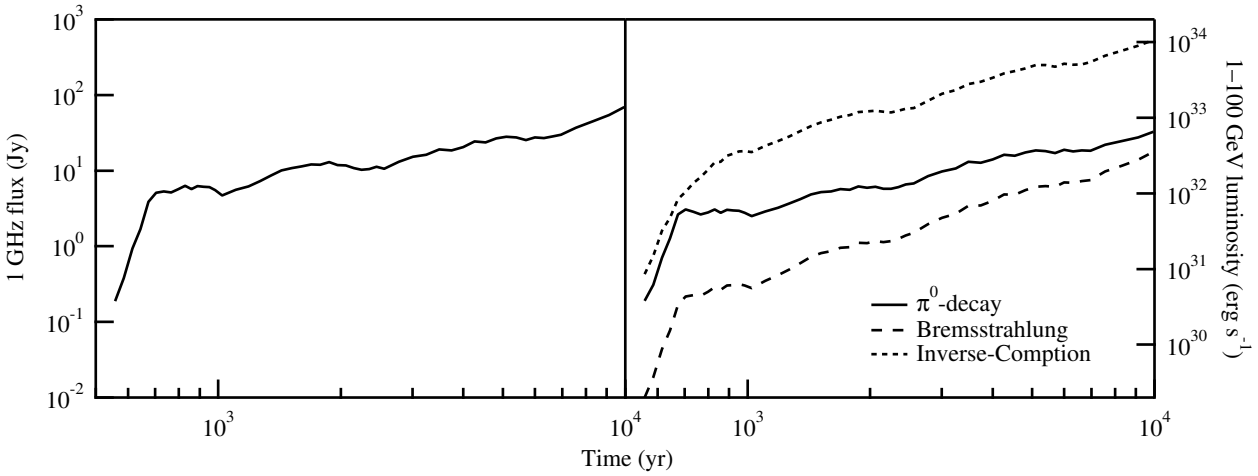

Figure 4.4: Left: Radio flux at 1 GHz of synchrotron radiation from the blast-shocked ISM shell as a function of elapsed time after the explosion, calculated for $\xi_{\rm e} = 10\xi_{\rm p}$ and $d = 8$ kpc. Right: Luminosities of bremsstrahlung (broken), inverse-Compton scattering (dotted), π^0-decay (solid) γ-rays from the blast-shocked ISM shell in the $1 - 100$ GeV band.

where Γ is the gamma function and ζ is zeta function. The second term represents an effect of cut-off at maximum energy. The π^0-decay γ-ray luminosity is

$$\frac{dN_\gamma}{dtdh\nu dV} \simeq 3\times10^{-26}\frac{2cn_{\rm T}K_{\rm p}}{f_\pi} \times \begin{cases} \frac{1}{\mu}\left(\frac{h\nu}{f_\pi}\right)^{-\mu}\left\{0.95+0.06\left[\ln\left(\frac{h\nu/f_\pi}{1\ {\rm GeV}}\right)+\frac{1}{\mu}\right]\right\} \\ \quad + E_{\rm b}^{-\mu}\left[0.95\left(\frac{1}{\mu_2}-\frac{1}{\mu}\right)+0.06\left(\frac{1}{\mu_2^2}-\frac{1}{\mu^2}\right)+0.06\left(\frac{1}{\mu_2}-\frac{1}{\mu}\ln\left(\frac{E_{\rm b}}{1\ {\rm GeV}}\right)\right)\right], \\ \qquad\qquad \text{for } h\nu \le f_\pi E_{\rm b}, \\ \frac{E_{\rm b}^{-\mu+\mu_2}}{\mu_2}\left(\frac{h\nu}{f_\pi}\right)^{-\mu_2}\left\{0.95+0.06\left[\ln\left(\frac{h\nu/f_\pi}{1\ {\rm GeV}}\right)+\frac{1}{\mu_2}\right]\right\}, \text{ for } h\nu > f_\pi E_{\rm b}, \end{cases} \quad (4.17)$$

Integrating these γ-ray intensities over the volume of shocked ISM shell,

$$L = \int\int h\nu\frac{dN_\gamma}{dtdh\nu dV}4\pi r^2 dr dh\nu, \quad (4.18)$$

we get the γ-ray luminosity. The integration interval of r is give by the shocked ISM shell, defined in section 3.3.1. We calculated the bremsstrahlung and π^0-decay luminosity using $\langle n^2\rangle$ obtained from hydrodynamical calculation in section 3.2. Figure 4.4 shows the time evolution of the γ-ray luminosities due to bremsstrahlung, inverse-Compton scattering, and π^0-decay in the 1–100 GeV band.

Chapter 5

Discussion

We discuss dynamical evolution of the SNRs in the rarefaction scenario in section 5.1. With the understanding of evolution, we discuss temperatures and ionization states of X-ray emitting matter in section 5.2.1. In table 5.1 we summarize the temperatures and blast-wave radii at characteristic epochs, $t_{\rm b}$ and $t_{\rm d}$ (see below), for each model. We see that the matter become over-ionized states because of the rarefaction after the break-out, and those in model B2 remain in the over-ionized state for the longest time of all the models concerned in the present thesis in section 5.2.1. Using model B2, we discuss X-ray emission measures, which are proportional to X-ray surface brightnesses, in section 5.2.2, and radio and γ-ray radiation in section 5.3. Lastly, the rarefaction scenario and other scenarios of MM SNRs are compared with radio and X-ray observations in section 5.4.

Table 5.1: Characteristic epochs, and the ejecta temperature and the blast-wave radius at that epochs.

Model	Break-out			$T_{\rm z} - T_{\rm e}$ decoupling		
	$t_{\rm b}$ (yr)	$T(10^7$ K)	$R_{\rm b}$ (pc)	$t_{\rm d}$ (yr)	$T(10^7$ K)	$R_{\rm b}$ (pc)
A1	41	1.3	0.30	180	0.20	1.7
A2-e	46	1.2	0.30	210	0.18	1.8
A2-p	17	1.6	0.15	80	0.16	0.99
A3-e	47	1.4	0.30	220	0.21	1.8
A3-p	11	0.8	0.10	60	0.11	0.81
B1-e	46	1.2	0.30	190	0.23	2.0
B1-p	17	1.7	0.15	80	0.10	1.1
B2-e	450	1.2	3.0	70	1.7	0.64
B2-p	170	1.1	1.5	36	1.2	0.38

The characters "e" and "p" attached to models A2−B2 mean the equatorial and polar directions, respectively.

5.1 Dynamical Evolution

Before the break-out, the evolution of SNR can be described by a self-similar solution, and the blast wave expands as $r_{\rm b} \propto t^{\alpha}$. Almost independently of anisotropy of the CSM (models A1–3), the values of α are close to each other both in the polar and equatorial directions, as seen in the *upper* panel of figure 5.1. After the break-out, α values are slightly larger in larger a models, but approach the value of model A1 ($a = 1$) with time. This implies that the blast wave approaches spherical symmetry with time, and the ratio of the blast-wave radius of the polar to equatorial direction becomes less than ~ 1.2 in 1000 years in any model of ours here.

If the density difference across the interface between the CSM and ISM is large enough (models A1–3 and B1), the blast wave gets faster just after the break-out by a factor of ~ 2, almost independent of the density difference. On the other hand, if the density difference is as small as model B2, the velocity increases by a factor of ~ 1.4. The expansion velocity of a spherical fluid initially at rest asymptotically approaches its maximum value of $2c_{\rm s}/(\gamma - 1)$, where $c_{\rm s}$ is a sound speed of the fluid (Zel'dovich and Raizer 1966 [208]). Similarly, denoting the shock velocity by $V_{\rm S}$, we may have the maximum expansion velocity after the break-out, as

$$\frac{2}{\gamma - 1}[c_{\rm s}^2 + V_{\rm s}^2(t_{\rm b})]^{1/2} \simeq 2.0\, V_{\rm s}(t_{\rm b}), \tag{5.1}$$

where $V_{\rm S}(t_{\rm b})$ is the shock velocity of the blast wave immediately before the break-out at $t = t_{\rm b}$. Here we take the Rankine-Hugoniot relation of strong shocks into account. This estimate is consistent with the result of our hydrodynamical calculation. The high shock velocity and rarefaction caused by the break-out may be in favor of particle acceleration, because the former boosts the maximum energy of particles (see section 5.3), and the latter works for particles to become non-thermal.

5.2 X-rays

5.2.1 Thermal and Ionization State

As demonstrated by Itoh and Masai (1989) [95], rarefaction by the blast-wave break-out rapidly cools the shock-heated matter to be an over-ionized/recombining plasma of $T_{\rm e} < T_{\rm z}$. This recombining plasma state lasts until the second reverse shock reheats the matter to $\gtrsim T_{\rm z}$. Although ionization is not calculated simultaneously with hydrodynamics, we can analyze the ionization state, i.e., ionizing, equilibrium or recombining, of the shocked matter from the electron temperature and density. The ionization state thus evaluated is consistent with Itoh and Masai (1989) [95], considering the variation of epochs and duration that depend on the CSM/ISM models, as discussed in the previous sections.

The *upper* panels of figures 5.2a (model B1) and 5.2b (model B2) show the evolution of the ion and electron temperatures averaged over the shocked matter of the ejecta. Before the break-out, $T_{\rm e}$ becomes nearly equal to $T_{\rm i}$ due to high densities of the CSM. Also after the break-out and until arrival of the second reverse shock, $T_{\rm e}$ is nearly equal to $T_{\rm i}$, because

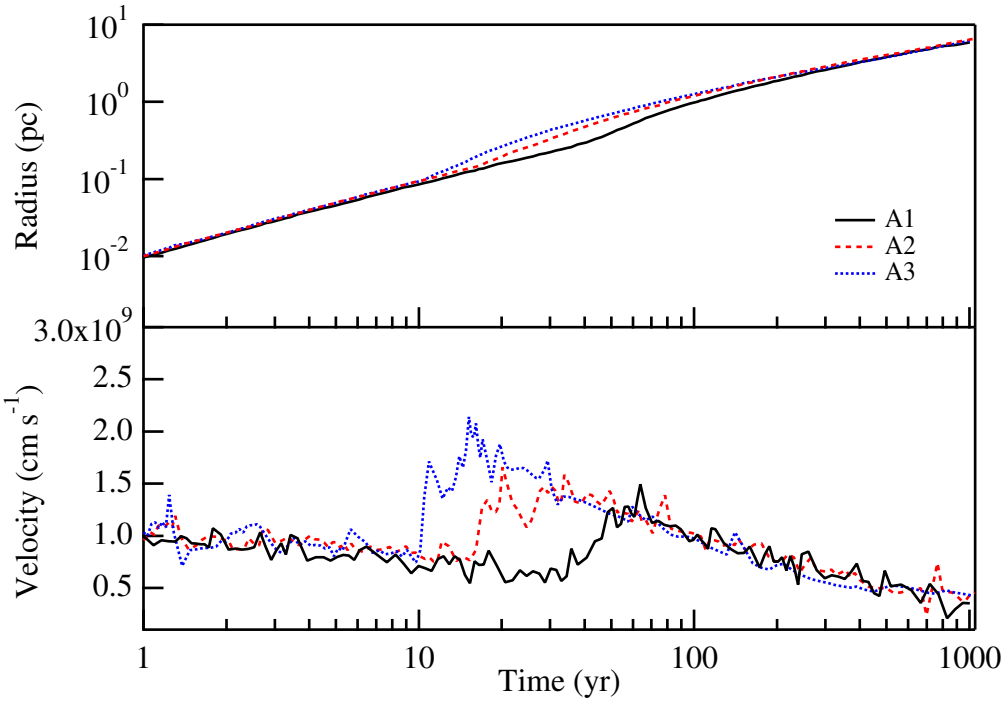

Figure 5.1: Radius and velocity of the blast wave in the polar direction for models A1 (black solid lines), A2 (red dashed lines), and A3 (blue dotted lines), as functions of elapsed time after explosion.

cooling is due to adiabatic expansion. By the second reverse shock, $T_{\rm i}$ rises faster than $T_{\rm e}$, and then $T_{\rm e}$ rises through the energy transport from ions, as shown in the *upper* panels of figure 5.2.

In the *lower* panels, we show the average density of the shocked ejecta by the solid line. Ionization by electron-impact becomes equilibrium with time-scale τ given by $\rho\tau \sim 10^{12}$ amu cm^{-3} s, almost independent of the temperature or ion species (Masai 1994 [121]). We also plot this relation as $\rho_{\rm crit} = 10^{12}\, t^{-1}$ amu cm^{-3} with the dashed line in the *lower* panels. Well before the break-out, since the density is high enough ($\rho > \rho_{\rm crit}$) due to the presence of CSM, ionization quickly reaches its equilibrium at $T_{\rm e}$, i.e. $T_{\rm z} \sim T_{\rm e}$.

As the SNR expands, the average density of the shocked matter decreases approximately as $\rho \propto t^{-2}$. When rarefaction occurs by the break-out, ρ decreases faster as $\propto t^{-3}$ (see section 4.2.1). Therefore, ρ becomes below $\rho_{\rm crit} \propto t^{-1}$, as seen in the *lower* panels of figure 5.2, and $T_{\rm z}$ is decoupled from $T_{\rm e}$. In other words, recombination no longer follows the rapid decrease of the electron temperature, and the ionization state freezes roughly at $T_{\rm z} \sim T_{\rm e}(t_{\rm d})$, where $t_{\rm d}$ is the epoch at which $\rho = \rho_{\rm crit}$.

The decoupling epoch $t_{\rm d}$ is also shown in the *lower* panels of figure 5.2 with the thin-dotted vertical line. In model B1, $t_{\rm d} \sim 190$ yr in the equatorial direction. Note that $t_{\rm d} > t_{\rm b}$ and $T_{\rm e}(t_{\rm d}) < T_{\rm e}(t_{\rm b})$ in model B1, where $T_{\rm e}(t_{\rm b})$ is the electron temperature immediately before the break-out. Models A1–3 show the similar behavior to model B1 described here.

In model B2, unlike other models or Itoh and Masai (1989) [95], the CSM is located away

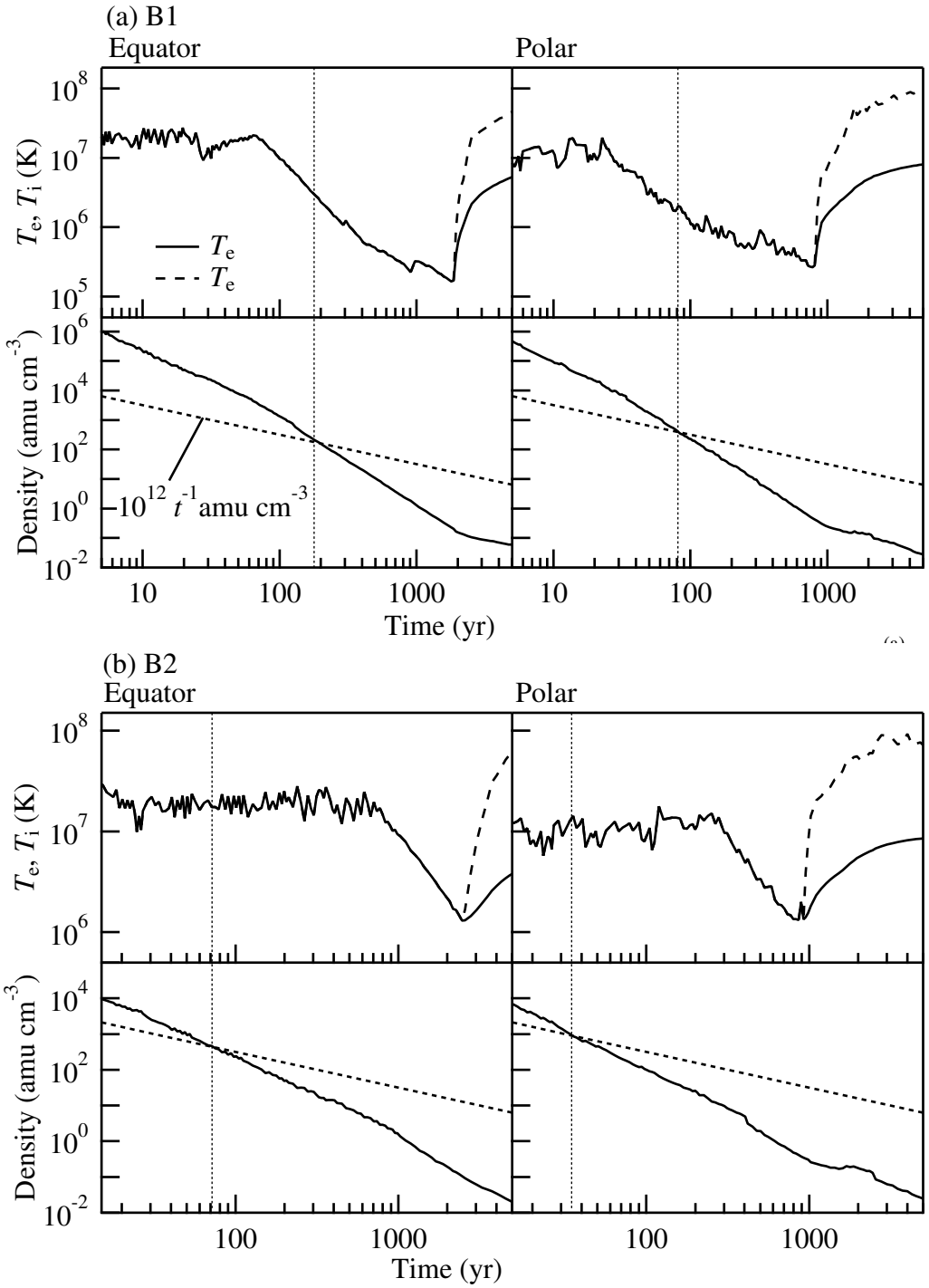

Figure 5.2: Model (a) B1 and (b) B2: Averaged temperature and density of the shocked ejecta in the equator (*left*) and polar (*right*) directions, as functions of the elapsed time after explosion. *Upper*: The solid and broken lines represent the electron and ion temperatures, respectively. *Lower*: The solid and dashed lines represent the density and $\rho_{\rm crit} = 10^{12}\,t^{-1}$ amu cm^{-3}, respectively, and the thin-dotted vertical lines represent the decoupling epoch $t_{\rm d}$ (see text).

from the progenitor, and hence the density is low. Therefore, the break-out occurs later but ρ becomes below $\rho_{\rm crit}$ earlier than in model B1. As seen in figure 5.2b, $t_{\rm d} < t_{\rm b}$ in model B2, and $t_{\rm d} \sim 70$ yr in the equatorial direction. In fact, as is seen in the *upper* panel, $T_{\rm e}$ before the break-out is nearly constant at $\sim T_{\rm e}(t_{\rm b})$ in model B2. As a result, the ionization temperature of the recombining plasma is higher in model B2 than that in model B1.

When the second reverse shock reaches the ejecta, the temperature turns to rise, as seen in the *upper* panels of figure 5.2. If the electron temperature exceeds or becomes comparable to $T_{\rm z} \sim T_{\rm e}(t_{\rm d})$, the ionization state turns to be ionizing or nearly equilibrium. This is the case for models A1–3 with a higher ISM density. In model B1, though the ISM density is low, $T_{\rm e}$ exceeds $T_{\rm z}$ in 3000 years owing to the dense CSM and lower $T_{\rm z}$. On the other hand, in model B2, the density is too low for the second reverse shock to raise $T_{\rm e} > T_{\rm z}$ in such short time, and the over-ionization state remains much longer. If $T_{\rm i}$ becomes higher than $2T_{\rm z}$ at the shock front, $T_{\rm e} \gtrsim T_{\rm z}$ may be attained by the energy transfer from ions. Since $T_{\rm i} \propto V_{\rm S}^2$ (reverse shock) decreases with the age, however, the recombining state would last yet for thousands years.

After decoupled from the electron temperature, the ionization temperature decreases by recombination with time-scale τ. We note here that the recombination time-scale $\sim 10^4$ yr (Masai 1994 [121]) is longer than the age of over-ionized SNRs: ~ 4000 yr for IC443 (Troja et al. 2008 [182]) and $1000 - 4000$ yr for W49B (Pye et al. 1984 [145]; Smith et al. 1985 [170]; Hwang et al. 2000 [93]).

5.2.2 Emission Measure

Almost all the SNRs with over-ionized/recombining plasma so far observed are mixed-morphology SNRs, which exhibit center-filled X-ray emission and shell-like radio emission. Hence, we investigate distribution of the X-ray emission measure for SNRs with anisotropic stellar wind. We integrate the density square along the line of sight, as $\int \rho^2 dl$, i.e. the emission measure, and show the map (black lines) for model B2 in the left panel of figure 5.3. The right panel of figure 5.3 shows the radial distribution of the emission measure in red square region of the map. Here the shocked matter of $T > 10^6$ K, which is responsible for X-ray emission, is taken into calculations.

At ages 980 yr and 1800 yr, we can see a bar-like structure (horizontal) with diffuse wings in the equatorial view, while a thin and thick shell in the polar view and 45° view, respectively. The emission measure is dominated by the shock-heated ejecta, which is a recombining plasma as seen from figure 5.2b. The temperature dependence of the line emissivity is weaker in recombining than in equilibrium, and the emission-measure map reflects roughly the X-ray surface brightness.

The bar structure is clearer at younger ages after the break-out, and diffuses out gradually with time. At 1800 yr, the second reverse-shock front appears to surround the bar/wing structure, and thereby the bar-end structure is being distorted. The second reverse-shock propagates inward and eventually sweeps the bar/wing structure out. Hence, the late-phase SNR approaches shell-like regardless of the viewing angle, as seen at 10000 yr in figure 5.3, where a little elongated shape with a narrow middle part is still seen in the equatorial view.

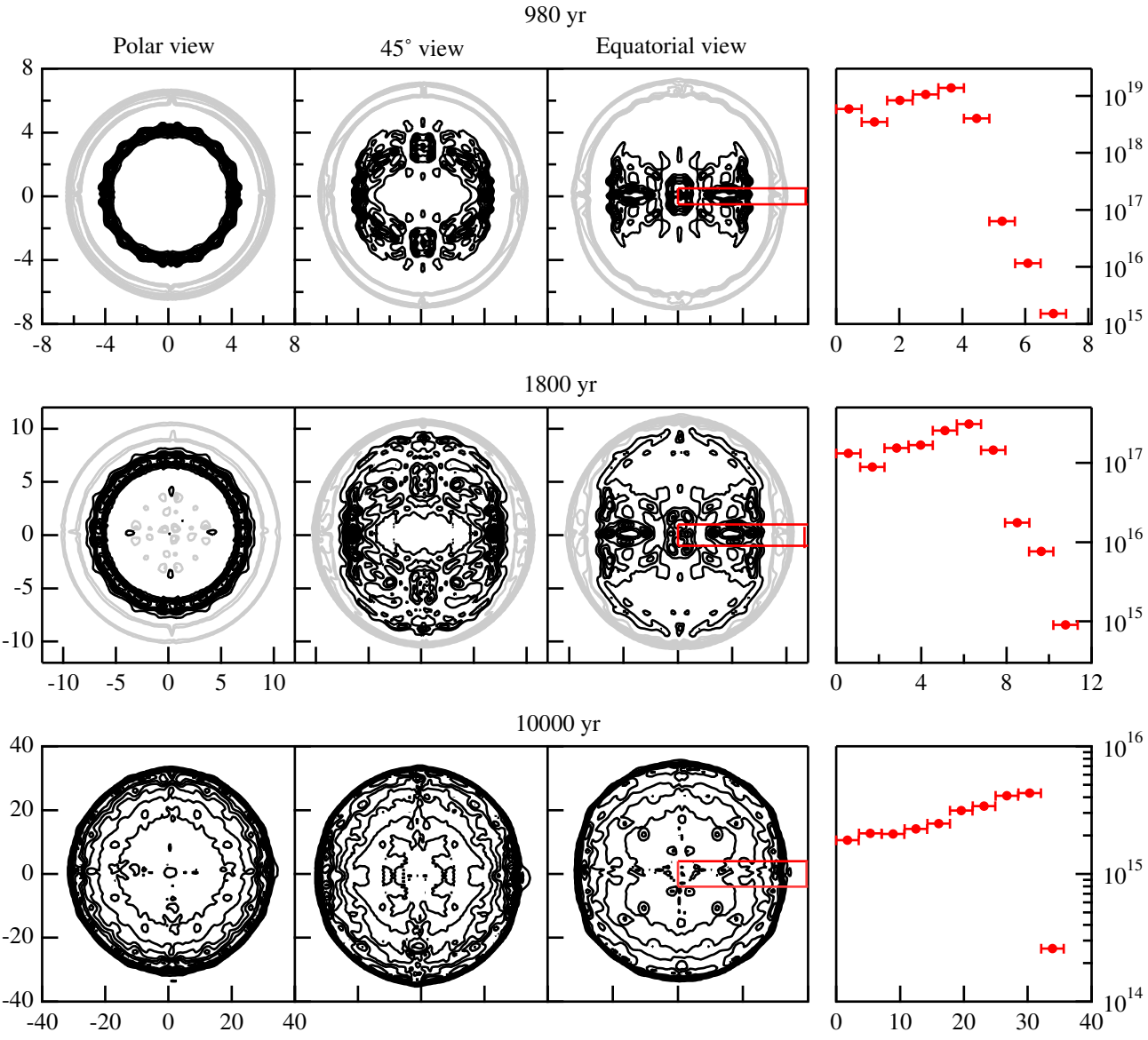

Figure 5.3: Left: Contours of the X-ray emission measure viewed from the polar direction, at an angle of 45 degrees to the polar axis, and from the equatorial directions of model B2 are drawn by black lines linearly from zero, every 1×10^{19} amu^2 cm^{-5} to the maximum $\sim 1.3 \times 10^{20}$ amu^2 cm^{-5} at 980 yr, every 5×10^{17} amu^2 cm^{-5} to the maximum $\sim 3.8 \times 10^{18}$ amu^2 cm^{-5} at 1800 yr, and every 2×10^{16} amu^2 cm^{-5} to the maximum $\sim 1.9 \times 10^{17}$ amu^2 cm^{-5} at 10000 yr, after explosion. The grey contours represent the low-level emission measure drawn linearly from zero, every 1×10^{16} amu^2 cm^{-5} up to 1.0×10^{17} amu^2 cm^{-5} at 980 yr, every 1×10^{16} amu^2 cm^{-5} up to 1.0×10^{17} amu^2 cm^{-5} at 1800 yr. The horizontal and vertical axes show the scale in units of pc. Right: Radial distribution of emission measure averaged over a red square region for equatorial view, which are shown in left panel.

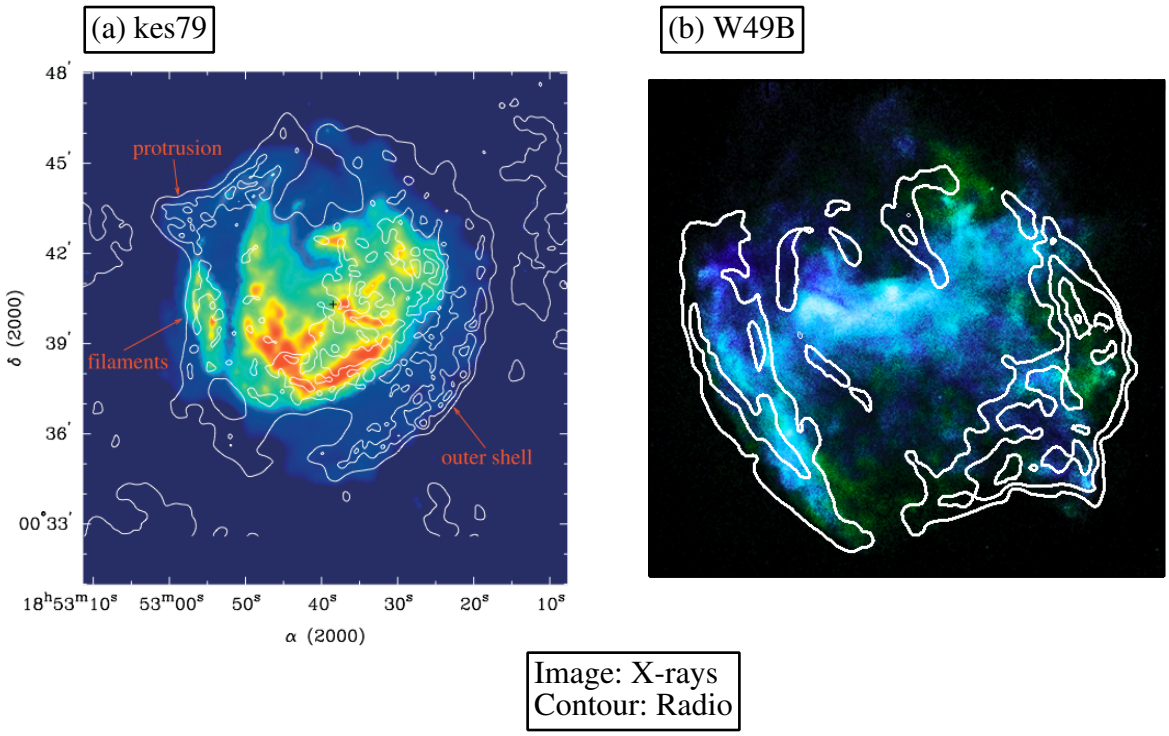

Figure 5.4: X-ray and radio surface brightnesses of MM SNRs: (a) $0.5-3$ keV X-rays and 1.5 GHz radio of kes79 (Sun et al. 2004 [176]) and (b) X-rays and radio of W49B (X-ray and radio images are available online at http://chandra.harvard.edu/photo/2013/w49b/). The words enclosed by square are added by the author.

W49B shows a bar-like structure as well as a recombining plasma state (Ozawa et al. 2009 [136]). The bar and its east-end observed with *Chandra* (Keohane et al. 2007 [106]) look similar to our calculation shown in figure 5.3. Thus we suggest that W49B is the case of nearly equatorial view for the SNR of a massive progenitor which exploded in its past stellar wind. It should be noted that, in our calculation, the structure of the bar-end is formed by the reverse shock, not by the collision with a molecular cloud near the bar-end. We show X-ray and radio surface brightnesses of W49B in figure 5.4 for comparison, and also those of kes 79, which exhibit X-ray ring-like structure within the radio shell and may be the case of the polar view.

The grey lines in the left panel of figure 5.3 represent the low-level emission measure, much smaller than that represented by the black lines, as shown in the right panel of that. One can see the blast-wave front in the grey lines. The shocked matter in the grey lines is hardly observed in X-rays, but the shock accelerates electrons to be of order of GeV (see 4.3.1), which can be responsible for GHz synchrotron radio. Hence the synchrotron radio appears to be shell-like regardless of the viewing angle because the blast wave expands spherically after the break-out.

5.3 Non-Thermal Particles and Radio and Gamma-Ray Radiation

For the low density ISM of density 0.016 cm^{-3} in the model B2, supposed for an H II region (e.g., formed by the progenitor and extended to a few tens pc), the blast wave is little decelerated through $\sim$ 10000 yr. As a result, in the context of diffusive shock acceleration described in section 3.3.1, the radio flux continues to increase, because the increase of the emission measure overcomes the decrease of the magnetic field strength. Consequently, for about ten thousand years, recombination-radiation X-rays are observed from the irregular-shape inner part of SNR (see section 5.3), while the radio emission of tens Jy is observed from the blast-shocked ISM shell.

In the beginning of the Sedov-Taylor phase where the blast wave is being decelerated significantly as $V_\mathrm{s} \propto t^{-3/5}$, the radio flux turns to decrease slowly as $t^{-3/10}$, and then approaches nearly constant as the magnetic field approaches its interstellar value ($\sim$ 3 μG) and T_e approaches T_p. Also the inverse-Compton γ-rays turns to decrease as $\propto t^{-1/5}$ in the Sedov-Taylor phase, while π^0-decay γ-rays are nearly constant. This sort of analysis is done also for the phase $\lesssim$ 10000 yr with the relation $V_\mathrm{s} \propto t^{-s}$ where s is given by the hydrodynamical calculation, and gives a good agreement with the computed time evolution of the radio and γ-ray emission in figure 4.4. It should be noted that $s \sim 0.4$ at 10000 yr, yet smaller than the Sedov value $s = 3/5$, and the SNR is in the transient phase to the Sedov-Taylor regime.

Again because of low density, the γ-ray luminosity of the shocked ISM shell is dominated by inverse-Compton scattering through the SNR evolution concerned. However, π^0-decay γ-rays could be enhanced by interactions with dense external matter, e.g., dense H I gas, molecular clouds or a cavity wall formed by the stellar wind of the progenitor. If 10% of accelerated protons interact with such matter of density $n \sim 100$ cm^{-3}, the luminosity L_π would exceed 10^{35} erg s^{-1} at a few thousands year, comparable to the typical γ-ray luminosity of MM SNRs. The interactions with molecular clouds are suggested in many MM SNRs by OH maser and/or near-infrared observations. The interaction with HI gas is suggested in RX J1713.7-3946 by observations (Fukui et al. 2012 [68]), and may be expected also in MM SNRs.

Finally, we mention the effect of the CSM, stellar wind matter here. An important effect of the CSM is that the shock break-out raises the maximum energy E_max to $\sim$ 1300 TeV for protons (see figure 4.3). Since $E_\mathrm{max} \propto BV_\mathrm{s}^2 t \propto V_\mathrm{s}^3 \propto (E_\mathrm{ej}/M_\mathrm{ej})^{3/2}$, where E_ej and M_ej are the initial kinetic energy of ejecta and the ejecta mass, respectively, E_max would reach $\sim$ 3000 TeV, the cosmic-ray knee energy, for 2 times larger value of $E_\mathrm{ej}/M_\mathrm{ej}$ than that in the present model.

5.4 Compared with Observations

The low X-ray/radio flux ratios of MM SNRs (figure 3.1) can be explained by the rarefaction scenario. The model predicts low temperature and low X-ray emissivity from a recombining

plasma (Itoh and Masai 1989 [95]). Also the increase in the flux ratios of MM SNRs with the 1 GHz surface brightness, $\Sigma_{1\ \mathrm{GHz}}$ (figure 3.1), can be explained by the model. In the model, the flux ratio is roughly proportional to $\Sigma_{1\ \mathrm{GHz}}^{3/2}$ while the radio luminosity, L_{radio}, is constant with time, because the X-ray luminosity, L_{X}, is roughly proportional to the inverse cube of a radius of SNR, R^{-3}. This relation is shown in figure 3.1 as a dotted line. The slope of the line is consistent with observations. A distribution of MM SNRs along the line reflects their radii.

The X-ray/radio flux ratio of MM SNR G272.2–3.2 is larger than those of other MM SNRs by two order of magnitude for a value of $\Sigma_{1\ \mathrm{GHz}}$ (figure 3.1). The high flux ratio may be due to low magnetic field strength. If the magnetic field strength, B, in G272.2–3.2 is $\sim 10^{-1}$ times as much as those in other MM SNRs, which are typically ~ 100 μG, the flux ratio and $\Sigma_{1\ \mathrm{GHz}}$ of G272.2–3.2 are $\sim 10^{3/2}$ and $10^{-3/2}$ times as much as those of other MM SNRs, respectively, because the synchrotron radio emissivity is proportional to $B^{3/2}$. In this case, B in G272.2–3.2 is $\sim 10\mu$G, which is attainable by shock compression of the interstellar magnetic field. Such magnetic field strength suggests that magnetic field amplifications do not work in the SNR.

Other models of MM SNRs based on cloud evaporation (White and long 1991 [194]), projection (Hnatyk and Petruk 1999 [90] and Petruk 2001 [141]), and evolution in radiative phase (Cox et al. 1991) are proposed. We also discuss these three models.

Cloud evaporation: White and long (1991) [194] investigate evolution of a SNR in a clumpy medium that contains dense clouds with small volume filling factor and rather low density inter-cloud gas, considering evaporation of the clouds by thermal conduction in the post shock region. In this model, L_{X} is roughly proportional to $R^3 n_0^2 \Lambda$, where n_0 is the number density of pre-shocked inter-cloud gas and Λ is the cooling function.

If Λ is proportional to the power-law of temperature, T^n, L_{X} is proportional to $R^{3(1-n)}$, where for T we use the shock temperature in Sedov phase. While L_{radio} is constant with time, the X-ray/radio flux ratio is proportional to $\Sigma_{1\ \mathrm{GHz}}^{-3(1-n)/2}$. Since $n \lesssim 0.5$ for a plasma of cosmic abundance, the model can not explain the increase in the flux ratios of MM SNRs with $\Sigma_{1\ \mathrm{GHz}}$.

Projection: Evolution of a SNR in the ISM with a large-scale density gradient is investigated by Hnatyk and Petruk (1999) [90] and Petruk (2001) [141]. Hnatyk and Petruk (1999) [90] find that the X-ray emission measure and temperature of such SNR are close to those of a SNR in Sedov phase with the same initial parameters. This can not explain the low X-rays/radio flux ratios of MM SNRs.

Radiative phase: Cox et al. (1999) [50] investigate a SNR in the radiative phase for a model of W44. In this model, the radio is emitted from cosmic-ray electrons swept by the blast wave. If the swept-up electrons are Galactic cosmic-rays, the spectral index of the electrons would be about 3 (e.g., Adriani et al. 2011 [10]; Ackermann et al. 2012 [8]), which is not consistent with the average of radio indices of MM SNRs (table 7.1).

Chapter 6

Summary

We investigate the dynamical evolution and high-energy radiation of SNRs that explode in the progenitors' stellar wind matter, considering possible environments of mixed-morphology SNRs with over-ionized plasmas. We summarize the results;

- When the blast wave breaks out of the wind matter into the ambient interstellar medium, the shocked matter cools rapidly due to adiabatic expansion. Just after the break-out, the expanding velocity becomes faster by a factor up to two, and then gradually decreases to that of the extrapolated from the velocity trend before the break-out.
- Before the break-out, the shocked matter reaches ionization equilibrium and equipartition $T_{\rm e} \sim T_{\rm i}$, but deviates from equilibrium by rarefaction after the break-out. Consequently, the shock-heated ejecta turns to be a recombining plasma, since cooling due to adiabatic expansion is much faster than recombination.
- The recombining state of the shocked ejecta lasts until the second reverse shock, which occurs by the interaction with the interstellar medium, propagates inward and reheats the ejecta. If the density of the ejecta is too low to establish ionization equilibrium, however, the recombining state lasts longer.
- After the break-out in the adiabatic phase, since the emission measure of the shocked ejecta is much larger than that of the shocked ambient matter, the SNR in X-ray wavelengths appears much brighter in the reverse-shocked inner region than the blast-shocked outer shell.
- When the stellar wind matter is not isotropic but denser in the equatorial direction due to the progenitor's rotation, the SNR in the recombining state looks bar-like with wings in the equatorial view and thin shell-like in the polar view. So that, the SNR would show center-filled various shapes in X-rays, depending on the viewing angle. On the other hand, the blast-shocked matter, which is very faint in X-rays but are observed in radio, forms a fairly complete shell outside. The 1 GHz flux of synchrotron radiation from the shell reaches tens of Jy, which is comparable to typical observational values of MM SNRs. Therefore the rarefaction scenario can explain the center-filled thermal X-rays emitted from over-ionized plasma within the radio shell of MM SNRs.
- As the SNR age increases, however, the second reverse shock sweeps the bar/wing

structure out and merges into the whole ejecta eventually. Hence, the bar/wing structure disappears and the late-phase SNR would look shell-like almost independently of the viewing angle.

- The luminosity of γ-rays emitted from the shocked-ISM shell in the $1 - 100$ GeV band is dominated by inverse-Compton scattering because of low density, but the total luminosity including also the contribution of bremsstrahlung and π^0-decay reaches $\sim 10^{34}$ erg s^{-1}, which is lower than typical values of observations of MM SNRs, which are $10^{34} - 10^{36}$ erg s^{-1}. However, if about 10% of accelerated protons interact dense external matter, i.e., molecular clouds or H I gas, of the density of 100 cm^{-3}, the π^0-decay γ-ray luminosity reaches 10^{35} erg s^{-1}.
- Because of the acceleration of blast wave just after the break-out, the maximum energy of accelerated protons increases to reach 1300 TeV, which is comparable with the cosmic-ray knee energy of 3000 TeV.
- The $2.1 - 10$ keV X-rays to 1 GHz radio flux ratios of MM SNRs are lower than those of shell-like SNRs at the same 1 GHz surface brightness. The low flux ratios can be explained by the rarefaction scenario that predict the over-ionized state, which has a lower X-ray emissivity than other plasma states.

Chapter 7

Prospect

We assume broken power-law spectra, which can not be explained by DSA, as energy spectra of non-thermal particles. Although an origin of broken power-laws is beyond the present thesis, we systematically investigate spectral indices of radio and γ-ray emitting particles of MM SNRs compared with shell-like SNRs in order to find observational clues. We show a list of MM and shell-like SNRs that detected in the GeV γ-ray band with their spectral indices of radio-emitting particles, GeV/TeV photon indices, and diameters in table 7.1 in the diameter order. We also show the average of these spectral indices of MM and shell-like SNRs in table 7.1. The values in the upper average rows in the GeV column in table 7.1 is calculated from spectral indices of SNR whose spectra are fitted to single power-laws, and spectral indices below the break of SNRs whose spectra are fitted to broken power-laws. The values in the lower average rows in the GeV column is calculated in the same way but spectral indices above the break are used. The average spectrum of radio emitting particles of MM SNRs are similar to that of shell-like SNRs, but slightly harder than that of all of MM SNRs of 2.0. The average spectrum of GeV and TeV γ-ray photons of MM SNRs are steeper than that of shell-like SNRs.

The sightly hard radio spectra of MM SNRs observed in the GeV γ-ray band may be due to absorption. Figure 7.1 shows a diameter distribution of radio spectra indices of MM SNRs. At a same diameter, MM SNRs observed in the γ-ray band have harder radio spectra than other MM SNRs. One possibility of the harder spectra is free-free absorption by ionized matter along the line of sight. Since all of the MM SNRs observed in the γ-ray band interact with molecular clouds, dense absorbing matter are expected outside the SNRs. Such matter absorb low frequency photons, and radio spectra become hard below a frequency at which an optical depth due to the absorption is not much smaller than unity. In fact, frequency turnover is observed in W49B (Moffett and Reynolds 1994 [128]), IC443 (Castelletti et al. [42]), and 3C391 (Brogan et al. 2005 [38]). Although the turnover, i.e., a direct evidence of absorption, is not observed in other MM SNRs, spectral hardening by absorption is expected in them because of the interactions.

The steeper γ-ray spectra of MM SNRs than shell-like SNRs are suggested by a GeV to TeV flux ratio. Such ratio reflects a slope of broadband γ-ray spectrum. We calculate the ratio of $1 - 100$ GeV flux to above 1 TeV γ-rays flux, which are taken from the references

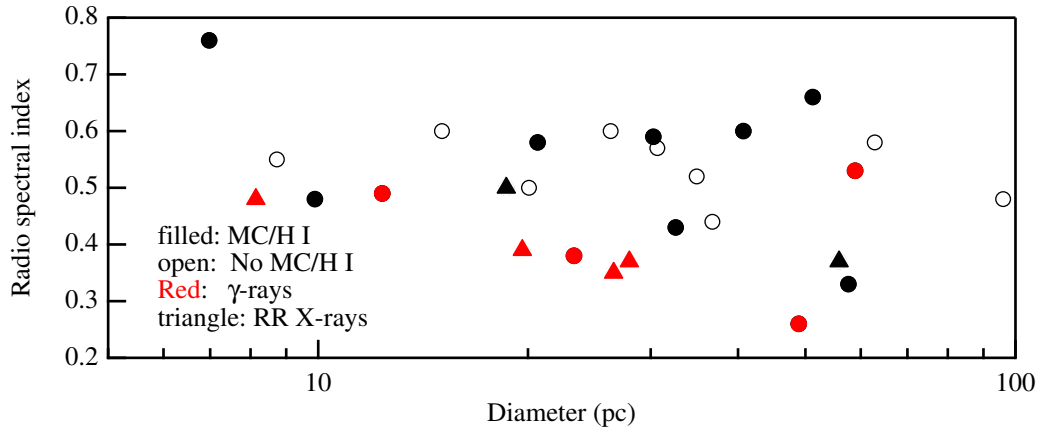

Figure 7.1: Radio spectral indices versus diameters of MM SNRs. We use geometric mean of long and short diameters for distorted SNRs. The filled and open symbols represents interaction with molecular clouds/H I gas. The red symbols represent GeV γ-rays are observed. The triangles represent recombination radiation X-rays are detected.

listed in table 7.1, and show the ratio against the diameter of SNR in figure 7.2. At the same diameter, the ratios of MM SNRs are higher than those of shell-like SNRs, i.e., the broadband γ-ray spectra of MM SNRs are steeper than those of shell-like SNRs.

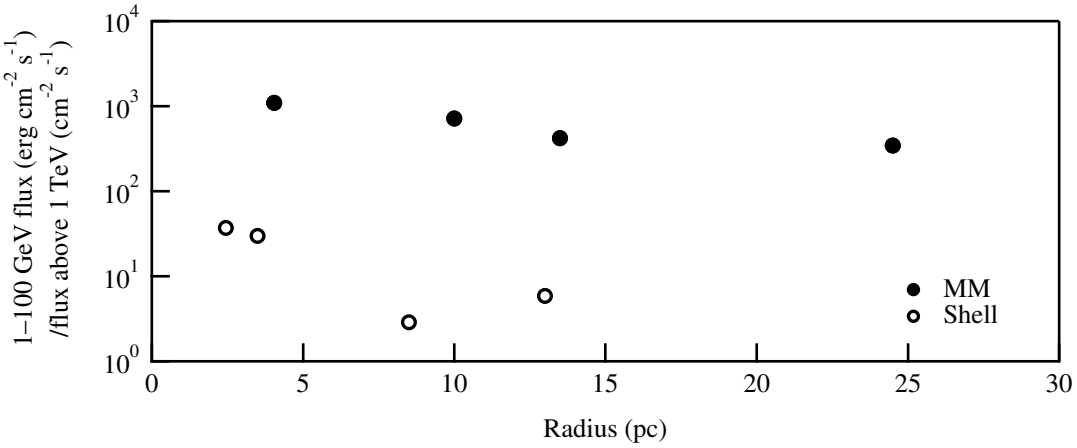

Figure 7.2: Flux ratio of $1-100$ GeV to above 1 TeV γ-rays vs. the diameter of SNR for shell-like (open diamonds) and MM SNRs (filled diamonds).

The GeV γ-rays of MM SNRs are thought to be due to π^0-decay, since all of these MM SNRs interacts with molecular clouds. In fact, the GeV γ-rays of W44 and IC443 are due to π^0-decay (Giuliani et al. 2011 [77]; Ackermann et al. 2013 [8]). Similarly, the GeV γ-rays of several shell-like SNRs are thought to be due to π^0-decay, suggested by observations: spectral break about GeV for Cas A (Yuan et al. 2013 [206]), broad band spectral fitting for Tycho (Giordano et al. 2012 [76]), and interaction with molecular clouds for G349.7+0.2 (Frail et al. 1996 [65]). In RX J1713.7-3946, although the hard GeV γ-ray spectrum prefers inverse-

Compton scattering by accelerated electrons with energy spectrum $\propto E^{-2}$ (Abdo et al. 2011 [4]), interactions with dense gas (e.g., Dame et al. 2001 [51]), which spatially correlate with the TeV γ-rays (Fukui et al. 2012), suggest that the γ-rays are due to π^0-decay. The π^0-decay γ-ray spectrum can be hard by energy-dependent penetration of accelerated protons into dense gas (Zirakashvili and Aharonian 2010 [209]), which produces the observed γ-ray index when the proton energy spectrum $\propto E^{-2}$ and diffusion coefficient proportional to the gyration radius are considered (Inoue et al. 2012 [94]). Although the γ-ray origin of other SNRs are also not clear, if the γ-rays are due to π^0-decay, spectral indices of protons emit GeV γ-rays and electrons emit radio at every these SNRs are the same, as expected in DSA, in the range of error. Assuming that π^0-decay γ-ray origin for all SNRs, we plot spectral indices of radio and γ-ray emitting particles of MM and shell-like SNRs in figure 7.3. The average spectral indices of radio and γ-ray emitting particles of shell-like SNRs are the same in the range of error, while the particle spectra of MM SNRs are steeper at high energies than low energies. In particular, spectra of particle emit GeV γ-rays above the break energy of MM SNRs are clearly steeper than those of shell-like SNRs.

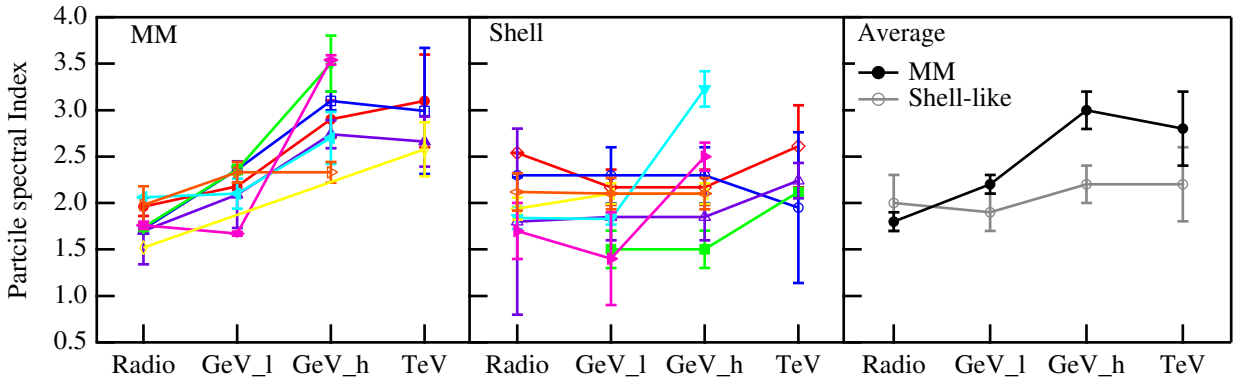

Figure 7.3: Spectral indices of particles emit radio, GeV and TeV γ-rays of MM SNRs (left) and shell-like SNRs (middle). When a GeV γ-ray spectrum is fitted to a broken power-law, the spectral indices below and above a break energy are denoted by GeV_l and GeV_h, respectively. When a GeV γ-ray spectrum is fitted to a single power-law, the spectral index is used as values of both GeV_l and GeV_h.

The steep spectra of particles emit GeV γ-rays of MM SNRs may be caused by magnetic field amplification in the shock down stream region. The pre-shocked medium of MM SNRs are thought to be highly inhomogeneous. When a shock wave interact with such medium, turbulence is generated in the shock down stream. The turbulence amplifies the magnetic field. In our model of MM SNRs, the blast wave is accelerated just after the break-out and have high velocity. The high shock velocities is favorable for the magnetic field amplification, because the growth rate and saturation field strength is proportional to the shock velocity (e.g., Fraschetti 2013 [66]). Since particles accelerations in DSA is caused by scatterings by magnetic inhomogeneity, the field amplification may affect accelerated particles spectrum.

Table 7.1: Spectral indices of radio-emitting electrons and GeV and TeV γ-ray photons of MM and shell-like SNRs in diameter order.

Name	Radio	Ref.	GeV	Ref.	TeV	Refs.	D (pc)
			MM				*
W49B	1.96 ± 0.1	[80]	2.18 ± 0.04	[3]	$3.1 \pm 0.3_{\rm stat} \pm 0.2_{\rm sys}$	[39]	9×7
			2.9 ± 0.2	[3]			
3C391	1.98 ± 0.2	[38]	2.33 ± 0.11	[43]	N		15×10
IC443	1.78 ± 0.02	[42]	$2.36 \pm 0.02^{\dagger}$	[9]	$2.99 \pm 0.38_{\rm stat} \pm 0.30_{\rm sys}$	[5]	20
			$3.1 \pm 0.1^{\dagger}$	[9]			
HB21	1.76 ± 0.04	[143]	1.67 ± 0.02	[143]	N		28×21
			3.54 ± 0.05	[143]			
W28	1.7 ± 0.4	[54]	$2.09 \pm 0.08_{\rm stat} \pm 0.28^{\ddagger}_{\rm sys}$	[2]	$2.66 \pm 0.27^{\ddagger}$	[14]	27
			$2.74 \pm 0.06_{\rm stat} \pm 0.09^{\ddagger}_{\rm sys}$	[2]			
W44	1.74 ± 0.04	[41]	$2.36 \pm 0.05^{\dagger}$	[9]	N		32×24
			$3.5 \pm 0.3^{\dagger}$	[9]			
W51C	1.52	[129]			$2.58 \pm 0.07_{\rm stat} \pm 0.22_{\rm sys}$	[17]	49
W30	2.06	[98]	$2.10 \pm 0.06_{\rm stat} \pm 0.10_{\rm sys}$	[16]	N		59
			$2.70 \pm 0.12_{\rm stat} \pm 0.14_{\rm sys}$	[16]			
Average	1.8 ± 0.1		2.2 ± 0.1		2.8 ± 0.4		
			3.0 ± 0.2				
			Shell-like				**
Cas A	2.54 ± 0.01	[22]	$2.17 \pm 0.09_{\rm stat}\,^{+0.10}_{-0.05}\,_{\rm sys}$	[206]	$2.61 \pm 0.24_{\rm stat} \pm 0.2_{\rm sys}$	[6]	5
Tycho	2.3 ± 0.02	[111]	$2.3 \pm 0.2_{\rm stat} \pm 0.1_{\rm sys}$	[76]	$1.95 \pm 0.51_{\rm stat} \pm 0.30_{\rm sys}$	[7]	7
G349.7+0.2	1.94 ± 0.12	[169]	2.10 ± 0.11	[43]	N		16×13
RX J1713.7-3946			$1.5 \pm 0.1_{\rm stat} \pm 0.1_{\rm sys}$	[4]	2.12 ± 0.03	[12]	19×16
Vela Jr.	1.8 ± 1.0	[55]	$1.85 \pm 0.06_{\rm stat}\,^{+0.18}_{-0.19}\,_{\rm sys}$	[178]	$2.24 \pm 0.04_{\rm stat} \pm 0.15_{\rm sys}$	[13]	26
Cygnus Loop	1.84 ± 0.12	[189]	1.83 ± 0.06	[99]	N		33×23
			3.23 ± 0.19	[99]			
Puppis A	2.12 ± 0.2	[87]	$2.1 \pm 0.07_{\rm stat} \pm 0.10_{\rm sys}$	[87]	N		38×32
S147	1.7 ± 0.3	[198]	1.4 ± 0.5	[103]	N		68
			2.5 ± 0.15	[103]			
Average	2.0 ± 0.3		1.9 ± 0.2		2.2 ± 0.4		
			2.2 ± 0.2				

Note. The charactors "stat" and "sys" represent statistical and systematic errors, respectively. When a GeV γ-ray spectrum is fitted to a broken power-law, we show indices below (upper in a row) and above (lower in a row) a break energy. W51C is detected in GeV band, but the γ-ray spectral index is not shown in the reference paper. Hence we leave blank in GeV index of W51C. The character "N" represents that SNR in not detected in TeV band so far.

† Particle spectral indices.

‡ Spectral index of source N in GeV band and HESS J1801-233 in TeV band in the references.

* Taken from table 3.1.

** Calculated from the radio angular diameter (Green 2009 [82]) and the distance to SNRs: 3.4 kpc to Cas A [146], 3 kpc to Tycho [86], 22 kpc to G349.7+0.2 [65], 1 kpc to RX J1713.7-3946 [67], 0.75 kpc to Vela Jr. [102], 0.5 kpc to Cygnus Loop [32], 2.2 kpc to Puppis A [151], 1.3 kpc to S147 [45].

Acknowledgement

I deeply thank Professor Masai for encouragement and helpful advice. He always teaches me attitude toward physics.

I also thank Professor Takaya Ohashi and Associate professor Yoshitaka Ishisaki for fruitful advice.

I also thank Dr. Yutaka Ohira for useful discussion about particles acceleration and informative advice.

I also thank Dr. Ryo Yamazaki and Dr. Tsuyoshi Inoue for helpful discussion about supernova remnants.

I also thank Dr. Makoto Sawada for helpful discussion about observations of supernova remnants and plasma physics.

I also thank Yasutaka Hanada for teaching me about numerical calculation technique and programing.

I also thank Tsukasa Yumibayashi, Hiromitsu Harada, Sataru Kohara, Yu-ki Sakai, and Tomofumi Teraguchi for helpful and enjoyable discussion about physics.

I also thank my family for helpful supports. Without their support, this thesis could not be completed.

Thanks to the support program of Tokyo Metropolitan University, I attended the 5th international conference of gamma-ray astronomy at Heidelberg when I was a second year doctoral course student. I appreciate the program.

I am supported by the scholarship of Tokyo Metropolitan University for graduate students when I was a second and third year doctoral course student. Thanks to the scholarship program, I reduce working hours of a part-time job and spend more time on my research. I appreciate the program, and thank Professor Masai who recommend me for a candidate of the program.

Bibliography

[1] Abdo, A. A., Ackermann, M., Ajello, M., et al. 2009, ApJL, 706, L1
[2] Abdo, A. A., Ackermann, M., Ajello, M., et al. 2010a, ApJ, 718, 348
[3] Abdo, A. A., Ackermann, M., Ajello, M., et al. 2010b, ApJ, 722, 1303
[4] Abdo, A. A., Ackermann, M., Ajello, M., et al. 2011, ApJ, 734, 28
[5] Acciari, V. A., Aliu, E., Arlen, T., et al. 2009, ApJL, 698, L133
[6] Acciari, V. A., Aliu, E., Arlen, T., et al. 2010, ApJ, 714, 163
[7] Acciari, V. A., Aliu, E., Arlen, T., et al. 2011, ApJL, 730, L20
[8] Ackermann, M., Ajello, M., Allafort, A., et al. 2012, Physical Review Letters, 108, 011103
[9] Ackermann, M., Ajello, M., Allafort, A., et al. 2013, Science, 339, 807
[10] Adriani, O., Barbarino, G. C., Bazilevskaya, G. A., et al. 2011, Physical Review Letters, 106, 201101
[11] Aharonian, F. A., & Atoyan, A. M. 2000, A&A, 362, 937
[12] Aharonian, F., Akhperjanian, A. G., Bazer-Bachi, A. R., et al. 2006, A&A, 449, 223
[13] Aharonian, F., Akhperjanian, A. G., Bazer-Bachi, A. R., et al. 2007, ApJ, 661, 236
[14] Aharonian, F., Akhperjanian, A. G., Bazer-Bachi, A. R., et al. 2008, A&A, 481, 401
[15] Aharonian, F., Akhperjanian, A. G., Barres de Almeida, U., et al. 2008, A&A, 483, 509
[16] Ajello, M., Allafort, A., Baldini, L., et al. 2012, ApJ, 744, 80
[17] Aleksić, J., Alvarez, E. A., Antonelli, L. A., et al. 2012, A&A, 541, A13
[18] Allen, C. W. 1973, London: University of London, Athlone Press, lc1973, 3rd ed.,
[19] Araya, M. 2013, MNRAS, 434, 2202
[20] Arbutina, B., Urošević, D., Andjelić, M. M., Pavlović, M. Z., & Vukotić, B. 2012, ApJ, 746, 79
[21] Arbutina, B., Urošević, D., Vučetić, M. M., Pavlović, M. Z., & Vukotić, B. 2013, ApJ, 777, 31
[22] Baars, J. W. M., Genzel, R., Pauliny-Toth, I. I. K., & Witzel, A. 1977, A&A, 61, 99
[23] Bamba, A., Yokogawa, J., Sakano, M., & Koyama, K. 2000, PASJ, 52, 259
[24] Barbon, R., Ciatti, F., & Rosino, L. 1979, A&A, 72, 287
[25] Bell, A. R. 1978a, MNRAS, 182, 147
[26] Bell, A. R. 1978b, MNRAS, 182, 443
[27] Bell, A. R. 2004, MNRAS, 353, 550
[28] Bell, A. R., & Lucek, S. G. 2001, MNRAS, 321, 433
[29] Berezhko, E. G., Ksenofontov, L. T., Völk, H. J. 2003, A&A, 412, L11

[30] Bertola, F. 1964, Annales d'Astrophysique, 27, 319
[31] Berezinskii, V. S., Bulanov, S. V., Dogiel, V. A., & Ptuskin, V. S. 1990, in The astrophysics of cosmic rays, ed. Ginzburg, V. L. (Amsterdam:North-Holland)
[32] Blair, W. P., Sankrit, R., & Raymond, J. C. 2005, AJ, 129, 2268
[33] Blandford, R. D., & Ostriker, J. P. 1978, ApJL, 221, L29
[34] Blondin, J. M., & Lundqvist, P. 1993, ApJ, 405, 337
[35] Blondin, J. M., Wright, E. B., Borkowski, K. J., & Reynolds, S. P. 1998, ApJ, 500, 342
[36] Blumenthal, G. R., & Gould, R. J. 1970, Rev. Mod. Phys., 42, 237
[37] Boumis, P., Meaburn, J., López, J. A., et al. 2004, A&A, 424, 583
[38] Brogan, C. L., Lazio, T. J., Kassim, N. E., & Dyer, K. K. 2005, AJ, 130, 148
[39] Brun, F., de Naurois, M., Hofmann, W., et al. 2011, arXiv:1104.5003
[40] Case, G. L., & Bhattacharya, D. 1998, ApJ, 504, 761
[41] Castelletti, G., Dubner, G., Brogan, C., & Kassim, N. E. 2007, A&A, 471, 537
[42] Castelletti, G., Dubner, G., Clarke, T., & Kassim, N. E. 2011, A&A, 534, A21
[43] Castro, D., & Slane, P. 2010, ApJ, 717, 372
[44] Castro, D., Slane, P. O., Gaensler, B. M., Hughes, J. P., & Patnaude, D. J. 2011, ApJ, 734, 86
[45] Chatterjee, S., et al. 2009, ApJ, 698, 250
[46] Chevalier, R. A. 1974, ApJ, 188, 501
[47] Chevalier, R. A. 1982, ApJ, 258, 790
[48] Chevalier, R. A. & Irwin C. M., 2011, ApJ, 729, L6
[49] Claussen, M. J., Frail, D. A., Goss, W. M., & Gaume, R. A. 1997, ApJ, 489, 143
[50] Cox, D. P., Shelton, R. L., Maciejewski, W., Smith, R. K., Plewa, T., Pawl, A., & Różyczka, M. 1999, ApJ, 524, 179
[51] Dame, T. M., Hartmann, D., & Thaddeus, P. 2001, ApJ, 547, 792
[52] Dermer, C. D. 1986 A&A, 157, 223
[53] Dubner, G. M., Moffett, D. A., Goss, W. M., & Winkler, P. F. 1993, AJ, 105, 2251
[54] Dubner, G. M., Velázquez, P. F., Goss, W. M., & Holdaway, M. A. 2000, AJ, 120, 1933
[55] Duncan, A. R., & Green, D. A. 2000, A&A, 364, 732
[56] Duncan, A. R., Stewart, R. T., Campbell-Wilson, D., et al. 1997, MNRAS, 289, 97
[57] Ekers, R. D., van Gorkom, J. H., Schwarz, U. J., & Goss, W. M. 1983, A&A, 122, 143
[58] Enoguchi, H., Tsunemi, H., Miyata, E., & Yoshida, K. 2002, PASJ, 54, 229
[59] Fermi, E. 1949, Physical Review, 75, 1169
[60] Ferrand, G., Decourchelle, A., Ballet, J., Teyssier, R., & Fraschetti, F. 2010, A&A, 509, L10
[61] Fich, M., Blitz, L., & Stark, A. A. 1989, ApJ, 342, 272
[62] Filippenko, A. V. 1988, AJ, 96, 1941
[63] Filippenko, A. V. 1997, ARA&A, 35, 309
[64] Frail, D. A., Goss, W. M., & Slysh, V. I. 1994, ApJL, 424, L111
[65] Frail, D. A., Goss, W. M., Reynoso, E. M., Giacani, E. B., Green, A. J., & Otrupcek, R. 1996, AJ, 111, 1651
[66] Fraschetti, F. 2013, ApJ, 770, 84

[67] Fukui, Y., Moriguchi, Y., Tamura, K., et al. 2003, PASJ, 55, L61
[68] Fukui, Y., Sano, H., Sato, J., et al. 2012, ApJ, 746, 82
[69] Gal-Yam, A., 2012, Science, 337, 927
[70] Gal-Yam, A., & Leonard, D. C. 2009, Nature, 458, 865
[71] Gao, X. Y., Han, J. L., Reich, W., et al. 2011, A&A, 529, A159
[72] Giacani, E. B., Dubner, G., Cappa, C., & Testori, J. 1998, A&AS, 133, 61
[73] Giacani, E., Smith, M. J. S., Dubner, G., et al. 2009, A&A, 507, 841
[74] Giacani, E., Smith, M. J. S., Dubner, G., & Loiseau, N. 2011, A&A, 531, A138
[75] Ginzburg, V. L., & Syrovatskii, S. I. 1965, ARA&A, 3, 297
[76] Giordano, F., et al. 2012, ApJL, 744, L2
[77] Giuliani, A., et al. 2011, ApJL, 742, L30
[78] Gotthelf, E. V., & Vasisht, V. 1997, ApJ, 486, L133
[79] Gould, R. J. 1969, Physical Review, 185, 72
[80] Green, A. J., Baker, J. R., & Landecker, T. L. 1975, A&A, 44, 187
[81] Green, A. J., Frail, D. A., Goss, W. M., & Otrupcek, R. 1997, AJ, 114, 2058
[82] Green, D. A. 2009, Bulletin of the Astronomical Society of India, 37, 45
[83] Hailey, C. J., & Craig, W. W. 1994, ApJ, 434, 635
[84] Hanabata, Y., Sawada, M., Katagiri, H., Bamba, A., & Fukazawa, Y. 2013, PASJ, 65, 42
[85] Harrus, I. M., Slane, P. O., Smith, R. K., & Hughes, J. P. 2001, ApJ, 552, 614
[86] Hayato, A., Yamaguchi, H., Tamagawa, T., et al. 2010, ApJ, 725, 894
[87] Hewitt, J. W., Grondin, M.-H., Lemoine-Goumard, M., Reposeur, T., Ballet, J., & Tanaka, T. 2012, ApJ, 759, 89
[88] Hewitt, J. W., & Yusef-Zadeh, F. 2009, ApJL, 694, L16
[89] Hillebrandt, W., & Niemeyer, J. C. 2000, ARA&A, 38, 191
[90] Hnatyk, B., & Petruk, O. 1999, A&A, 344, 295
[91] Hui, C. Y., Wu, E. M. H., Wu, J. H. K., et al. 2011, ApJ, 735, 115
[92] Hwang, U., & Gotthelf, E. V. 1997, ApJ, 475, 665
[93] Hwang, U., Petre, R., & Hughes, J. P. 2000, ApJ, 532, 970
[94] Inoue, T., Yamazaki, R., Inutsuka, S.-i., & Fukui, Y. 2012, ApJ, 744, 71
[95] Itoh, H., & Masai, K. 1989, MNRAS, 236, 885
[96] Jiang, B., Chen, Y., Wang, J., et al. 2010, ApJ, 712, 1147
[97] Karzas, W. J., & Latter, R. 1961, ApJS, 6, 167
[98] Kassim, N. E., & Weiler, K. W. 1990, ApJ, 360, 184
[99] Katagiri, H., Tibaldo, L., Ballet, J., et al. 2011, ApJ, 741, 44
[100] Katsuda, S., Maeda, K., Nozawa, T., Pooley, D., & Immler, S. 2014, ApJ, 780, 184
[101] Katsuda, S., Petre, R., Hwang, U., Yamaguchi, H., Mori, K., & Tsunemi, H. 2009, PASJ, 61, S155
[102] Katsuda, S., Tsunemi, H., & Mori, K. 2008, ApJL, 678, L35
[103] Katsuta, J., Uchiyama, Y., Tanaka, T., et al. 2012, ApJ, 752, 135
[104] Kawasaki, M. T., Ozaki, M., Nagase, F., et al. 2002, ApJ, 572, 897
[105] Kawasaki, M., Ozaki, M., Nagase, F., Inoue, H., & Petre, R. 2005, ApJ, 631, 935
[106] Keohane, J. W., Reach, W. T., Rho, J., & Jarrett, T. H. 2007, ApJ, 654, 938

[107] Kiewe, M., Gal-Yam, A., Arcavi, I., et al. 2012, ApJ, 744, 10
[108] Kinugasa, K., & Tunemi, H. 1999, PASJ, 51, 239
[109] Koo, B.-C., Kim, K.-T., & Seward, F. D. 1995, ApJ, 447, 211
[110] Koralesky, B., Frail, D. A., Goss, W. M., Claussen, M. J., & Green, A. J. 1998, AJ, 116, 1323
[111] Kothes, R., Fedotov, K., Foster, T. J., & Uyanıker, B. 2006, A&A, 457, 1081
[112] Koyama, K., Petre, R., Gotthelf, E. V., et al. 1995, Nature, 378, 255
[113] Krymsky, G. F., Kuzmin, A. I., Petukhov, S. I., & Turpanov, A. A. 1979, International Cosmic Ray Conference, 2, 39
[114] Landecker, T. L., Pineault, S., Routledge, D., & Vaneldik, J. F. 1989, MNRAS, 237, 277
[115] Landecker, T. L., Roger, R. S., & Higgs, L. A. 1980, A&AS, 39, 133
[116] Lazendic, J. S., Slane, P. O., Hughes, J. P., Chen, Y., & Dame, T. M. 2005, ApJ, 618, 733
[117] Leahy, D. A., & Tian, W. W. 2007, A&A, 461, 1013
[118] Maeder, A., & Meynet, G. 2000, ARA&A, 38, 143
[119] Mauerhan, J. C., Smith, N., Filippenko, A. V., et al. 2013, MNRAS, 430, 1801
[120] Masai, K. 1984, Ap&SS, 98, 367
[121] Masai, K. 1994, ApJ, 437, 770
[122] McClure-Griffiths, N. M., Green, A. J., Dickey, J. M., et al. 2001, ApJ, 551, 394
[123] McKee, C. F. 1974, ApJ, 188, 335
[124] McKee, C. F., & Ostriker, J. P. 1977, ApJ, 218, 148
[125] Milne, D. K., Caswell, J. L., Kesteven, M. J., Haynes, R. F., & Roger, R. S. 1989, Proceedings of the Astronomical Society of Australia, 8, 187
[126] Minkowski, R. 1941, PASP, 53, 224
[127] Miyata, E., Katsuda, S., Tsunemi, H., Hughes, J. P., Kokubun, M., & Porter,F. S. 2007 PASJ, 59, S163
[128] Moffett, D. A., & Reynolds, S. P. 1994, ApJ, 437, 705
[129] Moon, D.-S., & Koo, B.-C. 1994, Journal of Korean Astronomical Society, 27, 81
[130] Moriya, T. J., & Tominaga, N., 2012, ApJ, 747, 118
[131] Nakamura, R., Bamba, A., Ishida, M., Nakajima, H., Yamazaki, R., Terada, Y., Pühlhofer, G., & Wagner, S. J. 2009, PASJ, 61, S197
[132] Nakamura, R., Bamba, A., Dotani, T., Ishida, M., Yamazaki, R., & Kohri, K. 2012, ApJ, 746, 134
[133] Ness, N. F., Scearce, C. S., & Seek, J. B. 1964, J. Geophys. Res, 69, 3531
[134] Ohnishi, T., Koyama, K., Tsuru, T. G., Masai, K., Yamaguchi, H., & Ozawa, M. 2011, PASJ, 63, 527
[135] Ostrowski, M. 1999, A&A, 345, 256
[136] Ozawa, M., Koyama, K., Yamaguchi, H., Masai, K., & Tamagawa, T. 2009, ApJL, 706, L71
[137] Panagia, N., Van Dyk, S. D., Weiler, K. W., et al. 2006, ApJ, 646, 369
[138] Parizot, E., Marcowith, A., Ballet, J., & Gallant, Y. A. 2006, A&A, 453, 387
[139] Park, S., Kargaltsev, O., Pavlov, G. G., Mori, K. Slane, P. O., Hughes, J. P., Bur-

rows, D. N., & Garmire, G. P. 2009, ApJ, 695, 431
[140] Park, S., Slane, P. O., Hughes, J. P., Mori, K., Burrows, D. N., & Garmire, G. P. 2007, ApJ, 665, 1173
[141] Petruk, O. 2001, A&A, 371, 267
[142] Pfeffermann, E., Aschenbach, B., & Predehl, P. 1991, A&A, 246, L28
[143] Pivato, G., Hewitt, J. W., Tibaldo, L., et al. 2013, ApJ, 779, 179
[144] Putze, A., Maurin, D., & Donato, F. 2011, A&A, 526, A101
[145] Pye, J. P., Thomas, N., Becker, R. H., & Seward, F. D., 1984, MNRAS, 207, 649
[146] Reed, J. E., Hester, J. J., Fabian, A. C., & Winkler, P. F. 1995, ApJ, 440, 706
[147] Reich, W., & Fuerst, E. 1984, A&AS, 57, 165
[148] Reid, M. J. 1993, ARA&A, 31, 345
[149] Reynolds, S. P., Gaensler, B. M., & Bocchino, F. 2012, SSR, 166, 231
[150] Reynolds, S. P., Borkowski, K. J., Hwang, U., Harrus, I., Petre, R., & Dubner, G. 2006, ApJL, 652, L45
[151] Reynoso, E. M., Dubner, G. M., Goss, W. M., & Arnal, E. M. 1995, AJ, 110, 318
[152] Reynoso, E. M., Johnston, S., Green, A. J., & Koribalski, B. S. 2006, MNRAS, 369, 416
[153] Rho, J., & Petre, R. 1998, ApJL, 503, L167
[154] Rho, J., Dyer, K., Borkowski, K. J., & Reynolds, S. P. 2002, ApJ, 581, 1116
[155] Rosado, M., & Gonzalez, J. 1981, RMxAA, 5, 93
[156] Routledge, D., Dewdney, P. E., Landecker, T. L., & Vaneldik, J. F. 1991, A&A, 247, 529
[157] Russell, B. R., & Immler, S. 2012, ApJL, 748, L29
[158] Rybicki, G. B., & Lightman, A. P. 1979, New York, Wiley-Interscience, 1979. 393
[159] Safi-Harb, S., Dubner, G., Petre, R., Holt, S. S., & Durouchoux, P. 2005, ApJ, 618, 321
[160] Sakano, M., Warwick, R. S., Decourchelle, A., & Predehl, P. 2004, MNRAS, 350, 129
[161] Saken, J. M., Long, K. S., Blair, W. P., & Winkler, P. F. 1995, ApJ, 443, 231
[162] Sasaki, M., Plucinsky, P. P., Gaetz, T. J., Smith, R. K., Edger, R. J., & Slane, P. O. 2004, ApJ, 617, 322
[163] Sawada, M., & Koyama, K. 2012, PASJ, 64, 81
[164] Sawada, M., Tsuru, T. G., Koyama, K., & Oka, T. 2011, PASJ, 63, 849
[165] Schlegel, E. M. 1990, MNRAS, 244, 269
[166] Schlegel, E. M. 1995, Rep. Prog. Phy. 58. 1375
[167] Sedov, L. I. 1959, Similarity and Dimensional Methods in Mechanics, New York: Academic Press, 1959
[168] Sezer, A., Gök, F., Hudaverdi, M., & Ercan, E. N. 2011, MNRAS, 417, 1387
[169] Shaver, P. A., Salter, C. J., Patnaik, A. R., van Gorkom, J. H., & Hunt, G. C. 1985, Nature, 313, 113
[170] Smith, A., Peacock, A., Jones, L. R., & Pye, J. P. 1985, ApJ, 296,469
[171] Sonett, C. P., & Abrams, I. J. 1963, J. Geophys. Res., 68, 1233
[172] Spitzer, L. 1962, Physics of Fully Ionized Gases, New York: Interscience (2nd edition), 1962

[173] Stage, M. D., Allen, G. E., Houck, J. C., & Davis, J. E. 2006, Nature Physics, 2, 614
[174] Stone, J. M., Gardiner, T. A., Teuben, P., Hawley, J. F., & Simon, J. 2008, ApJS, 178, 137
[175] Sun, X. H., Reich, P., Reich, W., et al. 2011, A&A, 536, A83
[176] Sun, M., Seward, F. D., Smith, R. K., & Slane, P. O. 2004, ApJ, 605, 742
[177] Tamura, K. 1995, Ph.D. thesis, Osaka Univ.
[178] Tanaka, T., Allafort, A., Ballet, J., et al. 2011, ApJL, 740, L51
[179] Tatematsu, K., Fukui, Y., Landecker, T. L., & Roger, R. S. 1990, A&A, 237, 189
[180] Taylor, G. 1950, Royal Society of London Proceedings Series A, 201, 159
[181] Torres, D. F., Rodriguez Marrero, A. Y., & de Cea Del Pozo, E. 2008, MNRAS, 387, L59
[182] Troja, E., Bocchino, F., Miceli, M., & Reale, F. 2008, A&A, 485, 777
[183] Truelove, J. K., & McKee, C. F. 1999, ApJS, 120, 299
[184] Uchida, H., Koyama, K., Yamaguchi, H., et al. 2012, PASJ, 64, 141
[185] Uchida, K., Morris, M., & Yusef-Zadeh, F. 1992, AJ, 104, 1533
[186] Uchiyama, Y., Aharonian, F. A., Tanaka, T., Takahashi, T., & Maeda, Y. 2007, Nature, 449, 576
[187] Uchiyama, Y., Takahashi, T., Aharonian, F. A., & Mattox, J. R. 2002, ApJ, 571, 866
[188] Uyaniker, B., Kothes, R., & Brunt, C. M. 2002, ApJ, 565, 1022
[189] Uyanıker, B., Reich, W., Yar, A., & Fürst, E. 2004, A&A, 426, 909
[190] Velázquez, P. F., Dubner, G. M., Goss, W. M., & Green, A. J. 2002, AJ, 124, 2145
[191] Vink, J. 2012, ARA&A, 20, 49
[192] Weiler, K. W., Panagia, N., Montes, M. J., & Sramek, R. A. 2002, ARA&A, 40, 387
[193] Welsh, B. Y., & Sallmen, S. 2003, A&A, 408, 545
[194] White, R. L., & Long, K. S. 1991, ApJ, 373, 543
[195] Wolszczan, A., Cordes, J. M., & Dewey, R. J. 1991, ApJ, 372, L99
[196] Woosley, S. E., Heger, A., & Weaver, T. A. 2002, Reviews of Modern Physics, 74, 1015
[197] Woosley, S. E., Langer, N., & Weaver, T. A. 1995, ApJ, 448, 315
[198] Xiao, L., Fürst, E., Reich, W., & Han, J. L. 2008, A&A, 482, 783
[199] Xiao, L., Reich, W., Fürst, E., & Han, J. L. 2009, A&A, 503, 827
[200] Xu, J. W., Han, J. L., Sun, X. H., et al. 2007, A&A, 470, 969
[201] Yamaguchi, H., Koyama, K., Katsuda, S., Nakajima, H., Hughes, J. P., Bamba, A., Hiraga, J. S., Mori, K., Ozaki, M., & Tsuru, T. G. 2008, PASJ, 60, S141
[202] Yamaguchi, H., Ozawa, M., Koyama, K., Masai, K., Hiraga, J. S., Ozaki, M., & Yonetoku, D. 2009, ApJL, 705, L6
[203] Yamaguchi, H., Tanaka, M., Maeda, K., et al. 2012, ApJ, 749, 137
[204] Yamauchi, S., Nobukawa, M., Koyama, K., & Yonemori, M. 2013a, PASJ, 65, 6
[205] Yamauchi, S., Minami, S., Ota, N., & Koyama, K. 2013b, arXiv:1308.1755
[206] Yuan, Y., Funk, S., Jóhannesson, G., et al. 2013, ApJ, 779, 117
[207] Yusef-Zadeh, F., Uchida, K. I., & Roberts, D. 1995, Science, 270, 1801
[208] Zel'dovich, Y. B., & Raizer, Y. P. 1966, Physics of Shock Waves and High-Temperature Hydrodynamic Phenomena, ed. W. D. Hayes & R. F. Probstein, Volume I (Academic Press New York and London), 103

[209] Zirakashvili, V. N., & Aharonian, F. A. 2010, ApJ, 708, 965